The Dissertation Committee for Sangpil Yoon
Certifies that this is the approved version of the following dissertation:

Estimation of the Mechanical Properties of Soft Tissues using a Laser-Induced Microbubble Interrogated by Acoustic Radiation Force

Committee:

Stanislav Y. Emelianov, Supervisor

Mark F. Hamilton

Salavat R. Aglyamov

Preston S. Wilson

Andrei B. Karpiouk

Kirill Larin

Estimation of the Mechanical Properties of Soft Tissues using a Laser-Induced Microbubble Interrogated by Acoustic Radiation Force

by

Sangpil Yoon, B.S.; M.S.

Dissertation

Presented to the Faculty of the Graduate School of

The University of Texas at Austin

in Partial Fulfillment

of the Requirements

for the Degree of

Doctor of Philosophy

The University of Texas at Austin

May 2012

Dedication

Dedicated to my family, Junghea Park, Jiho Yoon, and Olivia Yoon

Acknowledgements

I have always wished I had a space to thank everyone who supports me on both professional and private levels. It would be unfair to acknowledge anyone else before my supervisor, Dr. Stanislav Emelianov. He has provided the fundamental bases for my research, room to think and create ideas, and opportunities to show my work to academia. Working with Stas has been a privilege and I believe that it is a great honor to have worked with him for about three and a half years. In addition to Stas, Dr. Salavat Aglyamov has been my constant companion during my stay at the lab. We discussed many intellectual curiosities and Salavat was a mentor for me throughout. Dr. Mark Hamilton gave me tremendous intuition in theoretical cognition in Acoustics and even in Optics. I also would like to thank my committee members for their time and consideration during the process of my defense. I have also had the pleasure to work with the members of the Ultrasound Imaging and Therapeutics Laboratory. They were precious sources of ingenious ideas for my research and playmates in sports activities. Tera Sherrard is more than just a staff member of my lab. She helped me to survive in the tricky administrative processes. My friend, Kevin Bourque (AKA interrobang), gave me inspiration in English writing.

On the private level, my wife, Junghea Park, has always been the first supporter of my work and life. I would like to thank my wife for her love, patience, and food. If it would be possible, I would like to award her a “Ph.D. degree in unfailing perseverance.” When I decided to quit my job and go to academia, without her understanding and support, I might not even have started my journey getting a Ph.D. degree. She and my children, Jiho and Olivia, always make me smile during my hard work and have provided

a thrust to complete my work. My achievements are the consequences of my grandmother and parents' sacrifice and the power of my family. They always expected unrivalled accomplishment and enlightened me to the value thereof. They deserve to get full credit for my accomplishment and I hope they remember the influence of their contribution.

Estimation of the Mechanical Properties of Soft Tissues using a Laser-Induced Microbubble Interrogated by Acoustic Radiation Force

Sangpil Yoon, Ph.D.

The University of Texas at Austin, 2012

Supervisor: Stanislav Y. Emelianov

This dissertation introduces a new approach to measure the mechanical properties of soft tissues. A laser-induced microbubble, created by focusing a single nanosecond laser pulse with a custom-made objective lens, was created at desired locations inside a tissue sample. An acoustic radiation force was generated by a low frequency transducer to displace the microbubble. A custom-built high pulse repetition frequency (PRF) ultrasound system, consisting of two 25 MHz single element transducers, was used to track the dynamics of the microbubble. Reconstruction of the mechanical properties at the specific location in a tissue sample was performed using a theoretical model, which calculated the dynamics of a microbubble under an externally applied force in a viscoelastic medium. The theoretical model and the high PRF ultrasound system were successfully validated in both gelatin phantoms and *ex vivo* bovine crystalline lenses.

Age-related sclerosis of the crystalline lenses from bovine was clearly detected, which might be linked to changes in the crystalline. Location-dependent variation explained that the outer cortex and the inner nucleus had different mechanical properties. In the old and young porcine vitreous humors, age-related changes were not found. However, local variations of the mechanical properties were discovered, which may

coincide with the different distributions of the molecular compositions. The laser-induced microbubble approach shows potential for future research into the origin of physiological phenomena and the development of inherent disorders in the eye. I hope that further studies – in the development of a more suitable theoretical model for the microbubble dynamics, in extension to *in vivo* applications, and in defining the relationship of the mechanical properties to molecular components in the eye – may provide a plan for the therapeutic treatment of eye-related diseases.

Table of Contents

List of Tables

List of Figures

Chapter 1: *Introduction*

1.1 BACKGROUND

Tissues are layers of similar cells that perform a specific function. Organs may consist of different kinds of tissues. The ability of tissues to interact with one another in an organ is vitally important to perform specific functions for higher level organs. All organs begin to lose some function as people age. Aging changes have been found in all body cells, tissues, and organs and these changes affect the physiological function throughout the body. One example of the importance of interaction between tissues and the age-related degradation of organs is the human eye, which needs the delicate interplay between a crystalline lens and its constituent parts such as the zonule fiber, ciliary muscles, and vitreous humor to focus light. Age-related degradation of the crystalline lens and the vitreous humor is manifested in the form of visual disturbances and even the loss of vision.

Reliable measurements of the mechanical properties of ocular tissues may provide better understanding of the physiological activities and phenomena associated with their degradation. Accommodation is the process by which the eye changes its optical power to maintain a clear image of an object as its distance varies by changing the shape of the crystalline lens. The loss of this accommodation power is referred to as presbyopia. The fundamental concepts behind the mechanism of accommodation and the onset of presbyopia are not yet established because only limited information related to mechanical properties of the crystalline lens is available. The vitreous develops pockets of liquefied regions due to vitreous liquefaction. The problem of vitreous liquefaction is that it may lead to retinal detachment, which is directly related to blindness. One possible explanation of the vitreous liquefaction is the aggregation of collagen fibrils. Understanding the reasons for vitreous liquefaction and the development of treatment

plans for retinal detachment have been hampered by a lack of reliable measurements of the mechanical properties of the vitreous, which has made it difficult to understand the relationship of the chemical composition and microstructure to the mechanical properties.

Therapeutic planning for age-related diseases related to ocular tissues can be developed with precise measurements of the mechanical properties of ocular structures. To date only surgical solutions to presbyopia have been offered such as lens implants and mono-vision surgeries. Currently, reading glasses and contact lenses are the common treatments. Because one of the main reasons for presbyopia is crystalline lens sclerosis, regaining the compliance of the lens would be one possible treatment of presbyopia [1-3]. It is of importance to have an elasticity map of the crystalline lens for each individual; the amount of elasticity in different parts of the crystalline lens should be defined for the best outcome of the treatment. During the surgical procedure for retinal detachment, called vitrectomy, empty spaces inside the eye cavity are filled with vitreous substitutes. Making vitreous substitutes that resemble the mechanical properties of the vitreous humor in its natural state is important because proper intraocular pressure inside the eye should be maintained for physiological activities such as accommodation.

The goal of this dissertation is to develop an approach to measure the mechanical properties of *ex vivo* animal ocular tissues such as the crystalline lens and the vitreous humor (Figure 1.1) to investigate age-related changes and location-dependent variations of the mechanical properties. This goal consists of five specific objectives:

1. Adopt a theoretical model of microbubble dynamics in a viscoelastic medium under acoustic radiation force (as in Chapter 2).
2. Validate the theoretical model in a tissue-mimicking phantom (Chapter 3).

3. Develop a high pulse repetition frequency (PRF) ultrasound system to accurately measure microbubble dynamics (Chapter 4).
4. Validate the theoretical model and the high PRF ultrasound system in *ex vivo* bovine crystalline lenses (Chapter 4).
5. Compare the changes and variations of ocular tissue mechanical properties with respect to different ages over samples and different locations within a sample (Chapters 5 and 6).

The approach to achieve these objectives is to use a laser-induced microbubble, created by optical breakdown of a nanosecond laser pulse, to measure the localized mechanical properties of either soft tissues or a tissue-mimicking phantom and to use acoustic radiation force to palpate the microbubble. Once the dynamics of the microbubble under acoustic radiation force was measured with an ultrasound probing system, reconstruction of the mechanical properties of a surrounding medium was performed using a theoretical model of the microbubble dynamics.

The first hypothesis of this dissertation is that the dynamics of a laser-induced microbubble with externally applied forces depends on the mechanical properties of the surrounding medium, which allows us to acquire information about the viscoelastic properties of the local area surrounding the microbubble. The second hypothesis is that local variations and age-related changes in the mechanical properties of the crystalline lens and the vitreous humor are related to the internal microstructures and the distribution of biochemical materials of ocular tissues. The latter will be confirmed by comparing the results of this dissertation and previously reported results from the literature.

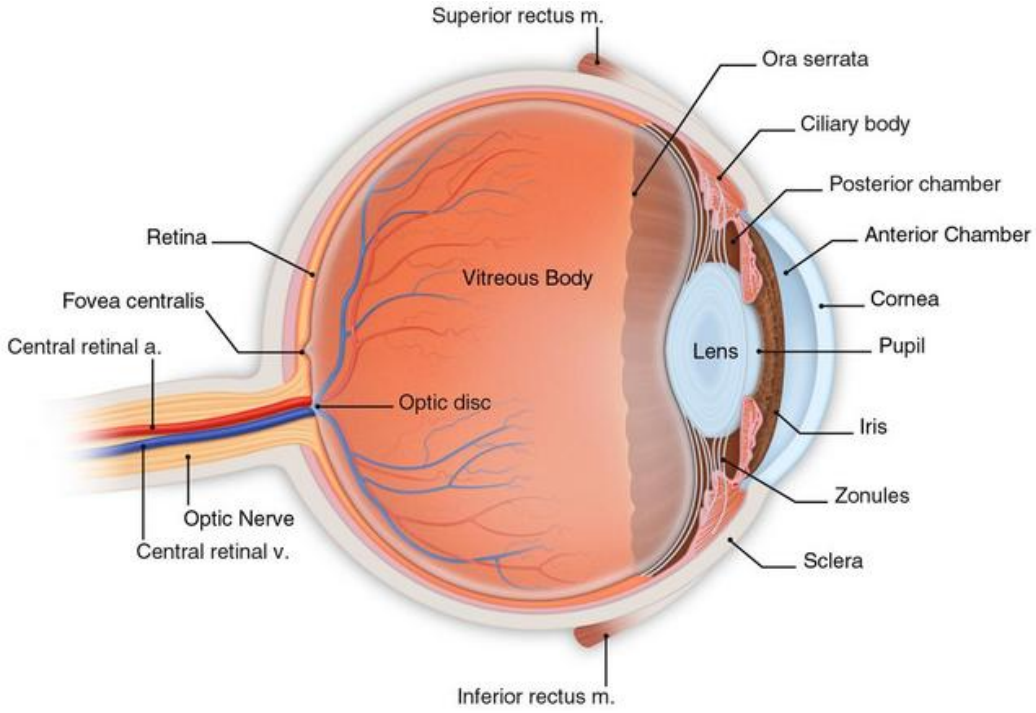

Figure 1.1: The human eye anatomy. Interactions between lens, ciliary body, and the zonule fiber are important to focus light. The vitreous maintains the shape of the whole eye globe and provides the pathway to light to make an image on the retina. Image is at "http://www.wnyretina.com/eye.html."

1.2 THE CRYSTALLINE LENS

The lens and the cornea are the main refracting surfaces of the eye. The lens is a transparent, avascular, biconvex structure held in position behind the pupil by zonular fibers (Fig. 1.1) [4]. The lens substance is surrounded by the lens capsule (Fig. 1.2). The crystalline lens is unique in that it grows throughout its whole life by adding new cells to the existing ones [5]. Due to this growth, the majority of lens fibers has lost their nuclei, and has migrated inward to form an increasingly compact tissue [6]. A central nucleus consists of the oldest lens fibers (the embryonic nucleus in Fig. 1.3) and is surrounded by more recently formed fibers to form a nucleus (Fig. 1.3). Younger fibers constitute the lens cortex. The lens has no blood vessels, so its metabolism is anaerobic. Fig. 1.3 reveals

the heterogeneous structure of the crystalline lens, evident by the presence of several different layers, created in different developmental stages [7]. Each region in Fig. 1.3 has different light scattering properties and different refractive index.

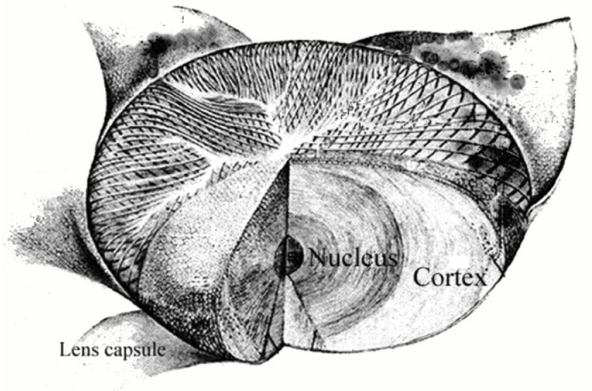

Figure 1.2: The anatomy of the crystalline lens (http://www.oculist.net/downaton502/prof/ebook/duanes/pages/v7/ch015/012f.html).

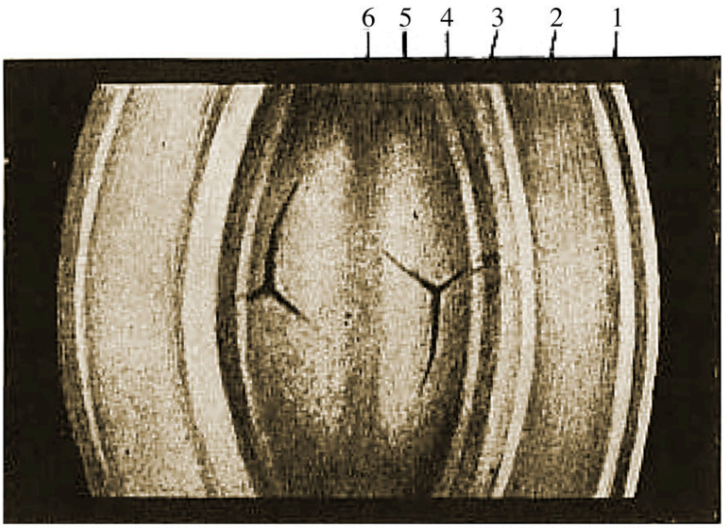

FIG. 378.–The lens of an adult of 40 years.

1. Anterior capsule.
2. Cortex.
3. Adult nucleus.
4. Infantile nucleus.
5. Foetal nucleus.
6. Embryonic nucleus.

Figure 1.3: Nomenclature of the optical zones in the human crystalline lens. (Reproduced by Fig. 378 from Systems of Ophthalmology [Duke-Elder and Wybar, 1961])

The crystalline lens can change its shape by virtue of its inherent elasticity. This provides increased refractive power (accommodation). However, the lens gradually loses its elastic properties, and usually by 40-50 years of age the ability to change its shape in response to the ciliary muscle significantly decreases, providing inappropriate refractive power for a near object (presbyopia).

1.2.1 Models of accommodative mechanism

The mechanism through which the lens changes its shape to focus near and distant objects is not yet understood. This knowledge gap may be due to the lack of information regarding elastic properties of the crystalline lens and/or the force balance between the lens and its constituent parts, such as zonular fibers and the ciliary muscle. The first theory states that relaxation of the ciliary muscle induces tension in the zonular fiber by stretching it [8-10]. In turn, the lens is in a flat shape, which is ideal for long distance vision. When accommodated, the contracted ciliary muscle moves inward to release the zonular fiber without tension. Because there is no tension, the lens becomes a rounded shape to focus the near object. This theory has long been accepted but there has been debate about the accommodative mechanism (Table 1.1). Tscherning [11] disagreed with the Helmholtz theory [10] that the tension of the zonular fiber stretches the periphery of the lens. Instead Tscherning proposed that because the central part has higher elastic resistance, bulging at this part could contribute to the focus of a near object. The location-dependent variations of the elastic properties of a lens were also suggested.

Because the mechanism of accommodation has not yet been established, the reasons for the development of presbyopia have not been adequately described.

Theory	C.M.	Z.F.	D	h	MPG
I	Contract	No tension	Decrease	Increase	No
II	Contract	Tension	Increase	Decrease	Yes

Table 1.1: The theory of accommodative mechanism. C.M.: ciliary muscle. Z.F.: zonular fiber. D: the diameter of the lens. h: the thickness of the lens. MPG: the gradient of the mechanical properties in a lens. I: Helmholtz's theory of accommodation[10]. II: Tscherning's theory [11].

1.2.2 The development of presbyopia

Presbyopia is the age-related loss of accommodative power. Confusion about the development of presbyopia still exists. The accommodative power becomes almost zero by approximately 50 years of age. Notably, however, presbyopia is not affected by life style or nutrition factors. Various research groups have been involved to investigate the cause of presbyopia [12-17]. The lenticular theory relates the cause of presbyopia to stiffness changes in the crystalline lens substance. The increase of the stiffness of a lens hampers change in the lens shape although the ciliary muscle has sufficient power. Therapeutic planning is possible by changing the stiffness of a lens. Femtosecond lentotomy is a possible solution by making laser-induced incisions around the periphery of the lens [2, 3, 18]. The second theory involves the changes in ciliary muscle. Duane [19, 20] explained that the weakening of the ciliary muscle causes a reduction in power, rendering it unable to change the shape. Lastly, the growth of the lens could change the power of accommodation [21]. Forces acting on the lens by the zonular fiber become tangential by the growth of the lens.

1.2.3 Compaction and stiffness increase in a crystalline lens

As people age, compaction of a lens is the only option because of both the limited space inside the lens capsule and the need for a high refractive index. The evidence of compaction of a lens is the decrease in the fiber thickness in regions of cortex and

nucleus. Fiber thicknesses at the inner nucleus and outer cortex are about 0.8 μm and 2.0 μm, respectively [22, 23]. Investigation into the fiber thickness of lenses from 25-to-60-year-old patients revealed that older lenses had 20-30% thinner fibers [24]. Refractive index measurements, protein distributions, and speed of sound measurements of different locations in a lens and different ages proved that central compaction occurs [25, 26]. There exists a plateau at the central region of a lens which widens with age.

Lens sclerosis has long been thought a plausible reason for the development of presbyopia. Therefore, a good deal of research about the hardness/stiffness (these two terms will not be distinguished in this section) measurements of a lens have been done (Table 1.2). Intact lens measurements used the whole lens with or without the lens capsule. Thus, there is little chance for changes in elastic properties during experiments. Fragmenting a lens is subject to change the elastic properties due to the disruption of the internal crystalline. Detailed local variations in the stiffness were found by dynamic mechanical analysis but the lens fragmentation induced the elastic property changes during the experiments. Erpelding and Tabandeh used intact lenses with an ultrasound measurement technique by combining benefits of other studies: no fragmentation and local measurements of elastic properties [27, 28]. However, they had difficulties in finding elastic properties quantitatively. The amplitude of the acoustic radiation force at the focus could not be measured in Erpelding's approach, which hampered quantitative measurements. In Tabandeh's method, no relationship between hardness and ultrasound attenuation was observed and therefore it was not possible to extract the absolute value of the elastic properties of a lens.

However, in a comparison of the refractive index and the stiffness of crystalline lenses, compaction is not related to stiffness increase. The stiffness increase may be

involved in other changes in the lens such as cellular interactions or crystalline modifications [29, 30].

		Approach	Drawback
Intact lens measurements			
Author	Fisher [31, 32]	Radial force	Averaged value of stiffness and / or the effects of lens capsule
	Pau [33]	Cone penetration	
	van Alpen [34]	Uniaxial test	
	Heyworth [35] / Assia [36]	Guillotine test	
	Sharma [37]	Compression test	
	Burd [38]	Radial force	
Intact + ultrasound			
Author	Tabandeh [28]	U/S attenuation	Qualitative measurements
	Erpelding [27]	LIMB+ARF	
Fragmented lens experiments			
Author	Reilly [39]	MI	Change of the elastic properties due to fragmentation
	Heys [40]	DMA	
	Weeber [41]	DMA	

Table 1.2: Measurements techniques of hardness/stiffness of a lens. DMA: dynamic mechanical analysis. LIMB: laser-induced microbubble. ARF: acoustic radiation force. MI: microindentation. U/S: ultrasound

1.3 THE VITREOUS HUMOR

The vitreous humor is a transparent gel network composed of uniformly thin collagen fibrils suspended in a highly dilute solution of salt, protein, and hyaluronic acid (Fig. 1.4) [42]. Between the collagen fibrils, hyaluronan fills the gap with a swelling pressure to inflate the vitreous (Fig. 1.4). Its main component is water (99%). The combination of collagen fibrils and hayluronic acid is responsible for the mechanical integrities of the vitreous; thus, the mechanical properties change with the distribution of the concentrations of those components. If the vitreous is in a gel-like state, collagen type

II fibrils are connected with one another comprising a network (upper circle in Fig. 1.4). If the vitreous is liquefied (lower circle in Fig. 1.4), the collagen fibrils aggregate with each other. The volume of gel in the vitreous reduces with age. The vitreous provides metabolic requirements for the human eye [43] and controls the eye growth [44]. It also protects the eye during mechanical damages [45].

The vitreous looks like a sphere with a segment removed anteriorly to provide a depression for the lens. The vitreous humor adheres firmly to the peripheral retina, to the ciliary epithelium in the region of the pars plana (vitreous base), and to the margin of the optic disk. Sometimes it is firmly attached to retinal blood vessels. The peripheral anterior hyaloids may be loosely attached to the posterior capsule of the lens.

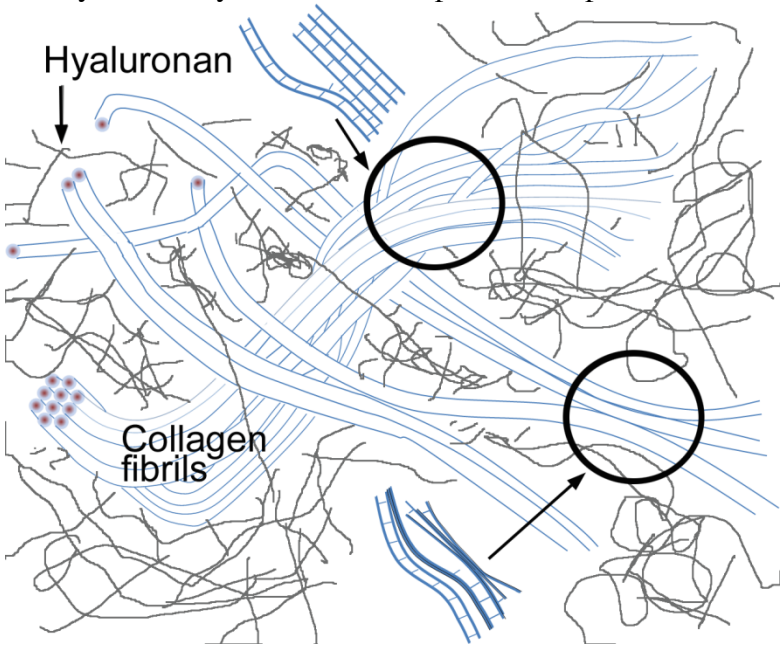

Figure 1.4: The vitreous network structure. Hyaluronan fills the gap between the collagen fibril type II network. The combination of collagen fibril and hyaluronan provides the mechanical integrity of the vitreous humor. Collagen fibrils type II are connected with each other by collagen type IV with a spacing to form an internal network (upper circle). Collagen fibrils aggregate with each other, which induces the collapse of the mechanical integrity and vitreous liquefaction (lower circle).

In a normal eye, the vitreous humor is in contact with the entire retina and is attached to the internal limiting lamina of the retina by scattered collagenous filaments. If the vitreous humor degenerates and collapses (vitreous detachment), the filamentary attachments may adhere to the sensory retina and cause a retinal hole, which may in turn lead to a retinal detachment.

Reliable measurements of the mechanical properties of the vitreous have been needed to define the relationship of the microstructure and biochemical compositions to the mechanical properties. Specifying this relationship will help us to plan therapeutic strategies for vitreous-related diseases. Thus, significant research has focused on the development of a means of measuring the mechanical properties of the vitreous humor (Table 1.3).

Authors	Approach	Parameter
Bettelheim [46]	Dynamic viscoelastometer	Dynamic storage modulus Bovine: 3-4 Pa
Zimmerman [47]	Relaxation of scattering	Elastic shear modulus Human: 0.05 Pa
Lee [48]	Micro-rheometry	Elastic shear modulus Bovine: 3 Pa Porcine: 1 Pa
Nickerson [49]	Rheometer with cleated tools	Dynamic shear storage Bovine: 7 - 32 Pa Porcine: 2.2 – 17 Pa
Zimberlin [50]	Cavitation rheology	Storage modulus Bovine: 120-660 Pa

Table 1.3: Measurements of viscoelastic properties of the vitreous humor.

1.4 OPTICAL BREAKDOWN AND LASER-INDUCED MICROBUBBLE

Laser-induced optical breakdown can be defined as the generation of an ionized gas (plasma). I will first consider laser-induced optical breakdown using nanosecond-pulses (ns-pulse). Optical breakdown induces three phenomena: plasma formation, shock wave generation, and laser-induced cavitation microbubble (LIMB) creation. The rapid temperature rise, associated with optical breakdown, is followed by a rapid pressure rise [51, 52]. The plasma region with increased pressure expands with hypersonic speed [52, 53]. At this moment, a shock wave propagates and further expansion of plasma creates LIMB [51-54]. The second rise and collapse of LIMB is due to the compressed vapor and gas inside the LIMB [55].

Damage due to plasma, shock wave, and LIMB includes evaporation at the plasma region (productively used in photodisuptive surgery in ophthalmology – posterior capsulotomy), jet flow from the collapse of LIMB near the solid boundary, interaction between existing LIMB and shock wave, and shock wave related damage. In ophthalmic applications of optical breakdown, the light damage of collateral tissues such as retina should be reduced. Long lasting LIMB should also be avoided for safety issues. The solution to reduce these damages is to use an ultra-short pulse with low energy for laser-induced optical breakdown. If an ultra-short pulse is used, the temperature and pressure at the plasma region decrease significantly because of temperature confinement and the diameter of LIMB is smaller than diffraction-limited focal size. Thus, LIMB-induced damage can be reduced. A small LIMB dissolves in a medium quickly due to the small volume and high surface tension.

In this dissertation, a ns-pulse of 5-6 ns with energy of less than 10 mJ was utilized for all experiments. The laser is not suitable for *in vivo* experiments. For future

use, however, a femtosecond laser is a good alternative to minimize damages to ocular tissues.

1.4.1 ns-pulse vs. fs-pulse

Nonlinear absorption means that the absorption coefficient of a medium depends on the intensity of the incident light. This can occur when a high power laser beam interacts with the medium [56]. The process during nonlinear absorption-induced optical breakdown – plasma formation, shock wave propagation, and LIMB creation – is the same as the process during linear absorption-induced breakdown. Pulse duration plays a key role to determine linear and nonlinear absorption-induced optical breakdowns. The main difference between ns-pulse induced and femtosecond-pulse (fs-pulse) induced optical breakdown is the ionization processes: cascade ionization by inverse bremsstrahlung (CI) and multiphoton ionization (MPI). Because MPI more highly depends on the intensity of the laser beam than CI does [57], MPI becomes important for optical breakdown for shorter laser pulse durations such as fs-pulses.

Free electron density changes during the optical breakdown, and the main process is different from duration of pulse. Free electron density evolution with a laser pulse is described by the rate equation[58-60]

$$\frac{d\rho}{dt} = \eta_{mp} + \eta_{casc} - g\rho - \eta_{rec}\rho^2 , \qquad (1.1)$$

The first two terms describe the creation of free electrons through muliphoton and cascade ionization. The last two terms indicate the losses of electron diffusion out of the focal volume and by recombination. The plots of the Equation 1.1 are shown in Fig. 1.5. Due to low intensity of ns-pulse, MPI generates few free electrons at the beginning (Fig. 1.5) and the electron density increases slowly. After CI is responsible for the breakdown,

the electron density increases dramatically in a very short time (less than 1 ns). The recombination of free electrons (loss mechanism) and CI even out (in saturation) when electron density increases. For fs-pulses, MPI dominates the breakdown procedures. Because the doubling time of electrons of CI takes a long time, even at the end of the fs-pulse, CI does not reach its saturation. The slowly increasing electron density of fs-pulse allows us to tune the breakdown threshold by changing the intensity of the laser beam.

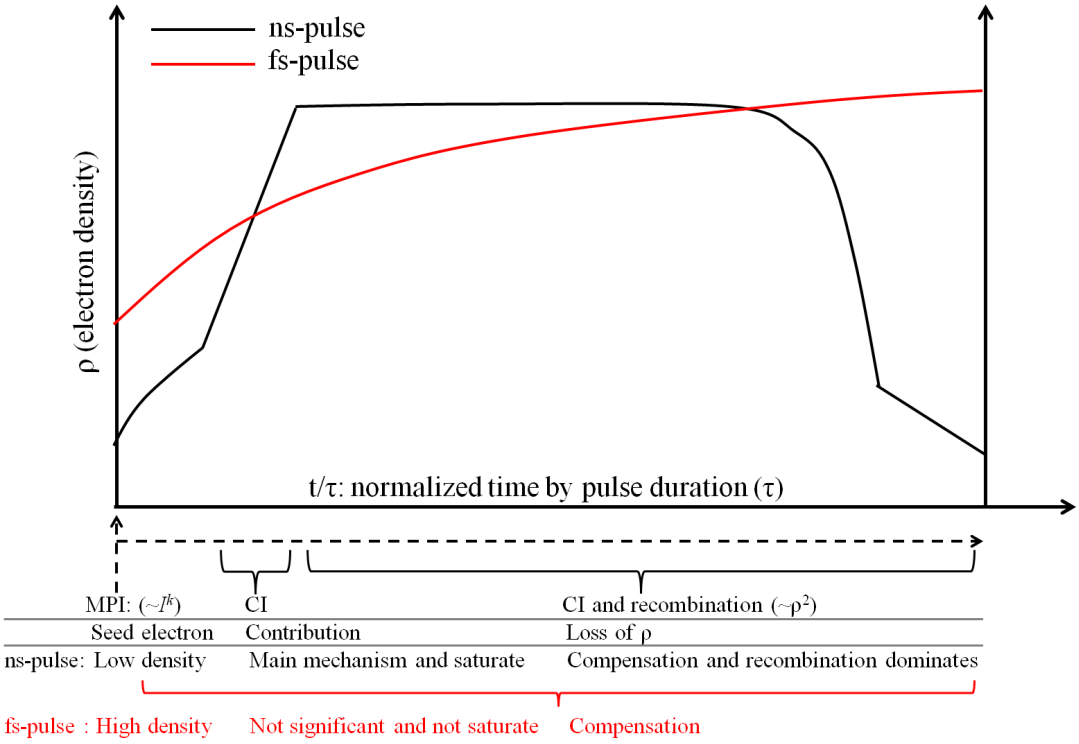

Figure 1.5: Evolution of free electron density for ns-pulse and fs-pulse. MPI: multiphoton ionization. CI: cascade ionization. τ: laser pulse duration. In ns-pulse optical breakdown process, CI increases ρ rapidly in very short time. The recombination of free electron and CI balance out and then recombination dominates at some point. Because free electron density for fs-pulse at the beginning is high due to the high intensity of fs-laser beam and the doubling time of electron for CI is much longer than laser pulse duration, MPI dominates during fs-pulse optical breakdown.

Lastly, the relation between the pulse duration and optical breakdown characteristic are compared [61]. Spot size at the beam focus and the fluence of laser beam decreases dramatically from ns-pulses to fs-pulses (Table 1.4).

Pulse duration	Wave length (nm)	Spot diameter (μm)	Intensity$\times 10^{11}$ ($W.cm^{-2}$)	Fluence ($J.cm^{-2}$)
76ns	750	20	0.23	1750
6ns	1064	5.5	0.66	398
300fs	580	5.0	47.6	1.4
100fs	580	4.4	111	1.1

Table 1.4: Spot size and breakdown thresholds of ns-pulse and fs-pulse.

1.4.2 Applications of optical breakdown in ophthalmology

The effects of the laser light on ocular tissues such as the retina should be studied carefully. However, one positive indication that our approach to measure the mechanical properties of ocular tissues using a laser-induced microbubble is safe in terms of laser light exposure to the human eye is that lasers are already widely used in ophthalmology [62, 63].

When lasers are used in clinical applications, it is very important to characterize the nature of the application. For nanosecond lasers, ns-pulse-induced optical breakdown has a high efficacy of energy deposition and a high conversion rate of light energy into mechanical energy [61]. Thus, ns-pulse is suitable for laser surgeries which need disruptive effects. For example, posterior capsulotomy needs high energy to make a long cut on the lens capsule. Thus, ns-pulses are more practical due to their disruptive characteristics [64]. Ultrashort laser pulses, for example femtosecond laser pulses (fs-pulses), have a lower energy deposition efficacy and a lower conversion rate from the laser light to mechanical energy. Thus, the collateral tissues around the focus of the laser beam suffer less damage. Two applications of fs-pulses in ophthalmology are explained

in the following sections. These applications need a very high precision and a low disruption to the collateral tissues.

1.4.2.1 LASIK

Refractive corneal laser surgery (Laser in Situ Keratomileusis, LASIK) treats eyes with myopia and hyperopia by changing the refractive power. Changing the curvature of the anterior part of the cornea to provide suitable refractive power is performed with ultraviolet photoablation from the excimer laser. To give access to deeper corneal tissue to the excimer laser, a corneal flap is made with the mechanical blade (microkeratome). The application of optical breakdown can replace the mechanical blade with an ultrafast laser because of its better precision and predictability [65-67]. Ultrafast laser systems have successfully entered the refractive surgery market since IntraLase introduced its first commercial system in 2001 [68].

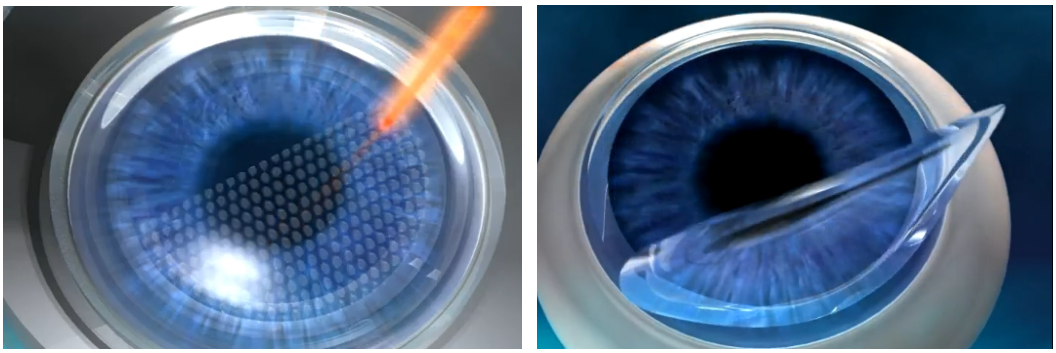

Figure 1.6: Making a corneal flap using femtosecond laser-induced photodiruption in cornea during LASIK. Captured images of a video at the Bloomberg Eye Center (Columbus, Ohio) website.

1.4.2.2 Femtosecond lentotomy

As discussed in Chapter 1.2, presbyopia starts developing in aged humans due to the stiffness increase of the crystalline lens. To provide flexibility to the crystalline lens

for accommodation, laser-induced incisions are introduced as a novel technique [69, 70]. Further investigations of presbyopia treatment have been done [1-3, 18, 71, 72]. Making different cutting planes inside the crystalline lens provides more flexibility to the crystalline lens. Fig. 1.7 shows the femtosecond laser-induced steering pattern in porcine lens.

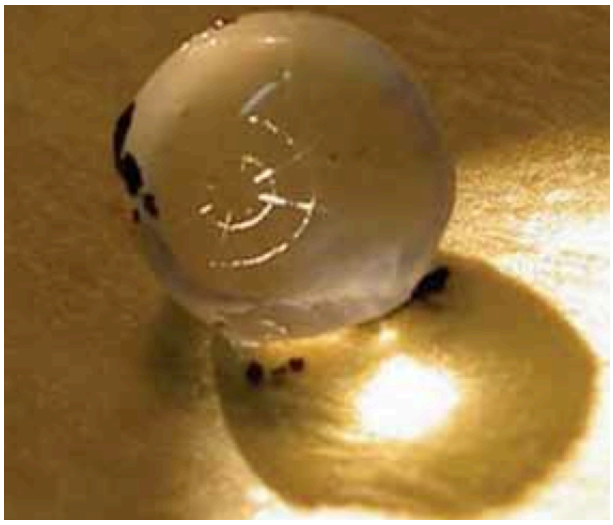

Figure 1.7: Steering wheel pattern in porcine lens after femtosecond lentotomy. This picture is used by the courtesy of Dr. Georg Gerten in Augenklinik am Neumarkt in Cologne, Germany.

1.5 ACOUSTIC RADIATION FORCE

Static elastography surfers from various artifacts due to unknown boundary conditions [73]. Acoustic radiation force is used to palpate inner tissues or objects remotely to investigate the elastic properties of soft tissues. Acoustic radiation force is generated when a sound wave is absorbed or reflected by an object. The acoustic radiation pressure is found useful in many applications, such as ultrasound imaging and tissue mechanical property measurements. The displacement induced at focus as a function of time can be linked to the local viscoelastic properties of the tissue [74, 75].

Among various techniques to measure mechanical properties of tissues noninvasively, radiation force has been investigated greatly during the last few decades as a means of a palpation tool for imaging soft tissues where external forces cannot reach. Recent applications have opened a variety of areas including shear wave elasticity imaging (SWEI) [76], acoustic radiation force impulse imaging (ARFI) [77-80], supersonic shear imaging [81-83], sonorheometry [77, 84-86], and vibroacoustography [75, 87, 88].

The original theory of acoustic radiation pressure was proposed by Rayleigh [89]. Brillouin investigated radiation pressure due to reflection and absorption on a plane [90]. King obtained the exact formula for the radiation force for the sphere in a gaseous medium with arbitrary densities [91]. Westervelt considered scattering and absorption on a target by using momentum conservation [92]. Radiation pressure on a pulsating bubble in a sound field was also considered [93, 94]. In this dissertation, I considered radiation force due to the nonlinearity of the medium. When an object (laser-induced microbubble) is travelling in a viscoelastic medium by acoustic radiation force, the moving object undergoes Stokes'-type force [95], which will be explained in Chapter 2.

1.6 APPROACH

Microbubble-based acoustic radiation force was introduced as a technique to remotely measure the localized viscoelastic properties of soft tissues by combining microbubbles created by laser-induced optical breakdown and acoustic radiation force [27, 96-98].

In this approach, laser-induced microbubbles were displaced using a long acoustic pulse to interrogate the mechanical properties of *ex-vivo* porcine and human lenses [98, 99]. Elastic properties were evaluated based on the amplitude of the bubble displacement from its steady state. Such an approach assumes that the acoustic radiation force on the

bubble surface is known or deduced by experiments or analytical calculations. For example, the radiation force can be estimated by matching the measured displacement of a laser-induced microbubble in a human lens with the same displacement observed in a phantom study [99]. However, the evaluation of the magnitude of radiation force is generally a challenging task due to the attenuation of ultrasound waves in tissue and unknown differences in acoustic impedances between tissue and the microbubble. In this dissertation, I propose to use a short acoustic impulse to estimate elasticity using timed characteristics of the microbubble motion [100]. Moreover, by comparing the displacements of a microbubble calculated by a theoretical model and measured by experiments, I could estimate the mechanical properties of soft tissues quantitatively [100-103].

My research collaborators theoretically investigated the motion of round objects such as solid spheres and bubbles within a viscoelastic medium subjected to an acoustic radiation force [103]. Static and transient responses of these round objects were obtained using linear approximation and analysis in both the frequency-domain and time-domain. The developed theoretical model was verified using experimental measurements on various solid spheres. The local elastic properties of the surrounding material were estimated from the temporal characteristics of the sphere motion and were found to be in good agreement with direct measurements [101, 102].

In this dissertation, I extend this previous work by employing laser-induced microbubbles as targets for acoustic radiation force in order to assess the mechanical properties of ocular structures such as the crystalline lens and the vitreous humor.

Reconstruction of the Young's modulus of soft tissues was performed by comparing experimentally measured times of maximum displacement of a microbubble with the values derived from a theoretical model of microbubble motion. When comparing the two, the scaling factor of acoustic radiation force was chosen to induce the best fit between the theoretical and measured data. Using this method, there was no need to measure the acoustic radiation force delivered to a laser-induced microbubble.

1.7 ORGANIZATION OF THIS DISSERTATION

Chapter 2 presents the theoretical background about the dynamics of a laser-induced microbubble in a viscoelastic medium under acoustic radiation force. This theoretical work was originally developed by Dr. Ilinskii [103].

From Chapters 3 to 4, the first hypothesis of this dissertation, stated in section 1.1, was confirmed. Experimental validation of the theory with gelatin phantoms is completed in Chapter 3. After a limitation of the current system was found, a new ultrasound system to accurately probe the dynamics of a microbubble was developed. The validation process of the high PRF ultrasound system using *ex vivo* bovine crystalline lenses is presented in Chapter 4.

Chapters 5 and 6 investigate the second hypothesis about the changes and variations of the mechanical properties of *ex vivo* animal ocular tissues with respect to age and location. *Ex vivo* animal crystalline lens and *ex vivo* porcine vitreous humor studies are presented in Chapters 5 and 6, respectively. Finally, conclusions and future work are addressed.

Chapter 2: *Microbubble dynamics in a viscoelastic medium*

In this chapter, a theoretical model of the dynamics of a microbubble interrogated by acoustic radiation force in a viscoelastic medium is considered. The original work was developed by Dr. Ilinskii [103] and I adopted it for my needs. It is worthwhile to take a look at three ways to estimate radiation force: bubble pulsation, the conservation of momentum, and the integration of the acoustic field on an object's surface. Finally, the derivation of the microbubble dynamics under acoustic radiation force is presented.

2.1 ACOUSTIC RADIATION FORCE

2.1.1 Bubble pulsation

Radiation force on a bubble in a standing wave is now considered. A pressure gradient, such as a standing wave field, induces bubble pulsation. In linear oscillation, bubble pulsation is in-phase with driving acoustic pressure and two main frequencies, the bubble's natural frequency and the driving frequency, should appear. If sufficiently high acoustic pressure is applied, the pulsation of a bubble becomes nonlinear. In that case, the bubble pulsates with great amplitude due to the nonlinear oscillations. However, before the driving acoustic pressure reaches a certain level, the bubble is still in stable oscillations. If the applied pressure amplitude exceeds a certain point, the bubble's radius grows dramatically and then suddenly collapses. This is called transient cavitation.

The radiation force on the bubble can be expressed as

$$\vec{F}_{rad} = -\left\langle V \cdot \vec{\nabla} p \right\rangle, \tag{2.1}$$

where $< >$ denotes the time-average. $\vec{\nabla} p$ is pressure gradient and V is volume of a bubble. $\vec{F}_{rad}$ is radiation force on a bubble (primary Bjerknes force). Using a linear approximation of the oscillations of bubble radius (equation (2.2)), the bubble radius is

$$R = R_0 + R' ,$$

(2.2)

where R is total radius of a bubble and R_0 and R' are equilibrium and small oscillation radius of a bubble, respectively. The standing wave is expressed as

$$p = p_0 \sin kx \cdot \sin \omega t , \tag{2.3}$$

where p_0 is the acoustic pressure amplitude of the incident plane wave and kx and ωt represent spatial and time variations of the incident plane wave, respectively.

By substituting equation (2.2) into equation (2.1) and Rayleigh-Plesset equation, equation (2.1) and R' becomes

$$\vec{F}_{rad} = -4\pi R_0^2 \left\langle R' \cdot \vec{\nabla} p \right\rangle \tag{2.4}$$

$$R' = \frac{p_0 \sin kx}{\rho R_0 (\omega^2 - \omega_0^2)} \sin \omega t , \tag{2.5}$$

where ρ denotes the density of the medium and γ denotes the specific heat ratio. $\omega_0^2 \left(= {3\gamma p_0}/{\rho R_0^2} \right)$ is the Minnaert resonance frequency. Using equation (2.4) and (2.5), the radiation force on a bubble in a standing wave field is

$$\vec{F}_{rad} = \frac{\pi V_0 p_0^2 \sin 2kx}{2\gamma \lambda P_0 (1 - {\omega^2}/{\omega_0^2})} ,$$

(2.6)

where $V_0 \left(= {}^{4\pi R_0^3}/_3\right)$ is the equilibrium volume of a bubble and λ is the wavelength of sound field. P_0 is the hydrostatic pressure of the medium. Notably, if the bubble is smaller than resonance size, the bubble moves to the pressure anti-node and vice versa.

2.1.2 Conservation of momentum

To estimate the radiation force, conservation of momentum can be used [92]. The momentum transfer only occurs due to absorption with the following assumption. First, an object is a Rayleigh scatterer (the diameter of an object is much smaller than the wavelength). Secondly, the object is spherical. Last, no momentum transfer by scattering effects exists. If these assumptions are valid, the radiation force on a bubble due to the incident wave is

$$F_{rad} = \frac{\langle W \rangle}{c_0}, \tag{2.7}$$

where W is total radiated and absorbed acoustic power and c_0 is speed of sound. By considering the pressure in far field [104], acoustic radiation force is defined as

$$F_{rad} = \frac{\rho \langle \ddot{V}^2 \rangle}{4\pi c_0^2}, \tag{2.8}$$

where $\ddot{V}^2$ is the second derivative of the bubble volume with respect to time.

Acoustic streaming is mainly about the tissue absorption of the wave. Some applications using acoustic streaming have been found [77]. Acoustic streaming can be derived from the conservation of momentum, too. Assuming conditions of slow flow of the medium (Stoke's flow), incompressibility of the medium and time averaging (< >), the acoustic streaming force is defined as

$$\vec{F} = \vec{\nabla}\langle P \rangle - \mu \nabla^2 \langle \vec{u} \rangle, \tag{2.9a}$$

where $\vec{F} = -\left\langle \rho(\vec{u} \cdot \vec{\nabla})\vec{u} + \vec{u}\vec{\nabla} \cdot \rho\vec{u} \right\rangle$.

(2.9b)

In equations (2.9a) and (2.9b), $\vec{F}$ is the negative of the time-averaged rate of increase of momentum per unit volume in an element of fluid. μ is the coefficient of shear viscosity of the fluid. P, $\vec{u}$, and ρ are pressure, density, and velocity at any point at the specific instant. By considering the second order terms, P, $\vec{u}$, and ρ can be expressed as

$$\begin{aligned} P &= P_0 + p_1 + p_2 + \cdots \\ \rho &= \rho_0 + \rho_1 + \rho_2 + \cdots \\ \vec{u} &= 0 + \vec{u}_1 + \vec{u}_2 + \cdots \end{aligned},$$

(2.10)

where P_0 and ρ_0 are ambient pressure and density, respectively. p_1, ρ_1, and $\vec{u}_1$ and p_2, ρ_2, and $\vec{u}_2$ are first-order and second-order approximations of corresponding variables, respectively. After substitute equation (2.10) into (2.9), equation (2.9) can be written as

$$\vec{F}_2 = \vec{\nabla} p_2 - \mu \nabla^2 \vec{u}_2, \tag{2.11a}$$

where $\vec{F}_2 = -\rho_0 \left\langle (\vec{u}_1 \cdot \vec{\nabla})\vec{u}_1 + \vec{u}_1 \vec{\nabla} \cdot \vec{u}_1 \right\rangle$. (2.11b)

Assuming plane wave propagation, the acoustic streaming force on tissue becomes

$$\vec{F}_2 = \frac{2I\alpha}{c_0}, \tag{2.12}$$

where α is absorption coefficient of tissue and I is the acoustic intensity of the beam. Equation (2.12) represents streaming force.

2.1.3 Integration of the acoustic field on the object surface

The last method to define acoustic radiation force is to integrate the wave field on an object surface. An acoustic radiation force is induced by the radiation stress acting on a spherical surface. Even though King [91] made significant progress related to describing radiation pressure on spheres, he did not take into account the compressibility of the sphere. Hasegawa and Yosioka [105] dealt with more general cases: a compressible fluid sphere in a fluid.

Radiation force function of a sphere for the plane progressive sound field is defined as

$$Y_p = \langle F \rangle / \pi a^2 \bar{E} \quad . \tag{2.13}$$

Y_p depends on the properties of the sphere and the surrounding medium such as ka, where k is a wave number of the incident wave and a is the radius of the sphere. πa^2 is the projected area of the sphere. $\bar{E}$ is the mean energy density in the plane progressive wave. Using equation (2.13), one can define the radiation pressure on the sphere ($\langle F \rangle$).

2.2 THE DYNAMICS OF A MICROBUBBLE UNDER ACOUSTIC RADIATION FORCE

In the theoretical model, I assume that the surrounding medium is viscoelastic, homogeneous, and isotropic. I further assume that the medium is incompressible as is the case for most soft tissues [106]. The problem at hand is axisymmetric and no force

dependence in the azimuthal direction exists. Therefore, the deformation of microbubble is symmetric along the axial direction.

The equation of motion for the incompressible medium [95] in time-domain is:

$$-\nabla P + \mu\nabla^2 U + \eta\nabla^2 \frac{\partial U}{\partial t} = \rho \frac{\partial^2 U}{\partial t^2}, \tag{2.14}$$

where P is internal pressure, U is the displacement vector, μ and η are the shear elastic modulus and shear viscosity, respectively, ϱ is medium density and t is time. Young's modulus (E) and shear elasticity modulus (μ) have a simple relation for homogeneous isotropic materials such that $E = 2\mu(1+\nu)$, where ν is Poisson's ratio. For an incompressible medium where Poisson's ratio is 0.5, Young's modulus is three times larger than the shear modulus. The polar axis of the spherical system of coordinates (r, θ, ϕ) is along the force vector (i.e. an angle θ is between a radius vector and displacement), and $U = (U_r, U_\theta, 0)$. The external force applied to the displaced spherical object is [104]:

$$F^{(ext)} = -2\pi R^2 \int_0^\pi (\sigma_{rr}\cos\theta - \sigma_{r\theta}\sin\theta) sin\theta d\theta, \tag{2.15}$$

where σ_{rr} and $\sigma_{r\theta}$ are stress tensor components at the surface of the object:

$$\sigma_{r\theta} = \left(\mu + \eta\frac{\partial}{\partial t}\right)\left(\frac{\partial U_\theta}{\partial r} - \frac{U_\theta}{r} + \frac{1}{r}\frac{\partial U_r}{\partial \theta}\right),$$

$$\sigma_{rr} = -P + 2\left(\mu + \eta\frac{\partial}{\partial t}\right)\frac{\partial U_r}{\partial r}. \quad (2.16)$$

The boundary conditions at the bubble surface (r=R) are:

$$\sigma_{r\theta} = 0\,,\ -\sigma_{rr} + P_r = P_0, \quad (2.17)$$

where R is the radius of bubble, P_r is acoustic radiation pressure acting on the surface of the bubble and P_0 is an internal gas pressure [104]. Since pressure P and, consequently, σ_{rr} are defined up to a constant, the internal gas pressure P_0 may be set equal to zero.

The solution of equations (2.14) and (2.16) is found in the frequency domain, and displacement of a microbubble in time domain is obtained by taking inverse Fourier transform from the spectral solution. The frequency-domain representation of equation (2.14) is given by:

$$-\nabla p + (\mu - i\omega\eta)\nabla^2\boldsymbol{u} = -\rho\omega^2\boldsymbol{u}, \quad (2.18)$$

where p and $\boldsymbol{u}$ are the Fourier transforms of P and $\boldsymbol{U}$, ω is an angular frequency.

In this study I consider that the external force applied to the bubble $F^{(ext)}$is impulsive:

$$F^{(ext)} = \begin{cases} F_0 & 0 \le t \le t_0 \\ 0 & t \ge t_0 \end{cases}, \tag{2.19}$$

where t_0 is the duration of acoustic radiation pulse. The frequency domain representation of (2.19) is:

$$F_\omega{}^{(ext)} = -\frac{iF_0}{\omega}\left(e^{i\omega t_0} - 1\right). \tag{2.20}$$

I consider u_ω as a spectral component of low frequency displacement and are looking for the bubble surface displacement components (for $r = R$) in the form:

$$\begin{aligned} u_r &= u_\omega \left(1 - \frac{1}{3} ikR\right)\cos\theta, \\ u_\theta &= -\frac{1}{2} u_\omega \left(1 + \frac{1}{3} ikR\right)\sin\theta, \end{aligned} \tag{2.21}$$

where $u_\omega = \left(-\frac{ik}{R}\tilde{a}e^{ikR}\right)$ is the low frequency displacement [104], k is the wave number of the shear wave and defined as $k = \omega/\left(c_t\sqrt{1 - i\omega\eta/\mu}\right)$ and $c_t = \sqrt{(\mu/\rho)}$. The sign of k is defined by the condition $Im(k) > 0$ because displacement of medium must approach zero away from the bubble. The constant $\tilde{a}$ is defined by the boundary conditions (2.17). Taking into account the boundary conditions (2.17) as well as

equations (2.15) and (2.16), the relationship between the spectral components of the displacement and force is:

$$F_{\omega}^{(ext)} = 4\pi(\mu - i\omega\eta)Ru_{\omega}\left(1 - ikR - \frac{1}{6}k^2R^2 + \frac{1}{18}ik^3R^3\right). \tag{2.22}$$

By combining algebraic equations (2.20) and (2.22), the solution in terms of u_{ω} is given by

$$u_{\omega} = -\frac{iF_0(e^{i\omega t_0} - 1)}{4\pi\omega(\mu - i\omega\eta)R(1 - ikR - \frac{1}{6}k^2R^2 + \frac{1}{18}ik^3R^3)} \ . \tag{2.23}$$

By taking inverse Fourier transform, time domain components U_r and U_{θ} are obtained:

$$U_r = -\frac{iF_0\cos\theta}{12\pi R}\mathfrak{F}^{-1}\left[\frac{\left(e^{i\omega t_0} - 1\right)(3 - ikR)}{\omega(\mu - i\omega\eta)(1 - ikR - \frac{1}{6}k^2R^2 + \frac{1}{18}ik^3R^3)}\right], \tag{2.24}$$

$$U_{\theta} = \frac{iF_0\sin\theta}{24\pi R}\mathfrak{F}^{-1}\left[\frac{\left(e^{i\omega t_0} - 1\right)(3 + ikR)}{\omega(\mu - i\omega\eta)(1 - ikR - \frac{1}{6}k^2R^2 + \frac{1}{18}ik^3R^3)}\right],$$

where $\mathfrak{F}^{-1}[f(\omega)] = \frac{1}{2\pi}\int_{-\infty}^{\infty} f\,(\omega)e^{-i\omega t}d\omega$ denotes inverse Fourier transform. To compare the theoretical model and experimental data the displacements should be transformed from spherical to Cartesian coordinates:

$$U_z = U_r\cos\theta - U_\theta\sin\theta,$$

$$U_x = U_r\sin\theta + U_\theta\cos\theta, \tag{2.25}$$

where θ is the angle between z-axis and r-axis and increases in the counter clock wise direction. The displacement is not constant on the bubble surface as the bubble could be deformed by acoustic radiation force. Thus, U_x is the displacement in the normal direction with respect to the force vector and U_z is the displacement along the force direction. If the ultrasound imaging transducer and the excitation transducer are aligned in the z-axis, then U_z corresponds to axial displacement of the microbubble. There is some freedom in the choice of the angle θ, but in our calculations, it is assumed that θ = 0. Thus, the theoretically predicted U_z of microbubble is used to find the best fit between theory and experimental measurements.

It is important to note that the problem has been formulated in linear approximation, assuming that the displacement of the bubble does not exceed one and half times the bubble radius [104]. Otherwise, the deformation of the bubble becomes significant and the influence of surface tension should be taken into account. Surface tension reduces the bubble deformation, especially for small bubbles and makes the bubble behave more like a solid sphere with small density.

2.3 THE BEHAVIOR OF A MICROBUBBLE

In this section, the behavior of a laser-induced microbubble in a viscoelastic medium under acoustic radiation force is simulated with respect to microbubble radius

(R), duration of acoustic pulse (t_0), Young's modulus (E), and shear viscosity (η). This process can provide a general idea of the dynamics of a microbubble under different circumstances. Table 2.1 indicates four different cases. For each case, the displacements of a microbubble with respect to time, time for the microbubble to reach its maximum displacement (t_{max}), and maximum displacement (U_{max}) are considered.

	R (μm)	t_0 (μm)	E (kPa)	η (Pa•s)
Case I	*10~100*	20	5	0.06
Case II	50	*20~400*	5	0.06
Case III	50	20	*1~20*	0.06
Case IV	50	20	5	*0.1~1.0*

Table 2.1: Parameters for case studies of the dynamics of a laser-induced microbubble. Microbubble radius (R), duration of acoustic pulse (t_0), Young's modulus (E), and shear viscosity (η) are changed to explore the dynamics of a microbubble.

2.3.1 Case I: changes in microbubble radius

The dependence of the displacements of a microbubble on bubble radius is now considered. The microbubble radius changes from 10 to 100 μm while other parameters are fixed as shown in Table 2.1.

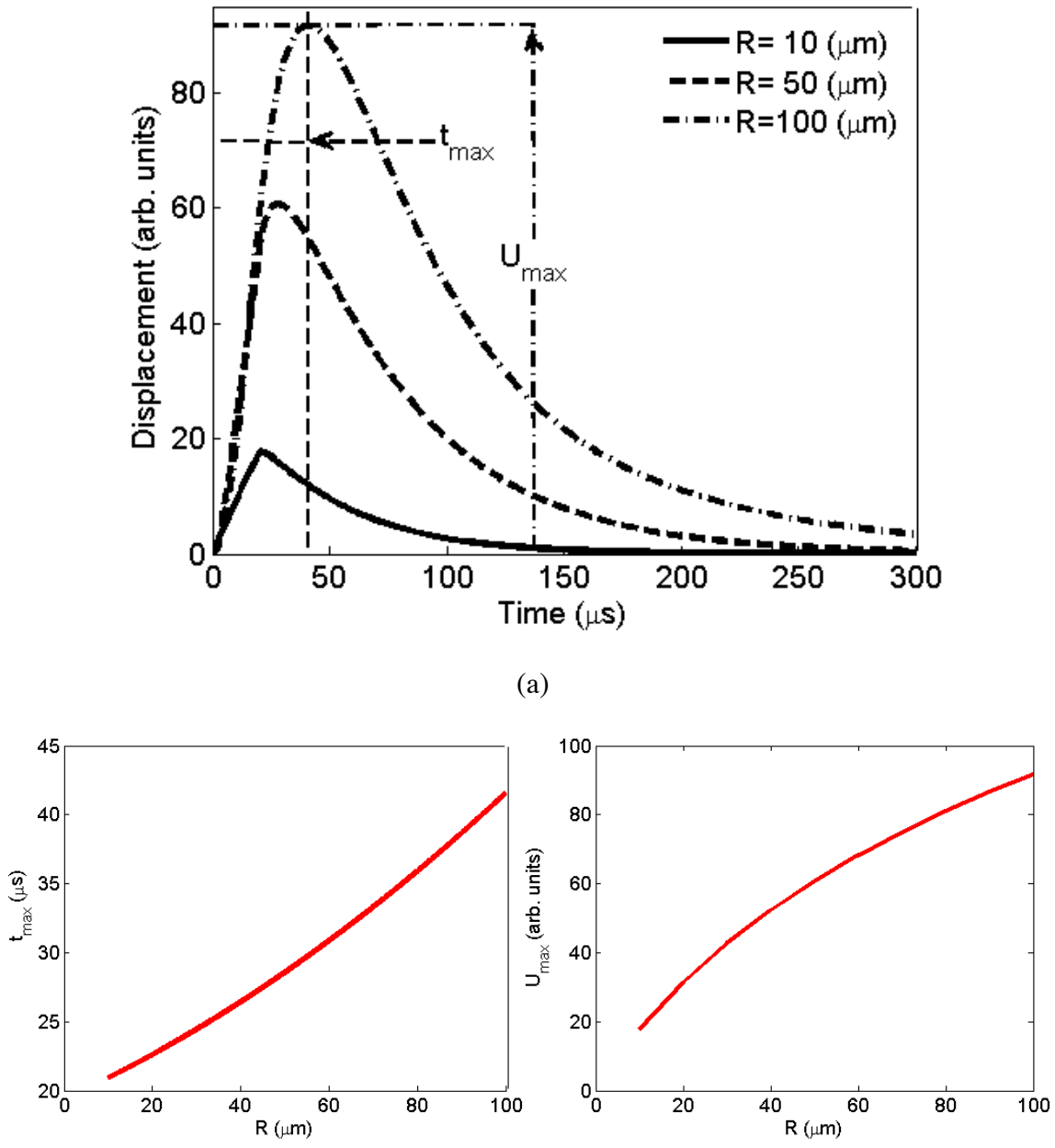

Figure 2.1: Investigation of case I (Table 2.1). (a) The displacements of microbubbles with radii (R= 10, 50, and 100 μm) in response to acoustic pulse duration of 20 μs. (b) t_{max} dependence with respect to bubble radius. (c) U_{max} dependence with respect to bubble radius. t_{max} and U_{max} are shown in (a).

Because larger microbubbles have larger inertia (=larger mass) than smaller microbubbles, t_{max} increases for larger microbubbles (Fig. 2.1 (b)) after acoustic pulse was removed at 20 μs (t_0). Because the cross-section increases as the microbubble radius becomes larger, acoustic radiation force acting on the microbubble increases for larger microbubbles. Thus, U_{max} increases.

2.3.2 Case II: changes in duration of acoustic pulse

The dependence of the displacements of a microbubble on the duration of acoustic pulse (t_0) is investigated. t_0 changes from 20 to 400 μs while other parameters are fixed as shown in Table 2.1.

After t_0 reaches a certain value, the displacement of a microbubble reaches a steady-state value (Figs. 2.2(a) and (c)). This is because the reaction force from the surrounding medium to the microbubble restrains the microbubble in moving further. A similar phenomenon happens to t_{max}. As shown in Fig. 2.2 (b), t_{max} merges to t_0 as t_0 increases. Thus, t_{max} and t_0 cannot be distinguished if t_0 goes beyond a certain value.

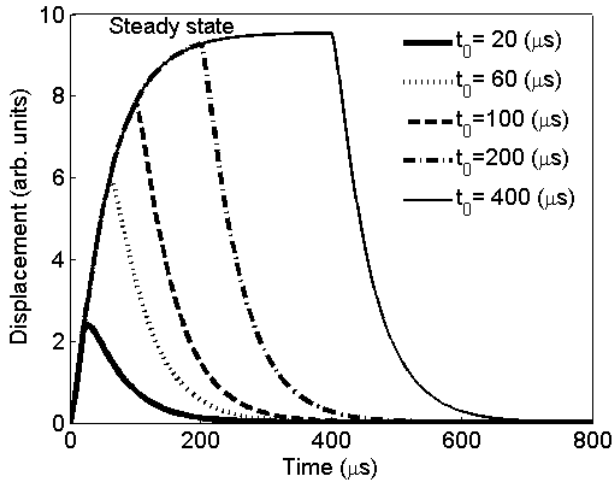

(a)

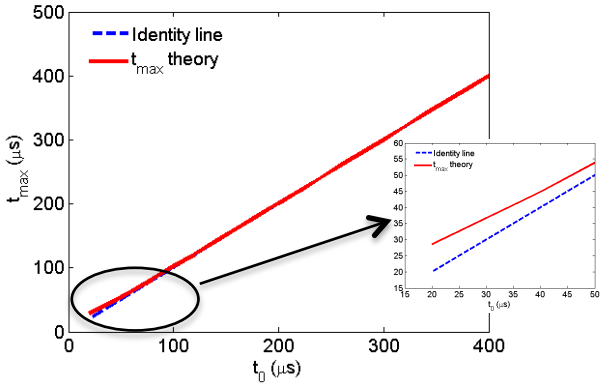

(b)

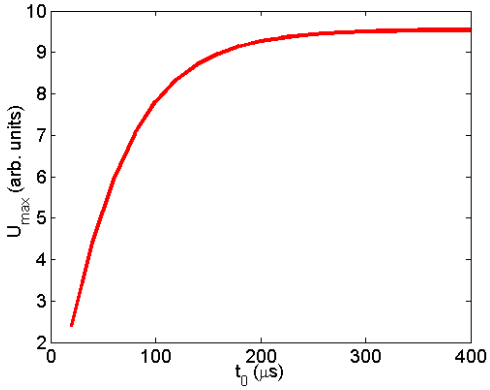

(c)

Figure 2.2: Investigation of case II (Table 2.1). (a) The displacements of 50 μm radius microbubble in response to acoustic pulse durations of 20, 60, 100, 200, 400 μs. (b) t_{max} dependence with respect to the duration of acoustic pulse (t_0). (c) U_{max} dependence with respect to the duration of acoustic pulse (t_0).

2.3.3 Case III: changes in Young's modulus

The dependence of the displacements of a microbubble on Young's modulus (*E*) is presented. *E* changes from 1 to 20 kPa while other parameters are fixed as shown in Table 2.1.

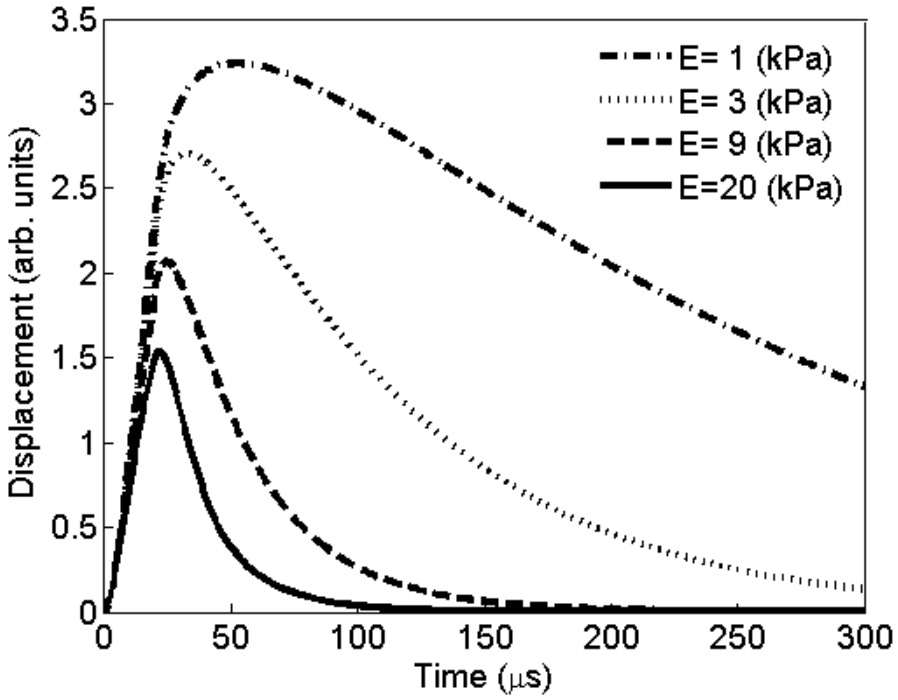

(a)

Figure 2.3: Investigation of case III (Table 2.1). (a) The displacements of 50 μm radius microbubble in response to acoustic pulse durations of 20 μs with different Young's modulus (*E*= 1, 3, 9, 20 kPa). (b) t_{max} dependence with respect to Young's modulus (*E*). (c) U_{max} dependence with respect to Young's modulus (*E*).

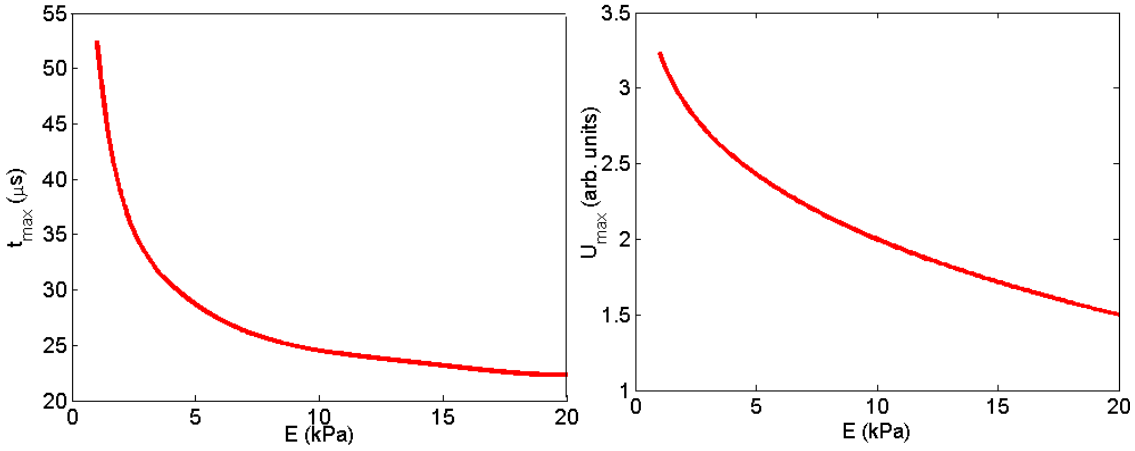

(b) (c)

Figure 2.3: Investigation of case III (Table 2.1). (a) The displacements of 50 μm radius microbubble in response to acoustic pulse durations of 20 μs with different Young's modulus (E= 1, 3, 9, 20 kPa). (b) t_{max} dependence with respect to Young's modulus (E). (c) U_{max} dependence with respect to Young's modulus (E).

A hard medium has a stronger reaction force to a moving microbubble (Figs. 2.3(a) and (c)). Moreover, t_{max} decreases exponentially if E increases from 1 to 20 kPa (Fig. 2.3(b)). For a hard medium, it is difficult to tell the difference between t_{max} and t_0.

2.3.4 Case IV: changes in shear viscosity

The dependence of the displacements of a microbubble on shear viscosity (η) is considered. η changes from 0.1 to 1.0 Pa•s while other parameters are fixed as shown in table 2.1.

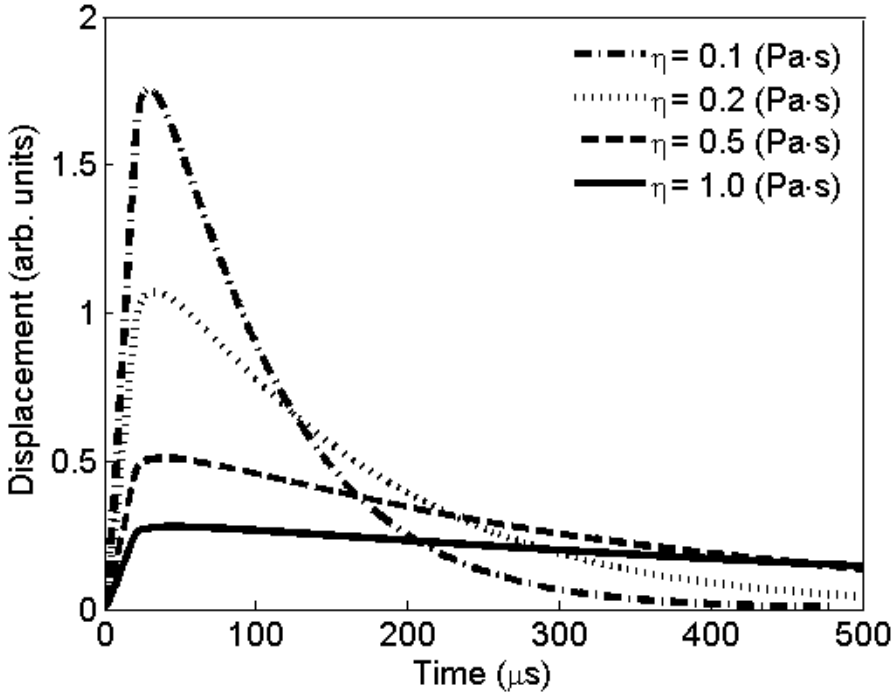

(a)

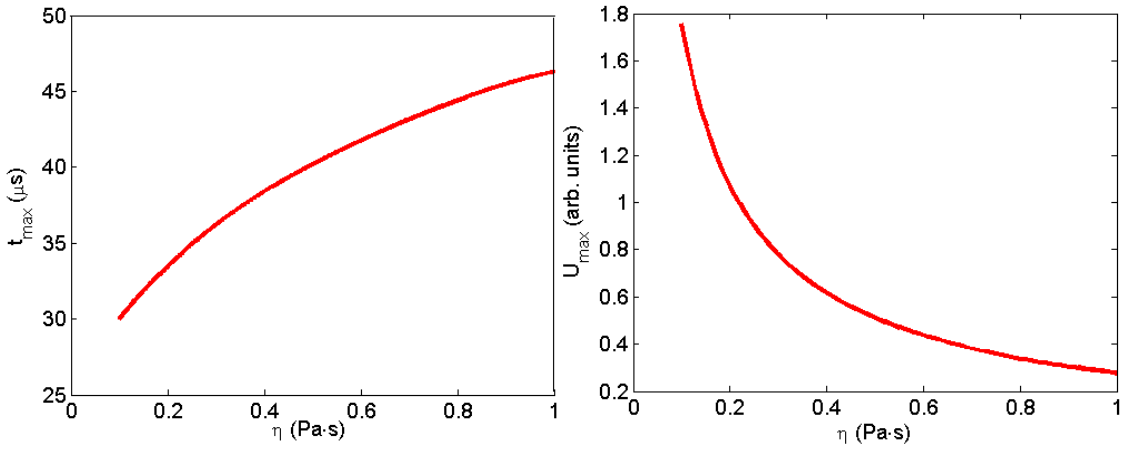

(b) (c)

Figure 2.4: Investigation of case IV (Table 2.1). (a) The displacements of 50 μm radius microbubble in response to acoustic pulse durations of 20 μs with different shear viscosity (η = 0.1, 0.2, 0.5, 1.0 Pa•s). (b) t_{max} dependence with respect to shear viscosity (η). (c) U_{max} dependence with respect to shear viscosity (η).

Shear viscosity acts as a damping. The higher the shear viscosity is, the longer the t_{max} and the smaller the U_{max} are (Fig. 2.4). After the acoustic pulse is terminated, the bubble needs much more time to reach its t_{max} and come back to its original position if η is large.

From the case studies above, it is important to pick the appropriate values of the duration of acoustic pulse (t_0) and microbubble radius (R) for experiments. This will determine the accuracy and the precision of the approach suggested in this dissertation.

Chapter 3: *Validation of a theoretical model: phantom study*

ABSTRACT

An approach to assess the mechanical properties of a viscoelastic medium using laser-induced microbubbles is presented. To measure mechanical properties of the medium, dynamics of a laser-induced cavitation microbubble in viscoelastic medium under acoustic radiation force was investigated. An objective lens with a 1.13 numerical aperture (NA) and an 8.0 mm working distance was designed to focus a 532 nm wavelength nanosecond pulsed laser beam and to create a microbubble at the desired location. A 3.5 MHz ultrasound transducer was used to generate acoustic radiation force to excite a laser-induced microbubble. Motion of the microbubble was tracked using a 25 MHz imaging transducer. Agreement between a theoretical model of bubble motion in a viscoelastic medium and experimental measurements was demonstrated. Young's modulii reconstructed using the laser-induced microbubble approach were compared with those measured using a direct uniaxial method over the range from 0.8 to 13 kPa. The results indicate good agreement between methods. Thus, the proposed approach can be used to assess the mechanical properties of a viscoelastic medium

3.1 INTRODUCTION

In laser-based ophthalmic microsurgery, micrometer-size bubbles are used to precisely cut tissue in the eye [107-111]. During the laser-tissue interaction, the focused laser radiation in tissue is absorbed, and a microbubble is formed where the intensity of the electromagnetic field exceeds the threshold of optical breakdown [111, 112]. One of the applications of laser-induced microbubbles in ophthalmology is refractive vision correction surgery to correct myopia, hyperopia, and astigmatism [67, 111]. Accurate

corneal flaps can be created by using laser-induced microbubbles, providing a better surgery outcome [113, 114].

While laser-tissue ablation and associated formation of microbubbles play an increasingly important role in laser-based microsurgery, microbubbles could also be used to obtain information about elastic properties of ocular tissues [99]. According to the most widely accepted theory of presbyopia, the age-related loss of accommodation is attributed to gradual loss of lens elasticity. Furthermore, there is evidence that nuclear cataract lenses are generally harder than normal lenses [28, 35, 40]. Thus, observing the changes of tissue properties may be used as a tool to diagnose disease and improve the outcome of treatment. Due to high acoustic reflectivity on the bubble surface, a microbubble-based acoustic radiation force technique can provide greater radiation force than an absorption-based acoustic radiation force technique [76, 77, 115]. Therefore, displacement variations inside tissue can be effectively generated by the combined method. External local excitation permits the estimation of the local mechanical properties of tissue based on the analysis of the motion of a laser-induced microbubble because the dynamics of the motion of a microbubble are defined by the properties of the surrounding tissue [104].

A number of methods have been developed to estimate the mechanical properties of lenses: ultrasonic characterization of the lens using ultrasound wave attenuation [28]; compression tests [116]; application of radial force [31, 32]; hydrostatic or automated guillotine tests [35, 36]; uniaxial test[34]; cone penetration test [33]; and dynamic mechanical analysis [40, 117, 118]. The results of these measurements demonstrate that

elasticity of the whole lens increases with age and the nucleus becomes stiffer than the cortex. It is reported that the lens has a Young's modulus of several tens of Pa to tens of kP [31-33, 40, 99]. However, most of these techniques to measure lens elasticity assume direct mechanical testing and usually can be used only *in vitro*. Among various techniques to measure mechanical properties of tissues noninvasively, radiation force has investigated greatly during last few decades as a means of a palpation tool for imaging soft tissues where external forces cannot reach. Recent applications have opened a variety of areas including shear wave elasticity imaging (SWEI) [76], acoustic radiation force impulse imaging (ARFI) [77-80], supersonic shear imaging [81-83], sonorheometry [77, 84-86], and vibroacoustography [75, 87, 88].

By combining microbubbles created by laser-induced optical breakdown and acoustic radiation force, microbubble-based acoustic radiation force was introduced as a technique to remotely measure the localized viscoelastic properties of the lens [96, 99]. In that approach, laser-induced microbubbles were displaced using a long acoustic pulse to interrogate the mechanical properties of *ex-vivo* porcine and human lenses [99]. Elastic properties were evaluated based on the amplitude of the bubble displacement from an equilibrium position. Such an approach assumes that the acoustic radiation force on the bubble surface is known or deduced by experiments or analytical calculations. For example, the radiation force can be estimated by matching the measured displacement of a laser-induced microbubble in a human lens with the same displacement observed in a phantom study [99]. However, the evaluation of the magnitude of radiation force is generally a challenging task due to the attenuation of ultrasound waves in tissue and

unknown differences in acoustic impedances between tissue and the microbubble. In this Chapter, I propose to use a short acoustic impulse to estimate elasticity using time characteristics of the microbubble's motion.

In the previous studies my collaborators theoretically investigated the motion of round objects such as solid spheres and bubbles within a viscoelastic medium subjected to an acoustic radiation force [103]. Static and transient responses of these round objects were obtained using linear approximation and analysis in both the frequency-domain and time-domain. The developed theoretical model was verified using experimental measurements on various solid spheres. The local elastic properties of the surrounding material were estimated from the temporal characteristics of the sphere's motion and were found to be in good agreement with direct measurements [101, 102].

In this Chapter, I extend our research by employing laser-induced microbubbles as targets for acoustic radiation force in order to assess the mechanical properties of tissue-mimicking phantoms. I measured the maximum displacement as well as the time it took to reach that value of a laser-induced microbubble under the acoustic radiation force. Reconstruction of the Young's modulus of the phantom was performed by comparing experimentally measured times of maximum displacement of a microbubble with the values derived from a theoretical model of microbubble motion. When comparing the two, the scaling factor of acoustic radiation force was chosen to induce the best fit between the theoretical and measured data. Using this method, there was no need to measure the acoustic radiation force delivered to a laser-induced microbubble. Experiments were performed on tissue-mimicking phantoms with Young's modulii from

0.8 to 13 kPa, which approximately corresponds to the elastic properties of the crystalline lens obtained from literature [40, 99, 116, 119, 120].

3.2 MATERIALS AND METHODS

To verify the theoretical model, the experiments were performed using laser-induced microbubbles in tissue-mimicking phantoms, containing 3% by weight gelatin (300 Bloom, type-A, Sigma-Aldrich, Inc., St. Louis, MO). In addition, cylindrical samples of 35 mm diameter and 16~18 mm height were made out of the same gelatin solution to be used in direct mechanical measurements with portable bench-top uniaxial tester In-Spec 2200 (Instron Inc., Morwood, MA). Prior to measurements, the phantoms and samples were kept together and followed the same experimental protocol to minimize any differences between the materials.

To validate the proposed approach experimentally, an experimental system was designed and built (Fig. 3.1). The overall system combined pulsed laser, objective lens, microscope, water container, excitation transducer, and imaging transducer.

A pulsed Nd:YAG laser (Polaris II, Fremont, CA) with 5 ns pulse duration, 532 nm wavelength, and 0.3 mJ energy was focused by a custom-built objective lens (1.13 numerical aperture (NA) and 8.0 mm working distance) to produce a microbubble inside the gelatin phantom. A high NA guaranteed that a laser-induced microbubble would be small and nearly spherical [109].

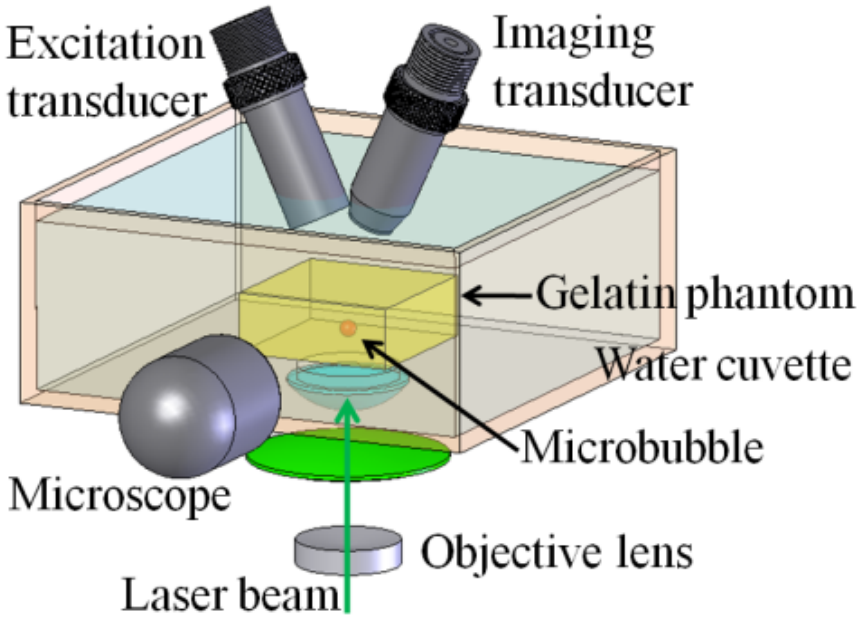

Figure 3.1: A schematic view of the experimental setup. A microbubble is produced by a focused laser beam. An excitation transducer generates acoustic radiation force on a microbubble. The motion of a microbubble is tracked by an imaging transducer. The size of the microbubble was monitored by an optical microscope.

The size of the microbubble was monitored by an optical microscope (Dino-Lite AM411T, Wirtz, VA) operating at 230x magnification. Example optical images of microbubbles captured during the experiments are presented in Fig. 3.2. The radii of microbubbles ranged from 13±2 to 258±2 μm. The uncertainty of the bubble radius came from four measurements in four different axes of the bubble.

A water cuvette with a hole for laser beam delivery was fixed to the standing post and the gelatin phantom attached to a translation stage was placed inside the water cuvette. The gelatin phantom was moved during the experiments to generate laser-

induced microbubbles at different locations in the phantom. A 3.5 MHz transducer (Valpey Fisher, Hopkinton, MA) and a 25 MHz imaging transducer (Olympus-NDT, Waltham, MA) with focal lengths of 25.4 mm were located at the top of the water cuvette with an angle of 20° with respect to a vertical line. Thus, the angle between 3.5 MHz and 25 MHz transducers was 40°. The foci of both transducers were aligned at the location of the microbubble.

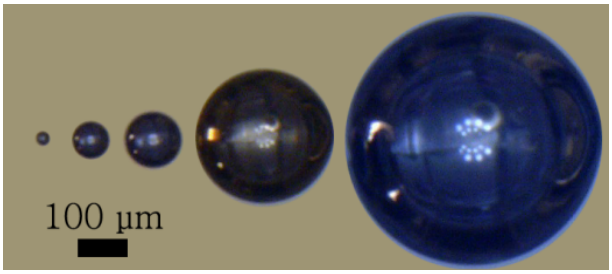

Figure 3.2: Typical microbubbles generated by pulsed laser (5 ns pulse duration, 532 nm wavelength, and 0.3 mJ energy). Pulsed laser was focused by using a 1.13 numerical aperture (NA) objective. Bubble radii are from 13 to 258 μm.

The 3.5 MHz excitation transducer (F/#= 4 and bandwidth= 60%), connected to RF power amplifier (ENI model 240L, ENI, Rochester, NY) with 50 dB gain, was used to generate pulsed acoustic radiation force to displace a laser-induced microbubble. The duration of the acoustic radiation pulse (t_0) was varied from 29 to 571 µs.

The 25 MHz imaging transducer (F/#= 4 and bandwidth= 51%), connected to a pulser/receiver (DPR 300 Pulser / Reciever, JSR Ultrasonics, Pittsford, NY) , was operated at pulse repetition frequency of 25 kHz in pulse-echo mode. Pulse-echo

ultrasound signals were saved at the data acquisition card (CompuScope 12400, GaGe Inc., Montreal, Canada) with 200 MSamples/sec for off-line processing. Therefore, radiofrequency (RF) raw data were comprised of trains of backscattered ultrasound echoes started 120 μs before the acoustic radiation pulse was launched. Arrival time of the first echo defined the initial location of the microbubble and changes in the arrival times of the following echoes determined microbubble displacement. RF raw data were used to define displacement of a microbubble by a cross-correlation speckle tracking method [121]. The Kernel size and search window for cross-correlation tracking were 375 μm and 1125 μm, respectively.

Comparison between theoretical calculations and experimental measurements of the motion of a laser-induced microbubble in the gelatin phantom was made to verify the developed theoretical model. Then, this model was used to reconstruct the elasticity of tissue-mimicking phantoms.

Theoretically calculated values of maximum displacement (U_{max}) and time required to reach the maximum displacement (t_{max}) of a laser-induced microbubble were compared with those obtained by experimental measurements for different values of acoustic radiation pulse duration (t_0) and various radii of a microbubble (R). Young's modulus (E), measured by uniaxial tester, was used in theoretical calculations. The value of the scaling factor of acoustic radiation force (F_0) was chosen to match experimentally observed displacements with theoretically calculated displacements. The shear viscosity was found by comparing decaying profiles of microbubble displacements from theory and experiments. The estimated value was 0.06 Pa·s which was used in all theoretical

calculations. The value corresponded to the results of our previous work, which was 0.1 Pa·s [102, 122]. The elastic properties were found to be almost independent from the shear viscosity in the measured range. Shear viscosity of porcine and human lens was investigated by another group and the values varied from 0.16±0.1 to 0.33 Pa·s [123].

In reconstruction, the Young's modulus was varied by gelatin concentrations. The gelatin concentrations used in the experiments were 1.4, 2.0, 3.0, 4.0, 5.0, 6.0, 7.0% by weight. Young's modulus of a viscoelastic medium was estimated using a laser-induced microbubble under acoustic radiation force by measuring the time of maximum displacement (t_{max}) [102, 122]. Then, it was compared to the Young's modulus measured by the uniaxial tester.

3.3 Results and Discussion

3.3.1 Experimental validation of theoretical model

Theoretically calculated and experimentally obtained displacements of a laser-induced microbubble with a radius of 258±2 μm are shown in Fig. 3.3a and Fig. 3.3b, respectively. The microbubble radius was measured with microscope (Fig. 3.1) and the measured radius was the average value of four different axes. The durations of applied radiation pulses were 29, 143, 286 and 571 μs. The arrows indicate the time when the force was turned off (i.e., the end of the acoustic pulse). The Young's modulus of the phantom measured using uniaxial tester was 4.37±0.26 kPa. As evident from Equation 2.24 in Chapter 2, microbubble displacement was scaled with the scaling factor of

acoustic radiation force (F_0). Therefore, F_0 in our model was chosen to match the experimentally observed displacements.

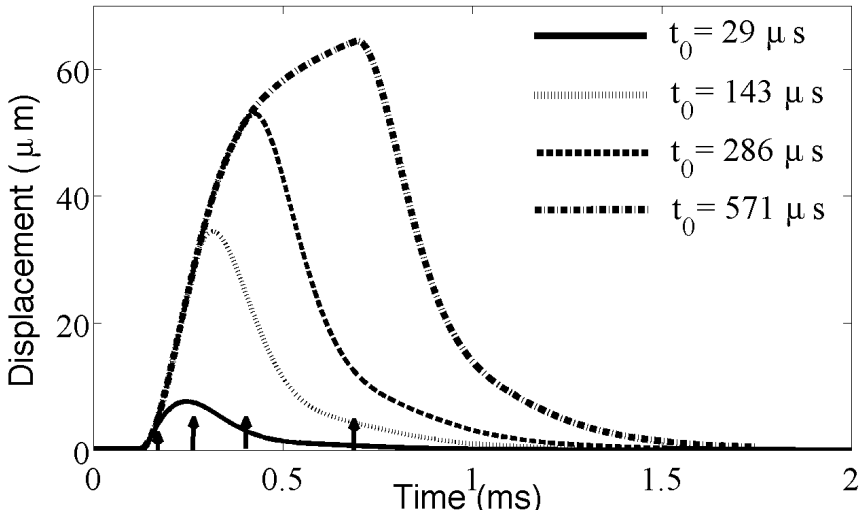

(a)

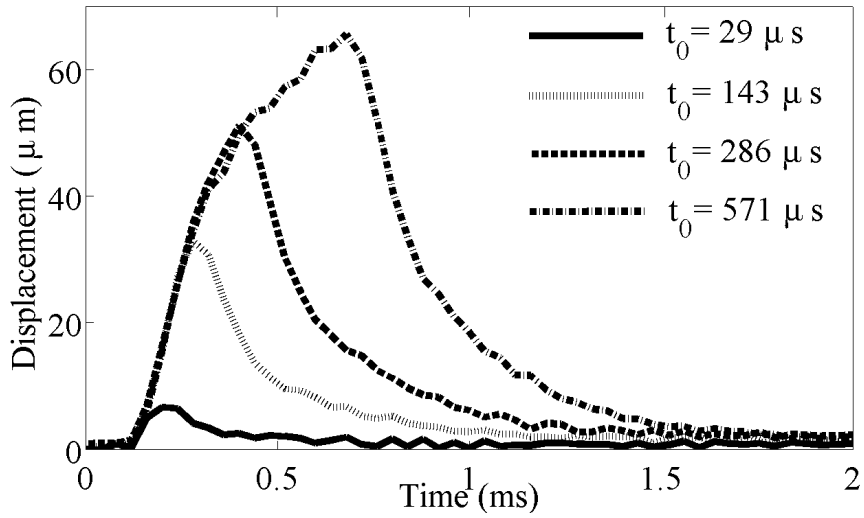

(b)

Figure 3.3: (a) Theoretically calculated and (b) experimentally obtained displacements (single measurement) of the microbubble in response to various durations of the acoustic pulse. The arrows represent the end of acoustic pulse. Bubble radius is 258±2 μm.

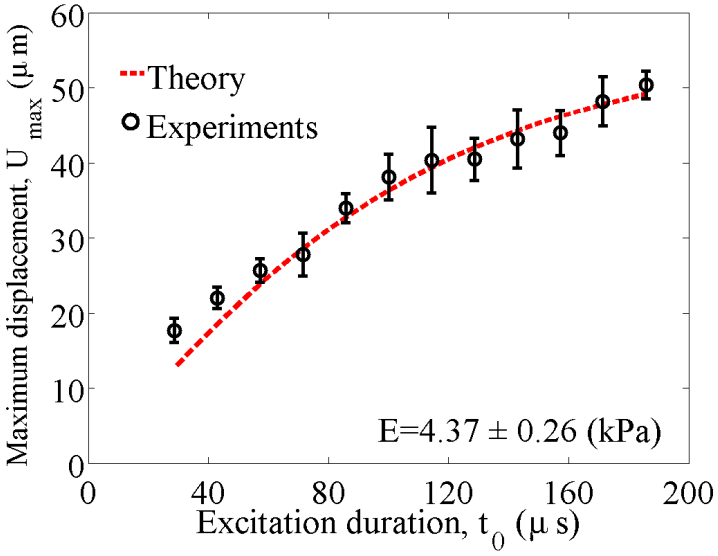

(a)

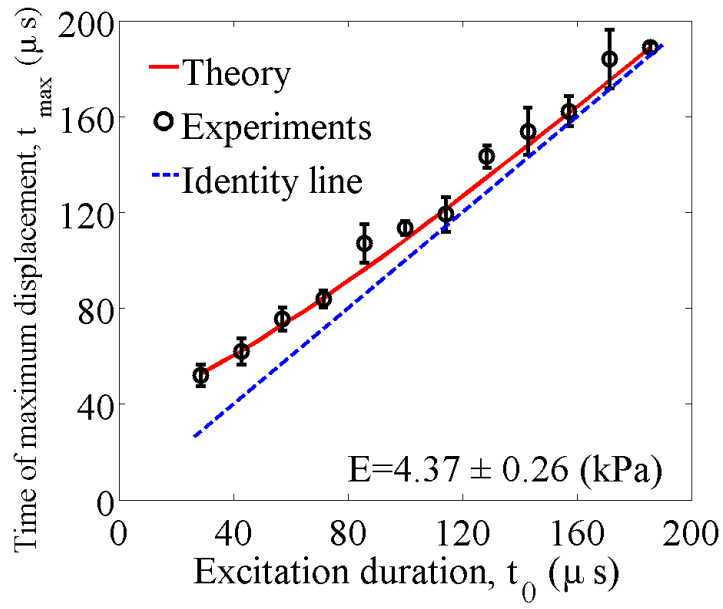

(b)

Figure 3.4: Comparison of theoretically predicted and experimentally measured (a) maximum displacement (U_{max}) vs. duration of acoustic pulse (t_0) and (b) time needed to reach maximum displacement (t_{max}) vs. duration of acoustic pulse (t_0). Four measurements were done using four different laser-induced microbubbles for every t_0. Error bars mean one standard deviation.

Calculated and measured displacements of the microbubble in response to the applied radiation force are in good agreement. The displacement profile and maximum displacement of a microbubble (U_{max}) depend on acoustic radiation pulse duration (t_0) (Fig 3.3). Increase of U_{max} does not have linear relationship with t_0. Increase of U_{max} gradually slows down as t_0 reaches values that induce steady-state displacement. Reaching steady-state displacement under certain t_0 means that elasticity of a medium is hard enough to push a microbubble in response to the bubble's motion and a microbubble does not have enough inertia to overcome the reaction of the medium after the applied external force is removed. Arrows in Fig. 3.3a indicate the end of acoustic pulses. When matching theory and experimental measurements, the scaling factor of acoustic radiation force (F_0) used here is 45 mN.

The comparison of theoretical and experimental dependences of maximum displacement (U_{max}) and time of maximum displacement (t_{max}) on acoustic radiation pulse durations (t_0) is shown in Fig. 3.4a and Fig. 3.4b, respectively. The scaling factor of acoustic radiation force (F_0) was 35 mN in the same phantom and this value comes from the best fit between the displacement profiles obtained from theoretical model and experimental measurements. The mean and standard deviation of radii of the four microbubbles are 75 and 2 μm. Theory and experiments have reasonable agreement. Fig. 3.4a depicts that the maximum displacement of the microbubble increases as radiation pulse duration becomes longer. Fig. 3.4b shows that at the end of a short pulse (under 120 μs) the bubble continues to move away from the excitation transducer until it reaches a maximum displacement ($t_{max} > t_0$) while at the end of a long pulse the bubble starts to

move back almost immediately ($t_{max} \approx t_0$) as shown by the identity line. Note that the same data was used for analysis of U_{max} and t_{max} in Fig. 3.4a and Fig. 3.4b. Four measurements were done (one measurement on four different laser-induced microbubbles in different locations within the same gelatin phantom) for every t_0.

The dependences of maximum displacement (U_{max}) and time of maximum displacement (t_{max}) on microbubble radius (R) for the duration of acoustic radiation pulse (t_0) of 43 μs are shown in Fig. 3.5a and Fig. 3.5b, respectively. Fig. 3.5a indicates that a large microbubble moves larger distances and takes a longer time to reach its maximum displacement as shown in Fig. 3.5b. Indeed, the surface area of a larger microbubble is bigger than that of a smaller microbubble. Because the diameter of the focus of the 3.5 MHz transducer is about 800 μm, microbubbles in the experiments are always inside the focal area. Thus, under the same acoustic radiation pressure, a larger microbubble experiences larger acoustic radiation force. The measured values of bubble radii are 49±3, 60±1, 66±3, 74±3, 85±3, 92±3, 98±2, and 110±3 μm and the corresponding scaling factor of acoustic radiation forces (F_0) of each microbubble are 30, 46, 54, 68, 90, 106, 120, and 151 mN after displacements of theoretical model and measurements were matched. The measurements were performed at least on three different microbubbles in the same gelatin phantom but at different locations.

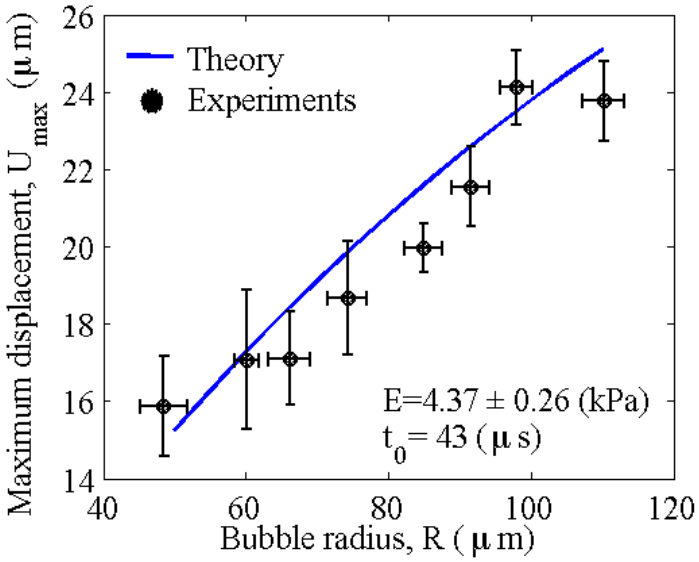

(a)

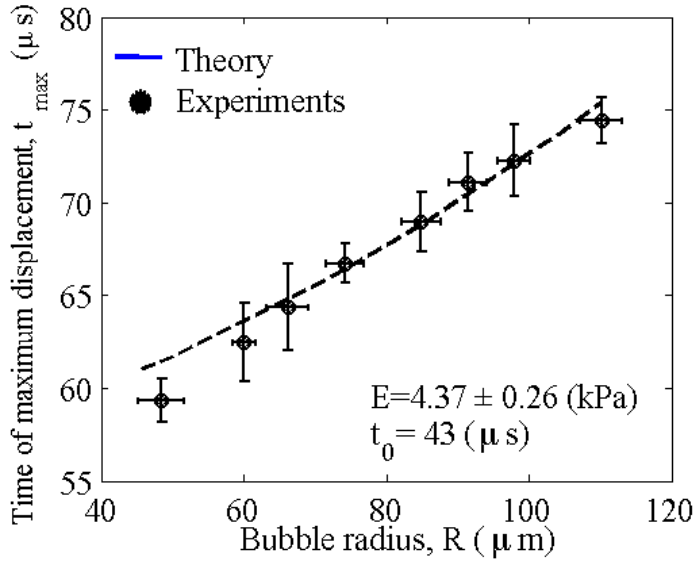

(b)

Figure 3.5: Comparison of theoretical and experimental dependences of (a) maximum displacement (U_{max}) and (b) time of maximum displacement (t_{max}) on bubble radius (R). In each point, three to five different measurements were made. Error bars mean one standard deviation.

The difference between time of maximum displacement (t_{max}) and acoustic radiation pulse duration (t_0) increased for short t_0 as shown in Fig. 3.4b and large microbubble radius (R) as shown in Fig. 3.5b. The large difference between t_{max} and t_0 was due to the increased inertial effect of the surrounding tissue. Furthermore, if the difference was large, more accurate measurements of t_{max} were possible, otherwise t_{max} could be hardly distinguished from t_0.

I could select durations of acoustic radiation pulse (t_0) based on microbubble radius (R) to perform effective Young's modulus reconstruction. To maximize the difference between time of maximum displacement and t_0, a short t_0 was used to reconstruct the elastic properties of the medium.

3.3.2 Reconstruction

The results of previous subsection A demonstrate that the developed theoretical model can predict mechanical response of microbubble under radiation force in a viscoelastic medium. In this subsection, an inverse problem is considered, i.e. reconstruction of the elastic properties of a medium.

Different strategies could be used to reconstruct elasticity. For example, an approach based on the value of maximum displacement was considered in several studies [96, 99]. The disadvantage of this method is the challenge in estimation of the acoustic energy delivered to the bubble as has been discussed previously. However, elasticity may be evaluated from the temporal characteristics of the bubble motion. While the amplitude of a laser-induced microbubble displacement is proportional to the amplitude of acoustic

radiation force, the time of maximum displacement (t_{max}) remains the same as shown in Fig. 3.6.

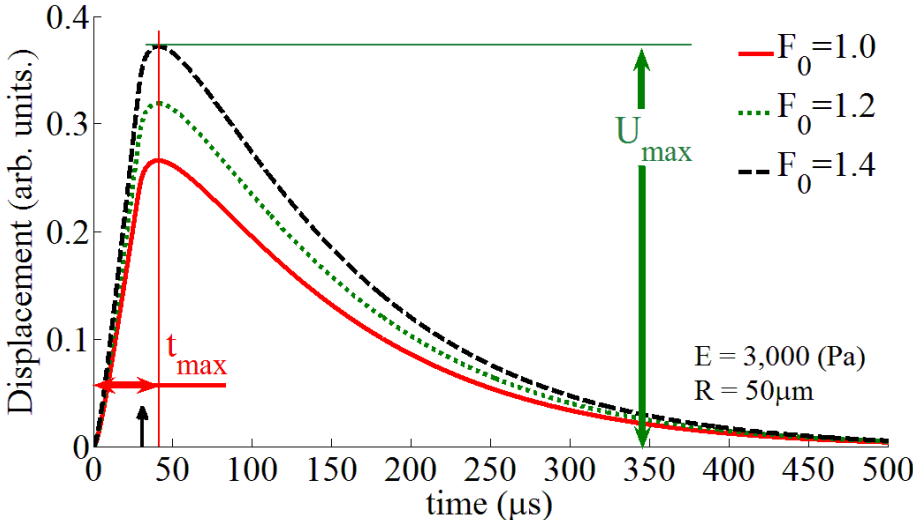

Figure 3.6: Theoretical analysis. Maximum displacement (U_{max}) and time of maximum displacement (t_{max}) under different acoustic radiation force amplitudes (F_0). t_{max} is an invariant parameter under different acoustic radiation forces. Acoustic radiation pulse duration (t_0) for this evaluation is 28 μs and arrow indicates the end of t_0.

Gelatin-based phantoms with the gelatin concentrations of 1.4, 2.0, 3.0, 4.0, 5.0, 6.0, 7.0% by weight were used to vary elastic properties of the phantoms at the reconstruction process [124]. To estimate elasticity of a medium, a microbubble was created in a phantom using a single laser pulse. Then, the microbubble was perturbed by an impulsive radiation force. I chose durations of acoustic radiation pulse as short as possible to maximize the inertial effect. In addition, experimentally meaningful durations were used to induce a noticeable displacement. The values of a laser-induced microbubble radius (R) and acoustic radiation pulse durations (t_0) were from 50±2 to142

± 5 μm and 43 μs, respectively. The measurements were performed twice for five different microbubbles created at various locations in every phantom.

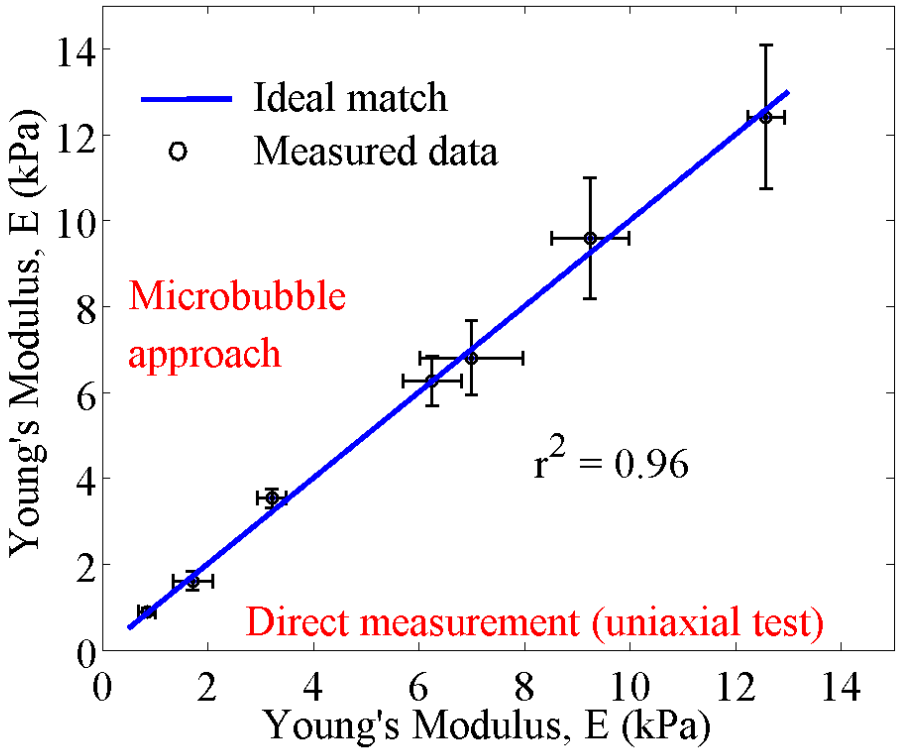

Figure 3.7: Comparison of Young's modulus values reconstructed using microbubble-based method and measured using the uniaxial load-displacement test. Two measurements were performed on five different microbubbles in all phantoms. Error bars represent one standard deviation.

Fig. 3.7 demonstrates the comparison of Young's modulus (E) reconstructed using the laser-induced microbubble approach and measured by using uniaxial tester. The solid line represents the ideal match between measurements. The Young's modulus reconstructed by the laser-induced microbubble technique and that directly measured by uniaxial test agree well with one another. For stiffer materials, the uniaxial tests provide higher accuracy of elasticity measurements. This is the result of a small difference

between time of maximum displacement (t_{max}) and duration of acoustic radiation pulse (t_0) for stiffer materials. Thus, the errors of t_{max} measurements induced larger error in the Young's modulus reconstruction. To measure elastic properties of stiff materials, higher pulse repetition frequency (PRF) of the ultrasound measurements is required. The increase of PRF is one of the major directions of our future work.

3.4 CONCLUSION

Assessment of the mechanical properties of a viscoelastic medium using laser-induced microbubbles under acoustic radiation force was developed. The measured displacements of microbubbles demonstrated good agreement with the theoretical predictions. Moreover, the phantom studies demonstrated good agreement between the Young's modulus reconstructed using remote microbubble-based measurements and that measured using the uniaxial tests. Thus, the Young's modulus of a medium can be measured using a laser-induced microbubble with typical sizes of tens of micrometers up to a hundred micrometers using acoustic radiation force.

Chapter 4: *High PRF ultrasound system and its validation with ex vivo bovine crystalline lens*

ABSTRACT

A high pulse repetition frequency ultrasound system for *ex vivo* measurement of mechanical properties of animal crystalline lens was developed and validated. I measured dynamics of laser-induced microbubbles created at different positions within the lens using nanosecond laser pulses. An impulsive acoustic radiation force was applied to the microbubble, and spatio-temporal measurements of the microbubble's displacement were accurately assessed using a custom-made high pulse repetition frequency ultrasound system consisting of two 25 MHz focused ultrasound transducers. The transducers were used to emit a train of ultrasound pulses and to receive the ultrasound echoes reflected from the microbubble. The developed system was operating at 1 MHz pulse repetition frequency. Based on measured dynamics of the microbubble, the Young's moduli of surrounding tissue were reconstructed and the values were compared with those measured using indentation test. Measured values of Young's moduli of 4 bovine lenses ranged from 2.6±0.1 to 26±1.4 kPa and there was good agreement between the two methods. Thus, the developed approach, utilizing the high pulse repetition frequency ultrasound system, can be used to assess the mechanical properties of *ex vivo* crystalline lenses. The potential of this approach for *in vivo* measurements is discussed.

4.1 INTRODUCTION

Detailed measurements of mechanical properties of the crystalline lens precede comprehensive understandings of the mechanism of accommodation and the development of age-related loss of accommodation power, the condition referred to as presbyopia. Since the theory of accommodation was developed [10], many explanations of the accommodative mechanism have been suggested [11, 125-128]. Despite intensive

research related to explaining the accommodative mechanism, uncertainty and debates among investigators continues. However, it is commonly agreed upon that the changes in viscoelastic properties of the lens play a major role in the development of presbyopia [21, 33, 40, 129]. The measurement of the mechanical properties of the crystalline lens *in vivo* could significantly help in understanding the accommodative mechanism of the human eye and in developing with new approaches for the presbyopia treatment.

Numerous experimental approaches have been developed to assess the mechanical properties of lenses: ultrasonic characterization of the lens using ultrasound wave attenuation [28]; compression tests [37, 116]; application of radical force [31, 32, 38]; hydrostatic or automated guillotine tests [35, 36]; uniaxial test [34]; cone penetration test [33]; and dynamic mechanical analysis [40, 117, 118]. However, there are several shortcomings in those measurement techniques. Most of them provide averaged mechanical properties of the whole lens. Even though they provide local elasticity within lenses, fragmented lenses, used in dynamic mechanical analysis technique, induce changes in mechanical properties during handling and preparation of the experiments. Moreover, these limitations restrict measurement techniques to be used only for *in vitro* studies

To overcome these disadvantages, microbubble-based acoustic radiation force was introduced as a technique to remotely measure the localized viscoelastic properties of the lens by combining microbubbles created by laser-induced optical breakdown and acoustic radiation force [27, 96-98]. This approach could potentially be extended to *in vivo* studies.

In the previous work of our group, researchers validated the theoretical model [104] related to the dynamics of rounded objects such as solid spheres [102, 122]. I validated the theory using laser-induced microbubbles [100] under acoustic radiation

force in viscoelastic medium such as gelatin phantoms. The mechanical properties of gelatin phantoms were estimated from the temporal characteristics of rounded objects and were found to be in good agreement with direct measurements [100, 102, 122]. It was found that impulsive acoustic radiation force should be used to fully utilize the inertia effect of laser-induced microbubbles after the termination of acoustic radiation force. In turn, high pulse repetition frequency (PRF) is required to sample the behavior of the laser-induced microbubbles under impulsive acoustic radiation force.

In this Chapter, I present and verify our high PRF ultrasound system to measure the mechanical properties of *ex vivo* animal crystalline lens. I measured Young's moduli of four different bovine lenses at different locations within lenses. Measured values of Young's moduli were ranged from 2.6±0.1 to 26.0±1.4 kPa. The obtained values were compared with the results of indentation tests, and a good agreement between the methods was demonstrated.

4.2 MATERIALS AND METHODS

To verify the theoretical model and a high pulse repetition frequency (PRF) ultrasound system in *ex vivo* animal crystalline lens, the experiments were performed using a laser-induced microbubble interrogated by impulsive acoustic radiation force. The validation procedure consisted of two consecutive experiments: 1) microbubble-based measurements with a high PRF ultrasound system and 2) indentation tests for reference measurements with the bench-top uniaxial tester In-Spec 2200 (Instron, Inc., Morwood, MA). The same animal lenses were used for both steps. The laser-induced microbubble experiments were followed by the indentation test in series. Young's modulus of *ex vivo* animal lenses was reconstructed based on the microbubble experiments and compared with the results of the indentation test. Thus, the indentation

tests served as reference measurements to verify the theoretical model and the performance of the high PRF ultrasound system.

During the experiments, four testing procedures were carried out: performance of high PRF system was investigated, accuracy of indentation test was explored, boundary effects on the indentation test results were examined, and time effects on the changes of the mechanical properties of *ex vivo* animal crystalline lens were identified.

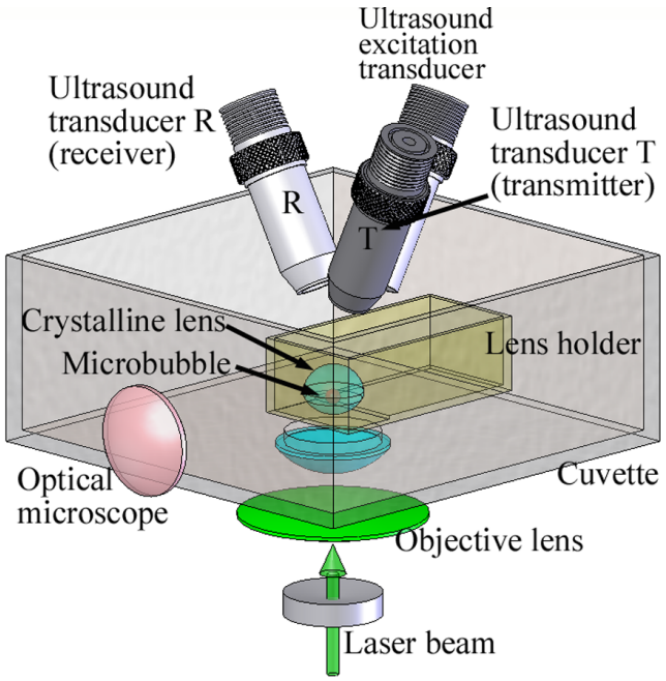

Figure 4.1: A schematic view of the experimental setup. A crystalline lens with anterior surface facing down was positioned in the lens holder, and a microbubble was produced by a focused laser beam inside a lens. A 3.7 MHz excitation transducer was used to generate acoustic radiation force applied to a microbubble. The motion of a microbubble was tracked by two 25 MHz ultrasound transducers (T and R) – separation of transmit (T) and receive (R) transducers allowed for high (up to 1 MHz) pulse repetition frequency. In addition to ultrasound measurements, the size of the microbubble was also observed using an optical microscope.

I designed and built (Fig. 4.1) an experimental system for the microbubble-based acoustic radiation force experiments. A Nd:YAG laser pulse (Polaris II, Fremont, CA) with 5 ns pulse duration, 532 nm wavelength, and 10 mJ energy was focused by a custom-built objective lens (1.13 numerical aperture (NA) and 8.0 mm working distance) to produce a microbubble inside the crystalline lens. A high NA was used to control the size and shape of the microbubbles [109]. The size of the microbubbles was also observed using an optical microscope (Dino-Lite AM411T, Wirtz, VA) operating at 230x magnification.

A cuvette with a hole for laser beam delivery was fixed to the standing post and it was filled with the phosphate buffered saline (Sigma-Aldrich, Inc., St Louis, MO) to minimize the changes of the mechanical properties of the lens during the experiments. A crystalline lens with anterior surface facing down was positioned in the lens holder, and the lens holder, attached to 3D translation stages, was placed inside the cuvette. A microbubble was produced by a focused laser beam inside the lens. The lens holder was moved during the experiments to generate microbubbles at different locations in the crystalline lens. A 3.7 MHz transducer (F/#=2 and bandwidth=17%, Valpey Fisher, Hopkinton, MA) and two 25 MHz transducers (F/#=4 and bandwidth=51%, Olympus-NDT, Waltham, MA) with focal lengths of 25.4 mm were located at the top of the cuvette. The angle between two 25 MHz transducers was 35°. The angle between the 3.7 MHz transducer and the plane made by two 25 MHz transducers was also 35°. The foci of three transducers were aligned at the location of the microbubble.

The 3.7 MHz excitation transducer, connected to RF power amplifier (ENI model 2100L, ENI, Rochester, NY) with 50 dB gain, was used to generate impulsive acoustic radiation force and to displace a laser-induced microbubble. The duration of the acoustic radiation pulse was varied from 10 to 30 μs.

The experimental setup was similar to the setup described in [100]. The main difference between the previous setup and the current setup was an additional ultrasound transducer was added to achieve high pulse repetition frequency for the accurate measurements of the microbubble dynamics. Thus, the motion of the microbubble was tracked by two 25 MHz ultrasound transducers (T and R). By separating ultrasound transducers T (transmit) and R (receive), I could achieve high pulse repetition frequency, up to 1 MHz.

Reconstruction of Young's moduli of phantoms and animal crystalline lenses using microbubble approach were performed by finding the best fit between displacement profiles measured by the microbubble experiments and calculated by theory [100]. Once the experimentally measured time required for a microbubble to reach its maximum displacement (t_{max}) was matched to the theoretically calculated t_{max}, the value of the scaling factor of acoustic radiation force was chosen to match experimentally observed displacements with theoretically calculated displacements. The shear viscosity was evaluated by comparing decaying profiles of microbubble displacements from theory and experiments.

4.2.1 High PRF system and signal processing

The schematic diagram of the high PRF ultrasound system is shown in Fig. 4.2. The system consisted of two function generators (Agilent 33250A, Agilent, Loveland, CO), radiofrequency (RF) power amplifier (E&I model A150, E&I, Rochester, NY) with 55 dB gain, two 25 MHz ultrasound transducers, an ultrasound receiver (DPR 300 Pulser / Reciever, JSR Ultrasonics, Pittsford, NY), and the analog-to-digital dual channels data acquisition card (A/D card, CompuScope 12400, GaGe Inc., Montreal, Canada). The function generator A was used to control the PRF of pulse-echo probing and to trigger the

function generator B that controlled the center frequency of each sine pulse. The sine pulses, generated by the combination of function generators A and B with desired PRF and center frequency, were saved at the channel 2 of the A/D card for data analysis and, at the same time, directed to the RF power amplifier. The center frequency and PRF of the train of sine pulses were 25 MHz and 1 MHz, respectively. The amplified pulses were directed to the ultrasound transducer T (transmitter). Emitted ultrasound pulses were reflected at the surface of the microbubble and the ultrasound transducer R (receiver) received the train of echoes. This train of echoes was amplified by the ultrasound receiver with a 45 dB gain and stored at the channel 1 of the A/D card for offline data analysis. Therefore, RF raw data were comprised of trains of sine pulses, saved at channel 2, and backscattered ultrasound echoes, saved at channel 1. The acoustic radiation pulse was launched from the 3.7 MHz ultrasound excitation transducer with delay of 60 μs according to the first sine pulse to displace the laser-induced microbubble. The duration of the acoustic radiation pulse was varied from 10 to 30 μs. Arrival time of the first echo with respect to the first sine pulse defined the initial location of the microbubble. Changes in the arrival times of the following echoes were used to determine the microbubble displacement using a cross-correlation speckle tracking method [121]. The kernel size and search window for cross-correlation tracking were 94 μm and 188 μm, respectively. Before the cross-correlation speckle tracking algorithm was applied to the saved RF raw data, a comb filter was used to remove the cross-talk between the ultrasound transducer R and the excitation transducer.

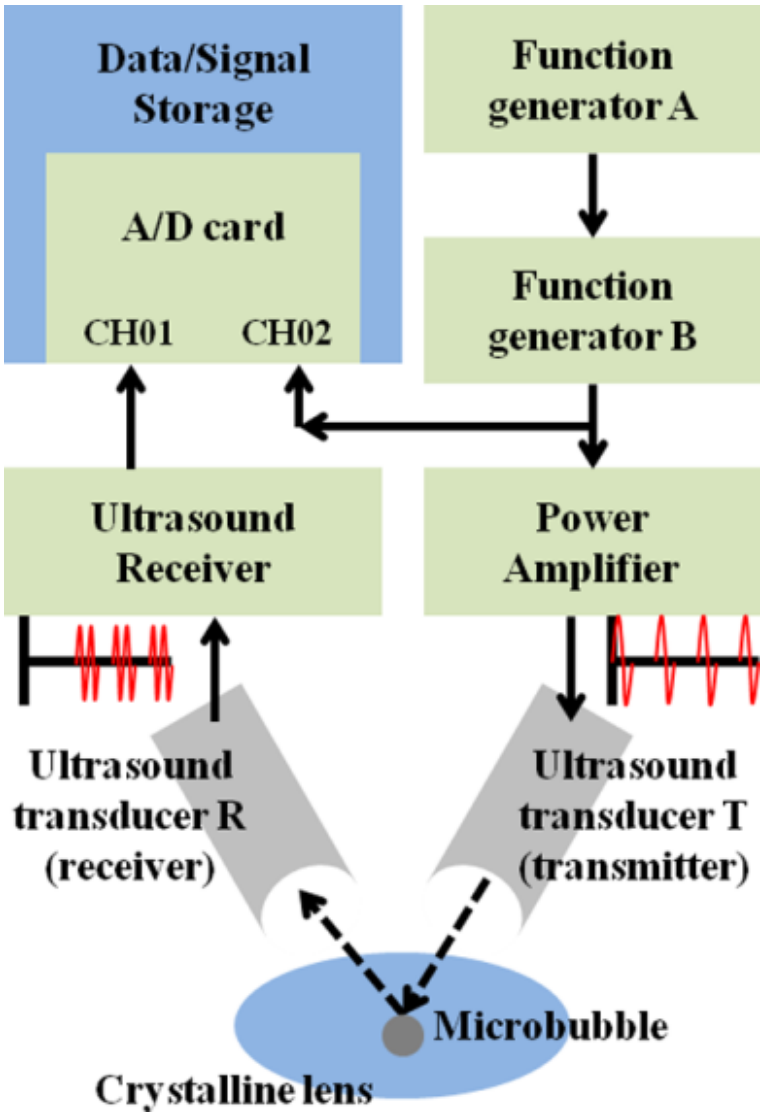

Figure 4.2: The schematic diagram of the high PRF ultrasound system. Dotted arrows indicated the direction of transmitted and reflected trains of sine pulses at the surface of microbubble.

4.2.2 Lens preparation

Four bovine eyes, from 25 – 30 months old cows, were obtained from the Sierra for Medical Science, Inc. (Whittier, CA). They were shipped over night in the thermo-insulated box with ice packs. All the experiments were done within 12 hours after eyes arrived at our facility.

For the laser-induced microbubble experiments, the cornea was removed from an eye. Then, the sclera was dissected vertically so that vitreous humor, lens, and components attached to both vitreous and lens could be pulled out from the sclera. Lens was carefully taken out by separating it from the vitreous. With an unused scalpel, the lens capsule was removed by slightly tearing off a small zone of the lens equator. Once the lens material without lens capsule was obtained, it was placed in a lens holder (Fig. 4.1) and 5 ml of 6% gelatin solution was added for fixation. The anterior of the animal lens was facing the bottom of the lens holder. During the laser-induced microbubble experiments, the lens and the lens holder was in the phosphate buffered saline to minimize changes in the mechanical properties of lens.

After the laser-induced microbubble experiments, the lens was carefully removed from the lens holder and sectioned equatorially for indentation test. Firstly, a 14 mm internal diameter trephine (Katena eye instruments, Denville, NJ) was placed inside the animal lens by the guidance of the existing laser-induced microbubbles (Fig. 4.3(a)). Secondly, a razor blade was used to make a flat surface for the indentation test. The lens fragment, inside the trephine with an open surface on top of the trephine (Fig 4.3(b)), was put inside phosphate buffered saline for the indentation test. The thickness of the lens fragment was 6 mm. Laser-induced microbubbles were always created 6 mm away from the anterior of the lens.

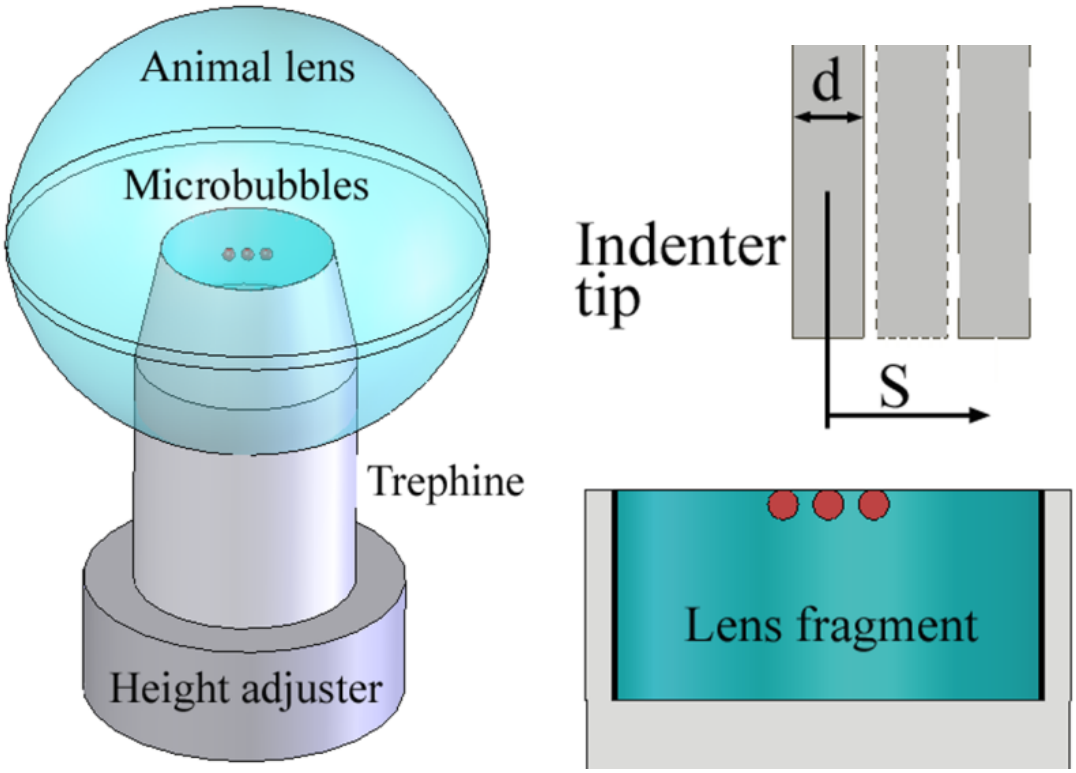

(a) (b)

Figure 4.3: Preparation of lens fragment for the indentation tests after laser-induced microbubble experiments. (a) The trephine with a 14 mm internal diameter and the height adjuster were placed into the lens by the guidance of existing microbubbles. Lens fragment was made by cutting the lens equatorially with a razor blade. (b) Cross-sectional view of lens fragment bounded by the height adjuster (bottom) and the trephine (sides). The indenter for indentation tests was placed above the lens fragment. The indenter was used to measure Young's modulus of lens fragment at different locations. The diameter of indenter tip (d) was 2.38 mm and the location from the center (S=0) is S.

4.2.3 Validations of the experimental systems

Before the high PRF ultrasound system and the indentation system were used to measure Young's modulus of animal crystalline lenses, the following experiments were performed.

4.2.3.1 High PRF ultrasound system validation with phantoms

To validate the high PRF ultrasound system, the experiments were performed using laser-induced microbubbles in tissue-mimicking phantoms, containing 2.0, 3.0, 6.0, 9.0, and 11.0% by weight gelatin (300 Bloom, type-A, Sigma-Aldrich, Inc., St. Louis, MO). For the microbubble experiments, one measurement was performed on five different microbubbles for each gelatin sample. In addition, cylindrical samples of 35 mm diameter and 17 mm height were made out of the same gelatin solution to be used in direct mechanical measurements with uniaxial tester by pressing the whole phantom with 45 mm diameter plates. Prior to measurements, the phantoms and samples were kept together and followed the same experimental protocol to minimize any differences between the materials. The duration of acoustic pulse was 10 μs for all phantom experiments. Young's modulus found using the laser-induced microbubble approach was compared with Young's modulus measured using uniaxial tester.

4.2.3.2 Accuracy of the intendation system and boundary effects

The indentation system consisted of an indenter (tip diameter = 2.38 mm), lever system, and a uniaxial tester, In-Spec 2200. The indenter was connected to the load cell of the uniaxial tester by a lever system with the force gain of 7.5.

To measure localized Young's modulus of a sample, an indenter with small tip diameter was used. However, for soft materials, the reaction force in the indentation tests was under the measurable ranges of the load cell. To increase the reaction force over the measurable ranges of the load cell, the lever system was used. If the reaction force from soft materials to the indenter tip was 10 mN, the lever magnified the force at the load cell to 75 mN. Therefore, the lever bridged the indenter and the load cell of the uniaxial tester to detect the small reaction force effectively. The indenter experienced acceleration and deceleration before the tip of the indenter moved up to about 2 mm from the starting

point. Therefore, the fragmented animal crystalline lens, inside the trephine, was placed at least 2 mm away from the tip of the indenter.

To verify the accuracy of the indentation system and investigate the influence of the boundary effects on the measurements of Young's modulus near the wall of the trephine, I used gelatin phantoms with the concentrations of 1.5, 2.0, 2.5, 3.0, 6.0, 9.0, and 11.0 % by weight. Typical uniaxial test measurements with 45 mm diameter plates were done by pressing the whole gelatin samples with 35 mm diameter and 17 mm thickness. For indentation tests, I made a container that mimicked the geometry of a lens fragment inside the trephine. The container had 14 mm diameter and 6 mm depth. The containers were filled with gelatin solutions with different concentrations as mentioned above. Indentation measurements were performed at six points on gelatin samples inside the container. Six points were 0, 2.0, 2.5, 3.0, 3.5, and 4.0 mm away from the center of gelatin container (Fig. 4.3(b)). The tip of the indenter was moved with the speed of 0.11mm/s in vertical direction and the total indention was 1.5 mm after the indenter tip touched the gelatin surface. Young's modulus was estimated in the assumption of the frictionless boundary condition at the indenter tip and the fixed bottom boundary using equations obtained by Yang [130].

To test the accuracy of the indentation measurement system, I compared Young's modulus of each gelatin sample measured by uniaxial test with Young's modulus measured by the indentation test at the center of the gelatin samples in the container. To explore the boundary effects I compared Young's modulus obtained in six different locations for each gelatin sample.

After the system for indentation experiments was tested, the same system was used for reference measurements. The fragment of animal lens was prepared using the

trephine and the razor blade (Fig. 4.3(a)) and placed in the phosphate buffered saline (PBS) for indentation tests.

4.2.3.3 Time effects of bovine lens in PBS

To identify the time effects on the changes of Young's modulus of bovine lens, I measured Young's modulus of the fragmented bovine lens prepared by the same procedure explained at lens preparation (Fig. 4.3(a)). I measured Young's modulus of the bovine lens in 4 different times with 2 hour intervals (from 0 to 6 hours) and in 5 different locations with 2.5 mm gap.

4.3 RESULTS

4.3.1 Validation of high PRF ultrasound system using phantom

Reconstruction of Young's modulus of viscoelastic medium using the custom-built high PRF ultrasound system is presented. Figs. 4.4(a) and (b) present an example of the dependence of microbubble displacement on time for 2% and 11% gelatin phantoms and the displacements of microbubbles in Fig. 4.4(b) are averaged from five measurements. Fig. 4.4(a) shows that how averaged displacements from five measurements are obtained. All five displacement profiles are plotted in one axis. For the theoretical calculations of the displacements of microbubbles shown in Fig. 4.4(c), Young's moduli obtained from the best fit between experimental measurements and theory were used [100]. Times required to reach microbubble's maximum displacement (t_{max}) are indicated at Fig. 4.4. and t_{max} was used forreconstruction of Young's modulus of the medium [100]. Fig. 4.4 shows how the amplitude of displacements and the time of maximum displacement (t_{max}) decrease with elasticity increase. t_{max} was found by the quadratic approximation of measurement points.

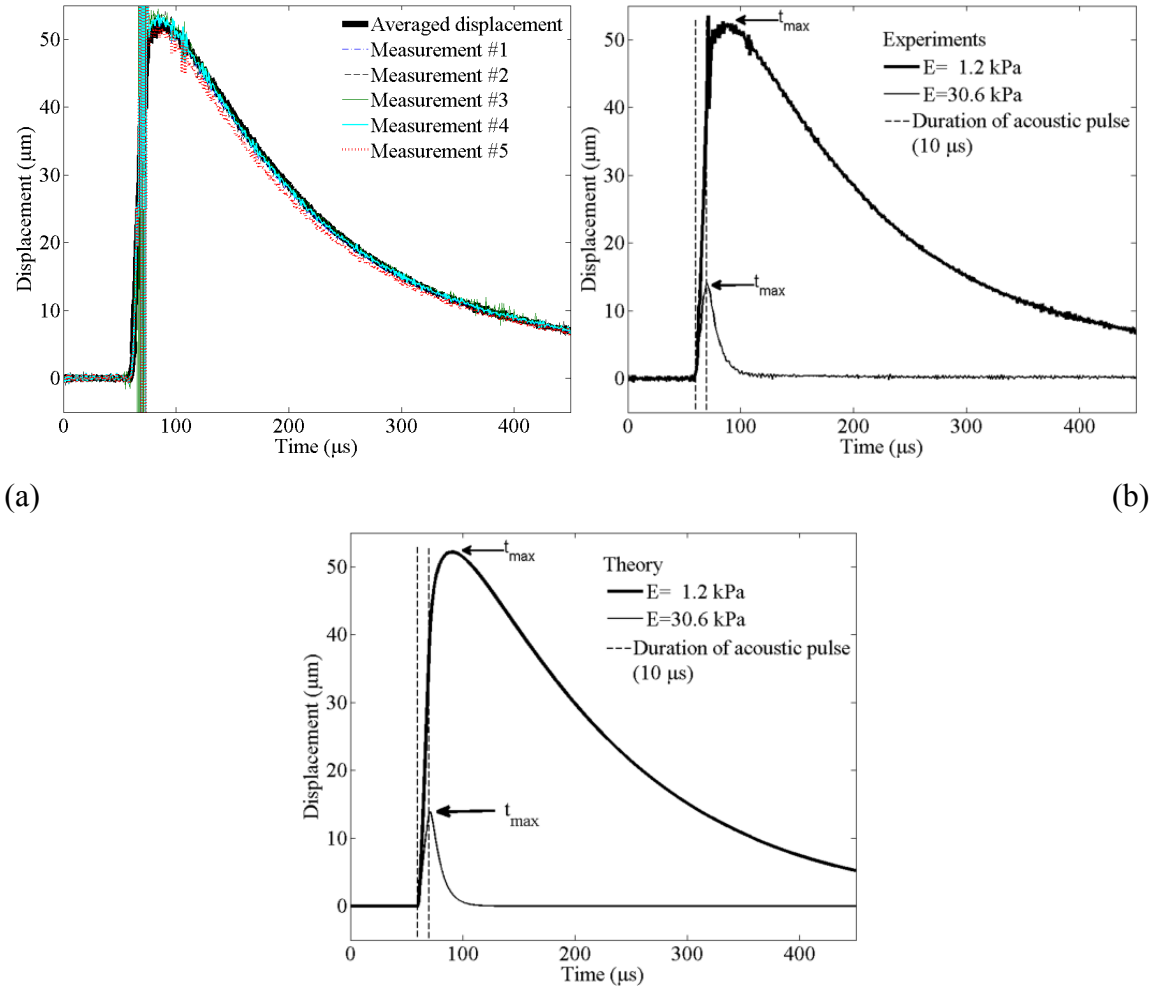

Figure 4.4: (a) Experimentally measured displacements from five different microbubbles and their averaged displacement for the thick line in (b). (b) Experimentally measured and averaged displacement from five different microbubbles and (c) theoretically calculated displacements of the microbubbles in response to 10 μs acoustic pulse in gelatin phantoms of different elasticity. Average values of Young's moduli (E) for plots (b) and (c) are 1.2 kPa (thick line) and 30.6 kPa (thin line). One measurement was performed to five different microbubbles for each gelatin phantom. Time of maxiumum displacement of microbubble is indicated as t_{max}. The dotted vertical lines indicate start and end of acoustic radiation force. For thick solid lines, the radius of the microbubble is 25±2 μm and for thin solid lines, the radius of the microbubble is 20±2 μm. In theoretical calculations shear viscosity of 0.05 Pa·s is used.

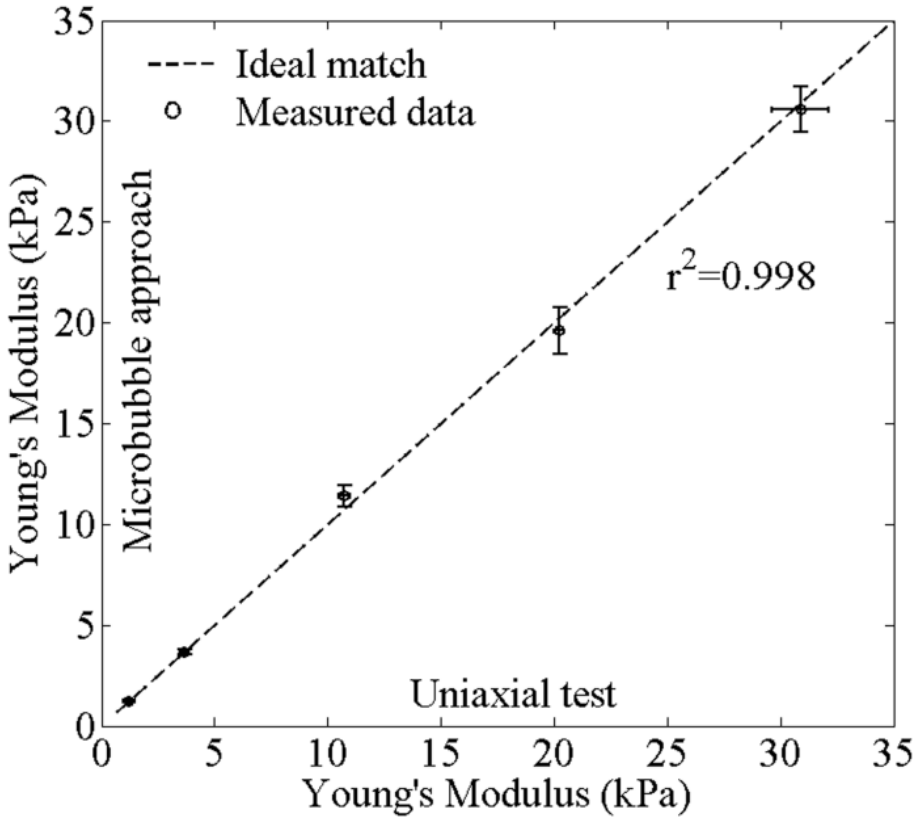

Figure 4.5: Comparison of Young's modulus values reconstructed using microbubble approach with the high PRF ultrasound system and measured using the uniaxial load-displacement test. One measurement was performed to five different microbubbles at each case. Error bars are plus/minus one standard deviation.

Fig. 4.5 shows the comparison between Young's moduli obtained using the microbubble approach and the uniaxial test. Error bars in Fig. 4.5. were generated from one measurement of five different microbubbles in each gelatin sample. Measurements of Young's modulus of gelatin phantoms using microbubble approach are in reasonable ranges when comparing to results obtained from the uniaxial test. I can also estimate the shear viscosity of gelatin phantoms by comparing the decaying profiles of the dynamics of a laser-induced microbubble from experiments and theory. The estimated shear viscosity for this phantom study is 0.05 Pa· s which is used in all theoretical calculations.

The value corresponds to the results of our previous work. [100, 102, 122]. In the measured range, Young's modulus is almost independent from the shear viscosity. The results show that the high PRF ultrasound system has the ability to assess the Young's modulus of tissue-mimicking phantoms with high accuracy.

4.3.2 Validation of indentation test system

In this section I am comparing Young's modulus of gelatin samples measured by uniaxial test with Young's modulus measured by indentation test at the center of gelatin samples in the container (Fig. 4.6(a)). Mean and standard deviation values betIen indentation test and uniaxial test have good agreement. Thus, indentation measurement system can be used to measure local Young's modulus of *ex vivo* animal crystalline lens.

Because the lens fragment inside the trephine is bounded by trephine (Fig. 4.3), the boundary effects should be investigated. To explore the boundary effects, I compared Young's modulus of six different locations (Fig. 4.3(b)) in each gelatin sample measured with indentation measurement system. The results are shown at Fig. 4.6(b).

The measured values of Young's modulus increase close to the boundary because of rigid boundary condition. However, for our study, to avoid the boundary effects, I measured Young's modulus of animal crystalline lenses near the central region. This way, I could dodge the boundary effects.

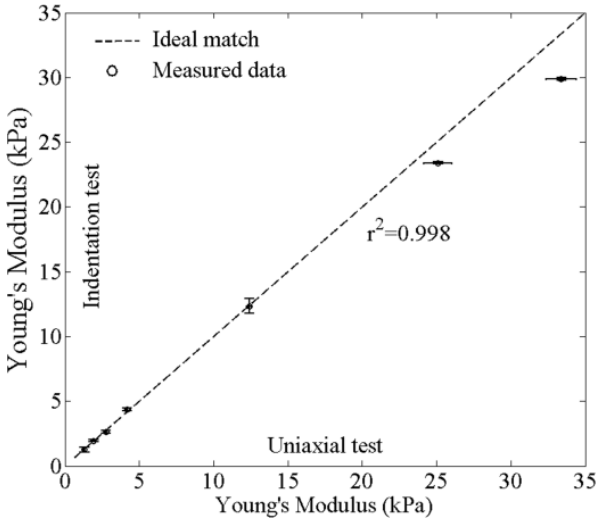

(a)

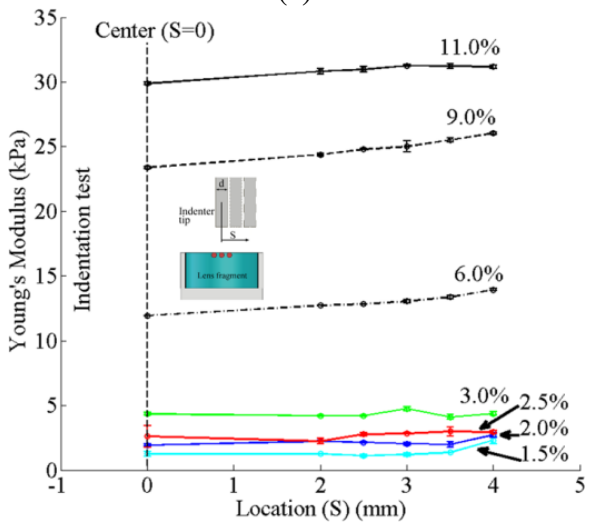

(b)

Figure 4.6: Validation of indentation measurement system. (a) Accuracy test of the indentation test by comparing Young's modulus obtained by the indentation measurement system with Young's modulus measured by the uniaxial test. (b) Dependence of the Young's modulus on the distance from phantom center for different gelatin concentrations.

4.3.3 Reconstruction of Young's modulus of bovine lenses

Before the reconstruction of Young's modulus was performed, the last validation was done on a bovine lens from 25-30 months old cow. Because for both the laser-

induced microbubble and indentation experiments, lens and fragmented lens were immersed in phosphate buffered saline (PBS), I investigated the changes of the mechanical properties of a bovine lens in PBS from zero to six hours with two hours intervals and measured Young's modulus of a bovine lens at five locations (S= $\pm n \cdot d$, d=2.5 mm, n=0, 1, 2, Fig. 4.3(b)). The fragment of bovine lens was prepared with the trephine (Fig. 4.3(a)) and put in PBS to investigate the time effects. As shown in Fig. 4.7, elastic properties of bovine lens do not change significantly in PBS up to 6 hours. Moreover, the experiments for both the laser-induced microbubble and the indentation experiments took less than one and a half hours after the lens was removed from an eye globe. Thus, during the series of experiments, time effects on the changes of the mechanical properties of bovine lenses can be ignored.

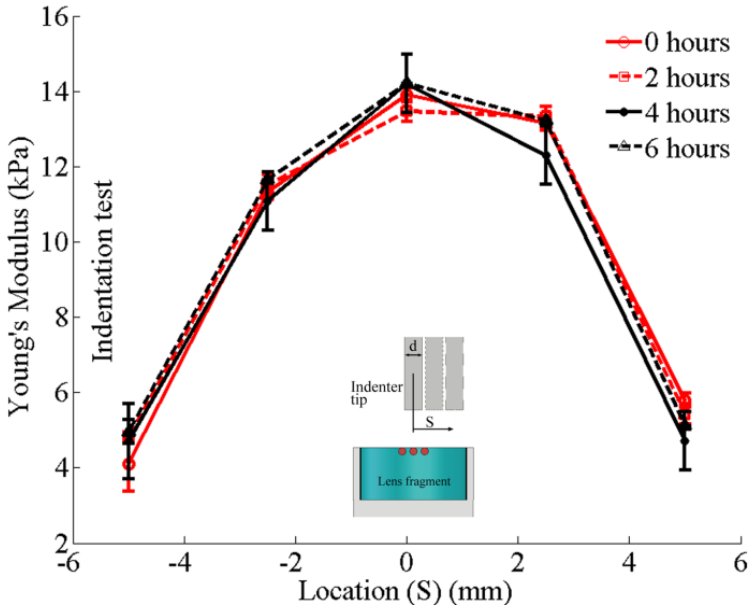

Figure 4.7: Time effects on the changes of the mechanical properties of bovine lens measured with indentation test system. Indentation measurements started from 0 to 6 hours after lens extraction with 2 hours intervals. S is the distance from the center of lens fragment (S=0 indicates the center point, Fig. 4.3(b)).

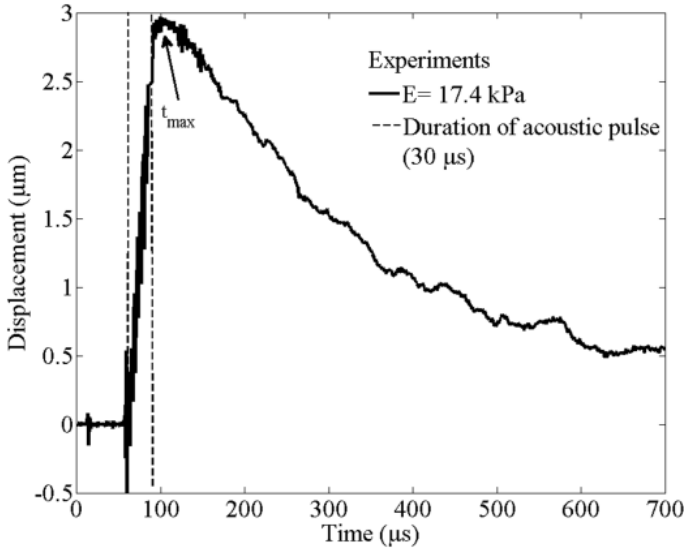

(a)

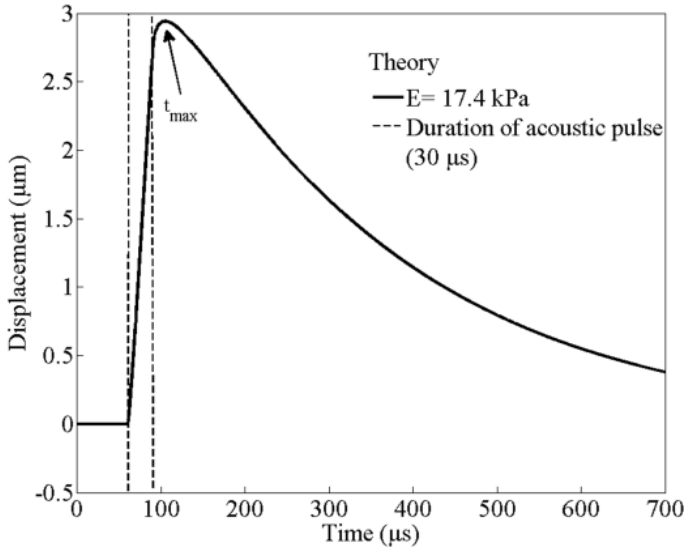

(b)

Figure 4.8: (a) Experimentally measured and averaged displacement from three trials to one microbubble and (b) theoretically calculated displacement of the microbubble in response to 30 μs acoustic pulse. Average value of Young's modulus (E) for plots (a) and (b) is 17.4 kPa and the shear viscosity is 1.5 Pa · s. Time of maxiumum displacement of microbubble is indicated as t_{max}. The dotted vertical lines indicate start and end of acoustic radiation force. The radius of the microbubble is 63±3 μm. Two plots (a) and (b) correspond to the circle at Fig. 4.9.

The results of the validation of the high PRF ultrasound system and the results presented in [100] demonstrate that the developed theoretical model can predict the dynamics of laser-induced microbubbles under acoustic radiation force in a viscoelastic medium with high PRF ultrasound system. Reconstruction, the inverse problem of Young's modulus of bovine lens was then considered. Three measurements were performed to each microbubble at the specific location within lenses. Experimentally obtained and theoretically calculated displacements of a laser-induced microbubble with the radius of 63±3 μm are shown in Figs. 4.8(a) and 4.8(b), respectively. Experimentally obtained displacement of each microbubble (Fig. 4.8(a)) is presented as an averaged value from three trials. The microbubble dynamics presented at Figs. 4.8(a) and 4.8(b) corresponds to the circle in Fig. 4.9. The duration of acoustic pulse was 30 μs. The Young's modulus of the bovine lens at the specific location was 17.4±0.5 kPa. I can also estimate the shear viscosity of bovine lenses by comparing the decaying profiles of the displacement of a laser-induced microbubble from experiments and theory. The estimated shear viscosity for this case is 1.5 Pa· s (Fig 4.8).

Fig. 4.9. describes the comparison of Young's modulus (E) reconstructed using the laser-induced microbubble approach and measured by indentation test. The dotted line indicates the ideal match between two measurements. A total of 11 microbubbles were generated in four bovine lenses; the first lens had three microbubbles; the second lens had three microbubbles; the third lens had one microbubble; and the fourth lens had four microbubbles. Table 4.1 shows Young's moduli of 11 different points in four bovine lenses measured by microbubble approach and indentation test. The measured Young's moduli varies from 2.6±0.1 to 26.0±1.4 kPa. The Young's modulus reconstructed by the laser-induced microbubble technique and that directly measured by indentation test agree well with each other as shown in Fig. 4.9. The corresponding shear viscosities of four

bovine lenses are 1.5±0.1, 1.6±0.1, 1.3, and 1.5±0.1 Pa· s by considering the decaying profiles of the dynamics of a laser-induced microbubble from theory and experiments. The shear viscosity does not change much within the area of measurements at the same bovine lens. In summary, the proposed approach using the laser-induced microbubble interrogated by impulsive acoustic radiation force with the high PRF ultrasound-based imaging system can be used to estimate the mechanical properties of *ex vivo* crystalline lens.

Bovine lens no	Young's Modulus (kPa)	
	Microbubble approach	Indentation test
Sample 1	6.6±0.05	6.3±0.3
	13.4±0.1	15.5±0.3
	17.4±0.5	18.5±0.6
Sample 2	13.8±0.1	13.8±0.5
	16.4±0.1	16.9±0.4
	23.6±1.6	26.3±0.9
Sample 3	4.3±0.1	4.3±0.4
Sample 4	2.6±0.1	2.6±0.3
	7.2±0.1	7.3±0.2
	11.1±0.6	10.8±0.6
	26.0±1.4	26.9±0.6

Table 4.1: Comparison of Young's moduli of bovine lenses using 11 different microbubbles.

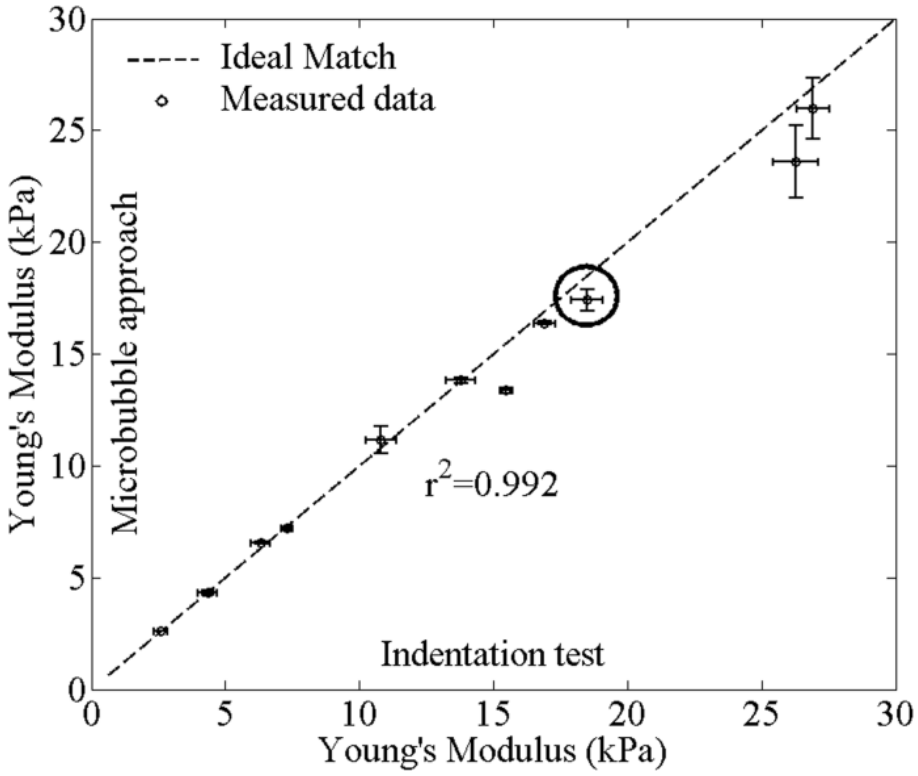

Figure 4.9: Comparison of Young's modulus values reconstructed using microbubble-based approach and measured using the indentation test. 11 laser-induced microbubbles created at 4 different bovine lenses were used. Three measurements were performed to each microbubble. Detailed example of the dynamics of the laser-induced microbubble at the circle is presented at Fig. 4.8. Error bars are plus/minus one standard deviation.

4.4 DISCUSSION

In this Chapter, I validated our theoretical model and the high PRF ultrasound system. To make a full use of the inertia effect of a laser-induced microbubble motion after the termination of acoustic radiation force, I chose very short acoustic radiation force pulses. I used 10 μs pulses and 30 μs pulses for phantoms and bovine lenses, respectively. In general, as previously reported [100], the difference between the duration of acoustic pulse (t_0) and time to reach the maximum displacement of a microbubble (t_{max}) becomes larger when t_0 decreases. However, the difference between t_0

and t_{max} is still short time. At most cases, the difference (t_{max}- t_0) is less than 30 μs. As a consequence, a high PRF ultrasound system to measure the dynamics of a microbubble is definitely needed to find t_{max} accurately. I built the high PRF ultrasound system that had 1 MHz PRF and testified it in both phantom and animal crystalline lens experiments.

Using laser-induced microbubble approach Young's modulus of soft tissues such as crystalline lenses can be measured with reasonable accuracy and precision compared to the indentation test. In general, the shear viscosity of tissue also can be evaluated based on the measured motion of the microbubble. The estimations of the shear viscosity changed from lens to lens, but did not change much within one lens. One possible explanation is that the measurement area is too small to observe big changes in shear viscosity (usually within 3 mm). The second explanation is that, microbubble approach is not sensitive enough to measure small changes in shear viscosity. Currently, no standard measurement technique is available to measure lens viscosity. Therefore, I have focused on measuring Young's modulus of crystalline lens.

Indentation measurement system was built and validated. There are several possible sources of the discrepancy between two measurement techniques. The 2.38 mm diameter indenter is still large compared to the diameter of laser-induced microbubble (80~150 μm). Measurements by indentation test were an averaged value of a circular area, but measurements by the microbubble approach had very localized values. Secondly, locations where the measurements were performed in laser-induced microbubble approach and the indentation test could not match perfectly. Even though indentation measurements were guided by existing laser-induced microbubbles created at the previous experiments, misalignment between the laser-induced microbubbles and the tip of the indenter may have caused errors in the measurements of Young's modulus of bovine lenses. Lastly, the equation used to calculate the value of Young's modulus [130]

assumes that the medium is infinite. However, due to the shape of the trephine, the lens fragment was bounded by 14 mm diameter of cylindrical walls. Thus, there is a boundary effect that makes the elasticity stiffer. The solution I took to avoid the boundary effects was that I measured the mechanical properties of lens near the center (Fig. 4.6(b)). However, boundary may still play a role in stiffening the measured Young's modulus even at the center.

As shown in Fig. 4.7, the lens from a 25-30 months old cow had Young's modulus gradient within 10 mm diameter (total diameter of the lens was about 16 mm). Central part, 6 mm below the anterior of the lens (thickness of the lens was about 11 mm), was almost 3 times stiffer than outer region, 5 mm away from the center. There are discrepancies between bovine and human lenses from morphological and biochemical point of view, but the result shows the location-dependent changes of the mechanical properties within eye lens [40, 41].

For the improvement of the estimation of elastic properties of soft tissues, I can modify our theoretical model. The current theoretical model assumes that the surrounding medium of a microbubble is isotropic and homogeneous [100]. However, lens is a layered object by adding new cells on top of old cells, making it an anisotropic and non-homogeneous medium. This discrepancy between assumptions and the real object may increase the differences when measuring Young's modulus of lens. Thus, future work is to create a model which includes these factors.

Ex vivo measurements of elastic properties of eye lens are important by itself when defining the mechanism of accommodation because reliable measurement data for mechanical properties of eye lenses is limited. However, more importantly, *in vivo* measurements should be performed to acquire more reliable data. Our approach has potential to be extended to *in vivo* experiments. The measurement procedure could be

combined with laser-based surgical procedures in the lens such as femtosecond lentotomy [2, 3]. In turn, the clinical treatment plans of ocular tissue related diseases such as presbyopia can be gained.

4.5 CONCLUSIONS

The high PRF ultrasound system to measure the mechanical properties of animal crystalline lens using microbubble-based method was developed and validated. Reconstructed Young's moduli in different locations for four bovine lenses correlated well with those measured by indentation test. Thus, the proposed laser-induced microbubble approach with the high PRF ultrasound system can be used to measure the mechanical properties of *ex vivo* animal crystalline lenses.

Chapter 5: *The mechanical properties of ex vivo animal crystalline lens: age-related changes and location-dependent variations*

ABSTRACT

The mechanical properties of *ex vivo* animal lenses from three groups – an old bovine (25-30 months old, n=4), a young bovine (6 months old, n=4), and a young porcine (6 months old, n=4) – were evaluated using a laser-induced microbubble approach. I measured the dynamics of laser-induced microbubbles created at different locations within the crystalline lenses. An impulsive acoustic radiation force was applied to the microbubble. The microbubble displacements were measured using a custom high pulse repetition frequency ultrasound system that can sample the motion of the microbubble every 1 μs. Based on the measured dynamics of the microbubbles, the Young's moduli of the animal lenses were reconstructed. Age-related changes and location-dependent variations in the Young's modulus of lenses were observed. Near the center, the old bovine lenses had approximately 5 times higher Young's modulus compared to the Young's modulus of young bovine and porcine lenses. The gradient of Young's modulus with respect to radial distance was clearly observed in the lenses from all three groups. However, there were no clear boundaries or rapid changes in tissue elasticity between the inner nucleus and outer cortex.

5.1 INTRODUCTION

When a near object is in focus, the lens becomes thicker and rounder in configuration [12, 131, 132]. This process is called "the lens accommodation." As age advances, accommodation power degrades [13, 19, 133-137]. Debates related to how the eye changes its focus (accommodation) and why the age-related degeneration of the focusing ability happens (presbyopia) have continued because the accommodative

mechanism has not been fully understood [10, 11, 125-128, 138]. There are indications that lens stiffening can be responsible for the inability of the lens to change its shape and loss of accommodation. To understand the processes leading to accommodation and presbyopia, a comprehensive understanding of the viscoelastic properties of the lens is required. A dearth of trustworthy measurements of mechanical properties has proved problematic in the development of the theory of accommodation [21, 38].

A crystalline lens is a non-homogeneous structure that is comprised of different zones. The cortex surrounds the nucleus and the nucleus has several zones that are created in different developmental stages [5, 22, 27, 40, 41, 139]. Researchers reported that the stiffness variation with respect to equatorial distance and age were observed using dynamic mechanical analysis [40, 41]. They concluded that the stiffness of the nucleus had an order of magnitude larger value than that of the cortex for human lenses over the age of 50. Regarding the age differences, they presented an almost 1,000 times increase in stiffness between nucleus regions of lenses from ages 14 to 78 [40]. However, lens fragmentation, used in the dynamic mechanical analysis technique, could induce changes in mechanical properties of lens due to the disruption of the internal crystalline structure during handling and preparation of the lens for the experiments.

As a promising way of assessing the mechanical properties of crystalline lens, microbubble-based acoustic radiation force technique was introduced [27, 97, 140, 141]. In this approach, an acoustic radiation force is applied to a microbubble, induced by a laser pulse. The displacement of microbubble is measured by ultrasound in pulse-echo mode and used to evaluate the local elasticity of the lens. This approach had an advantage because the internal structures of the lens remain intact compared to fragmentation. By combining laser-induced microbubbles and acoustic radiation force, the localized viscoelastic properties of lenses can be measured remotely.

In our previous work, I validated our theoretical model [104] using solid spheres [102, 122] and laser-induced microbubbles [100] in tissue-mimicking gelatin phantoms. The mechanical properties of gelatin phantoms were estimated from the temporal characteristics of rounded objects and were found to be in good agreement with direct measurements [100, 102, 122]. To improve the performance of microbubble-approach, I designed and built a high pulse repetition frequency ultrasound system. The validation of the system was successfully done in *ex vivo* bovine crystalline lenses [142].

In this Chapter, I investigate age-related changes and location-dependent variations of the mechanical properties of animal crystalline lenses. I generated laser-induced microbubbles at various locations in a crystalline lens by focusing a single nanosecond laser pulse. Then, the dynamic behavior of the laser-induced microbubble, displaced by an impulsive acoustic radiation force, was measured using a custom-built high pulse repetition frequency ultrasound system. I reconstructed the localized Young's modulus using measured dynamics of the laser-induced microbubble by comparing them with the theoretically calculated values. I compared the viscoelastic properties of both young and old bovine lenses to explore age-related changes. In addition, location-dependent variations of mechanical properties were measured using bovine and young porcine lenses.

5.2 Materials and Methods

5.2.1 Lens preparation

All tissue samples were obtained from the Sierra for Medical Science, Inc. (Whittier, CA). The eye globes were shipped over night in the thermo-insulated box with ice packs. Three groups of animal eyes were used: old bovine (25-30 month old), young bovine (6 month old), and young porcine (6 month old). In each group, four crystalline

lenses (n=4, samples 1-4), excised from the eye globes, were used in the experiments. All the experiments were performed within 12 hours after the tissue samples arrived at our facility.

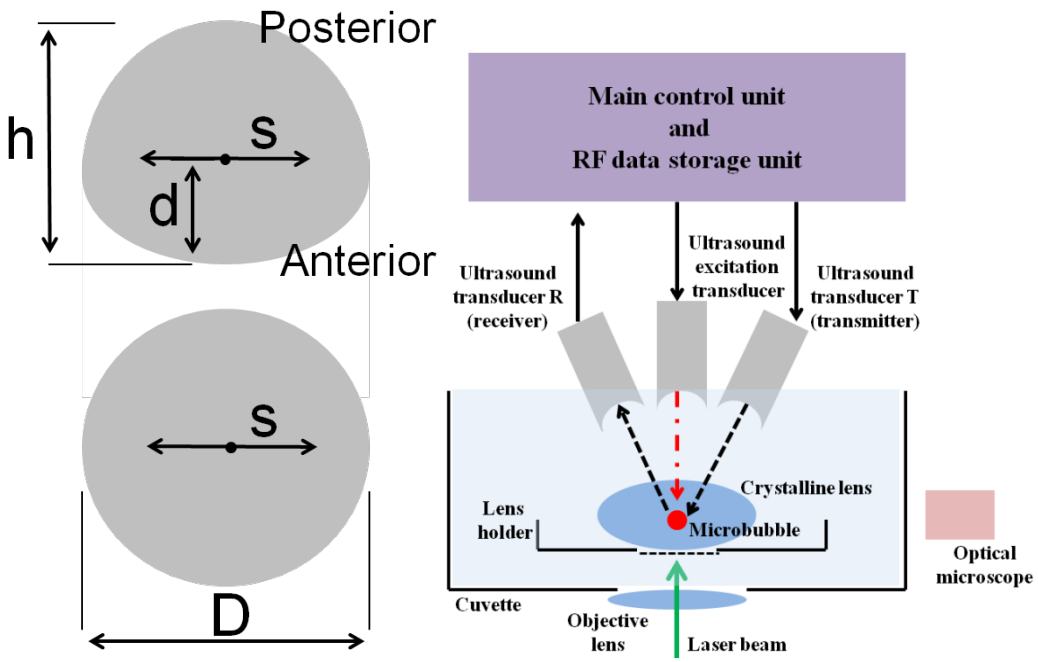

(a) (b)

Figure 5.1: (a) Coordinate system defined within the lens. This coordinate system is referenced throughout the entire chapter. The top and bottom diagrams show a sagittal section and an equatorial section of the lens. Laser-induced microbubbles were created along the S-axis and the center location (solid dot) corresponds to S=0. (b) A schematic view of the experimental setup. A crystalline lens with anterior surface facing down was positioned in the lens holder, and a microbubble was produced by a laser beam focused inside a lens. Excitation transducer (3.7 MHz) was used to produce acoustic radiation force pulse and initiate microbubble displacement (dash-dot arrow). The motion of a microbubble was tracked by two 25 MHz ultrasound transducers (T and R) – the separation of transmit (T) and receive (R) transducers allowed us to achieve high pulse repetition frequency (up to 1 MHz). The train of pulses from ultrasound transducer T and echoes reflected on the surface of a microbubble to ultrasound transducer R are shown as dashed arrows. The size of the microbubble was monitored by an optical microscope.

The lens was carefully extracted from an eye globe and the lens capsule was removed by making small tears at the lens equator. The lens was placed and secured in a lens holder filled with 5 ml of 6 wt % gelatin solution. The anterior of the animal lens was facing the bottom of the lens holder. During the experiments, the lens and the lens holder was kept in the phosphate buffered saline (Sigma-Aldrich, Inc., St Louis, MO) to minimize changes in the mechanical properties of lens.

Fig. 5.1(a) presents a coordinate system defined within the lens. Lenses from old bovine, young bovine, and young porcine had diameters (D in Fig. 5.1(a)) of 16±0.5 mm, 12±0.3 mm, and 10±0.5 mm, respectively. Total thicknesses (h in Fig. 5.1(a)) from the anterior to the posterior part were 11±0.6 mm, 9±0.3 mm, and 7±0.3 mm for old bovine, young bovine, and young porcine, respectively.

5.2.2 Laser-induced microbubble generation

Laser-induced microbubbles with typical radii of 45-60 micrometers were generated along the S-axis in Fig. 5.1(a). By adjusting the 3D axis, where the lens holder and the crystalline lens were attached, I controlled the distance between S-axis and anterior part (d in Fig. 5.1(a)) and the values of d were 4, 4, and 3 mm for old bovine, young bovine, and young porcine, respectively. The radial distances (S in Fig. 5.1(a)) were chosen as plus and minus multiples of one fortieth of one inch ($S=\pm 0.635 \cdot k$ mm, $k=1,2,4,6,8$). Thus, laser-induced microbubbles were generated along S-axis, d mm away from the anterior part of each crystalline lens, with the same spacing.

To produce a microbubble inside an animal crystalline lens, I used a pulsed Nd:YAG laser (Polaris II, Fremont, CA) with 5 ns pulse duration, 532 nm wavelength, and 10 mJ energy. A custom-built objective lens with high numerical aperture (1.13) and long working distance (8.0 mm) was designed to create spherical microbubbles located

inside the outer cortex and the inner nuclear of the lenses [109]. The size of the microbubble was monitored by an optical microscope (Dino-Lite AM411T, Wirtz, VA) operating at 230x magnification.

5.2.3 Experimental system and data processing

A crystalline lens was positioned in the lens holder. The holder was attached to 3D translation stages to generate laser-induced microbubbles by a focused laser beam in a lens at different locations along S-axis (Fig. 5.1(a)). An ultrasound excitation transducer (center frequency=3.7 MHz, F/#=2, and bandwidth=17%, Valpey Fisher, Hopkinton, MA) and ultrasound transducers T and R (center frequencies= 25 MHz, F#=4, and bandwidth=51 and 53 %, Olympus-NDT, Waltham, MA) with focal lengths of 25.4 mm were located at the top of the cuvette to push and track the microbubbles in a lens, respectively. By separating ultrasound transducers T (transmit) and R (receive), I could use desired high pulse repetition frequency (PRF) and set the PRF as 1 MHz [142]. The foci of three transducers were aligned at the location of the microbubble.

As shown in Fig. 5.1(b), the main control unit controlled the timing and sequences of pulse-echo probing using ultrasound transducers T and R and acoustic radiation pulse generation using the ultrasound excitation transducer [142]. The radiofrequency (RF) data storage unit, also controlled by the main control unit, saved the train of pulses from the main control unit and echoes acquired by the ultrasound transducer R for off-line data processing. Therefore, RF raw data was comprised of trains of pulses and backscattered ultrasound echoes. The generation of acoustic radiation pulse started with the delay of 60 μs after the first pulse was launched. The duration of acoustic radiation pulse was 20 μs.

Arrival time of the first echo defined the initial location of the microbubble and the changes in the arrival times of the following echoes determined the microbubble

displacement using a cross-correlation speckle tracking method [121]. The kernel size and search window for cross-correlation tracking were 65 ns and 130 ns, respectively. RF raw data was filtered with comb filter to remove the cross-talk between the ultrasound transducer R and the ultrasound excitation transducer before the cross-correlation speckle tracking algorithm was applied.

Reconstruction of the Young's moduli of animal crystalline lenses using microbubble approach were performed by finding the best fit between displacement profiles measured by the microbubble experiments and calculated by theory [100, 142]. Once time for microbubble to reach its maximum displacement (t_{max}) measured by microbubble experiments was matched to t_{max} calculated by theory, the value of the scaling factor of acoustic radiation force was chosen to match experimentally observed displacements with theoretically calculated displacements. The shear viscosity was found by comparing decaying profiles of microbubble displacements from theory and experiments.

5.3 RESULTS

The inverse problem, reconstruction of Young's modulus (E) of lenses from three groups, is now considered. Three measurements were taken of each microbubble at its specific location within the lens. Experimentally measured displacements of microbubbles (Fig. 5.2(a)) are presented as averaged values from three trials (averaged E=2.9 (thin line) and 23.3 (thick line) kPa) to microbubbles in samples 1 and 2. The measured radii of microbubbles are 47±2 (thin line) and 54±2 (thick line) μm. The displacements of laser-induced microbubbles, shown in Fig. 5.2(a), correspond to the dotted and the solid arrows in Fig. 5.3(a). Theoretically calculated microbubble displacements are shown in Fig. 5.2(b). Young's modulus and shear viscosity values for

the theoretical calculation were determined by the best fit between microbubble displacements obtained by theory and experiments. I can also estimate the shear viscosity of lenses by comparing the decaying profiles of the displacements of laser-induced microbubbles from experiments and theory. The estimated shear viscosities for these cases are 1.3 Pa·s. Fig 5.2 demonstrates the differences of the behavior of microbubbles in crystalline lenses with different elasticity. As it has been observed in phantom experiments, U_{max} and t_{max} in stiff region are smaller than those in soft region [100].

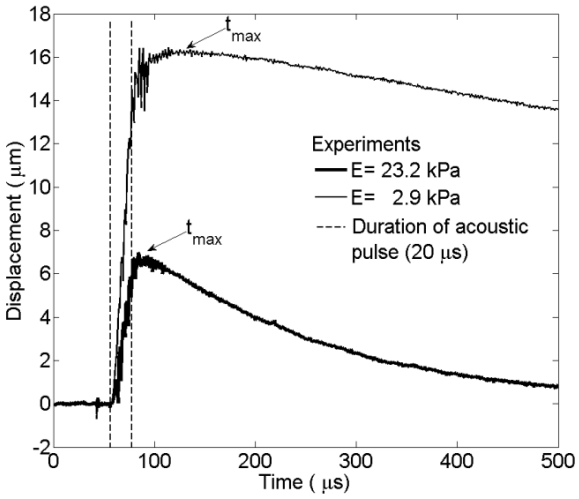

(a)

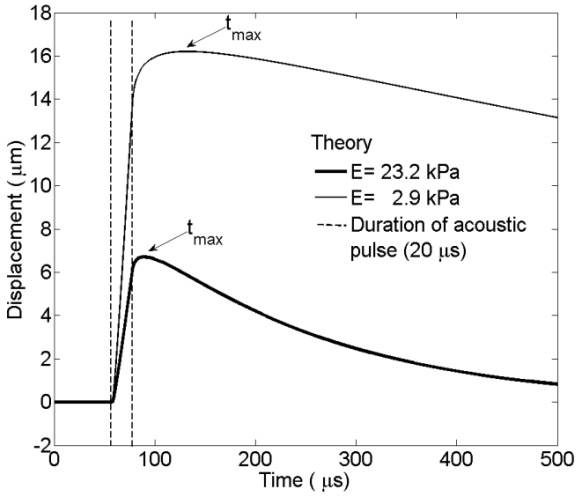

(b)

Figure 5.2: (a) Experimentally measured and averaged displacements from three measurement trials of microbubbles at two different locations in old bovine lenses and (b) theoretically calculated displacements of the microbubbles in response to 20 μs of the acoustic pulse (starting at 60 μs). Values of Young's modulus (E) are 2.9 kPa (thin line) and 23.2 kPa (thick line). Time of maximum displacement of microbubble is indicated as t_{max}. The dotted vertical lines indicate start and end of acoustic radiation force pulse. The radii of the microbubbles for thin and thick lines are 47$\pm$2 μm and 54$\pm$2 μm, respectively. In theoretical calculations, a shear viscosity of 1.3 Pa·s is used for both cases. The thick and thin lines in (a) correspond to the dotted arrow and the solid arrows in Fig. 5.3(a), respectively.

The location-dependent variations of Young's moduli of four lenses from old bovine, young bovine, and young porcine within ±5.1 mm along S-axis (Fig. 5.1(a)) are shown in Figs. 5.3(a)~(c), respectively. Three measurement trials were performed at each measurement point in each sample and error bars are plus/minus one standard deviation. Solid lines in (a), (b), and (c) are mean values over samples for each measurement point. For the comparison of Young's modulus between species and ages, solid lines from Figs. 5.3(a)~(c) are plotted in Fig. 5.3(d). The measured values of Young's moduli were ranged from 2.2±0.1 to 25.9±0.7 kPa for old bovine lenses within ±5.1 mm, 1.6±0.1 to 5.8±0.2 kPa for young bovine lenses within ±5.1 mm, and 1.2±0.1 to 5.7±0.2 kPa for young porcine lenses within ±3.8 mm. The results show age-related increase of elasticity in old bovine lenses. Near ±5.1 mm area, Young's modulus between old and young bovine lenses are comparable; however, as one approaches the center, Young's modulus of old bovine lenses jumps dramatically and the difference in Young's modulus between young and old reaches about 5 times (Fig. 5.3(d)). Moreover, even for young bovine and porcine lenses, the gradient of Young's modulus exists (Figs. 5.3(b) and 5.3(c)). I measured Young's moduli of all the designated radial distances along S-axis (Fig. 5.1(a)). For some points, measured displacements of microbubbles were not detectable because of the misalignment between the excitation transducer and microbubbles. Those points were left as blanks in Fig. 5.3.

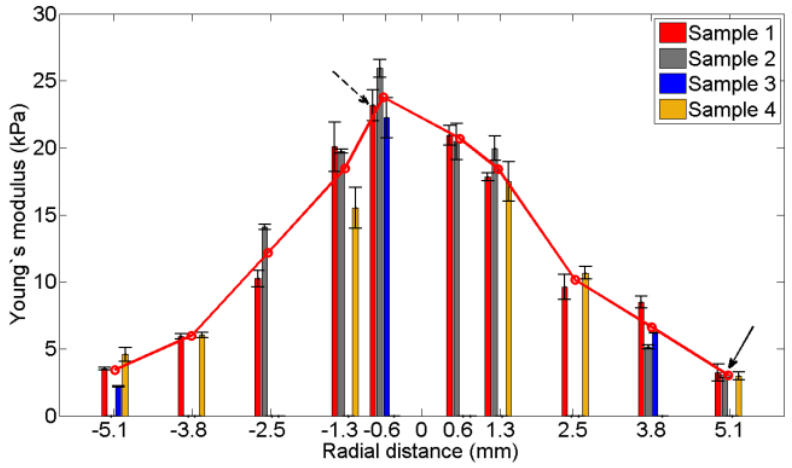

(a)

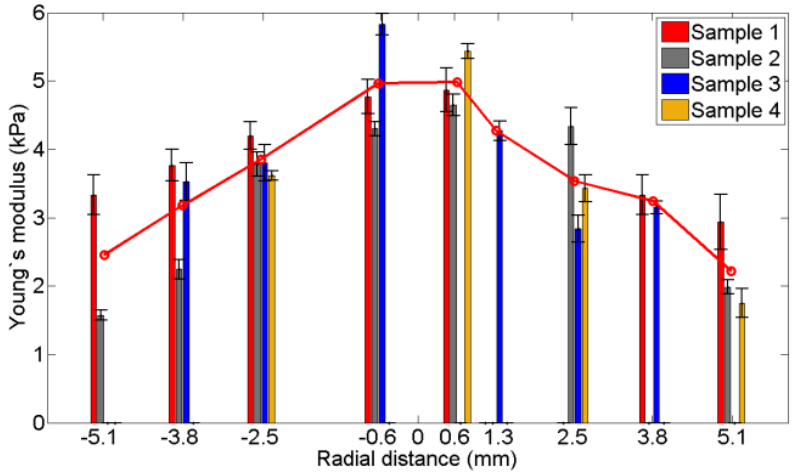

(b)

Figure 5.3: Young's modulus measurements of three groups: (a) old bovine (25-30 months old), (b) young bovine (6 months old), and (c) young porcine (6 months old). Radial distance is S-axis in Fig. 5.1(a). and 0 mm in the radial distance corresponds to the center of the lens. Four samples were used for each group. Solid lines in (a), (b), and (c) are mean values over samples for each measurement point. (d) Comparison of Young's modulus dependences with respect to radial distance for three groups. Measurement points in (d) are reproduced from plots (a), (b), and (c). Examples of detailed dynamics of the laser-induced microbubbles in old bovine lenses (dotted and solid arrows in (a)) are shown at Fig. 5.2(a). Three measurement trials were performed at each measurement point in each sample and error bars are plus/minus one standard deviation.

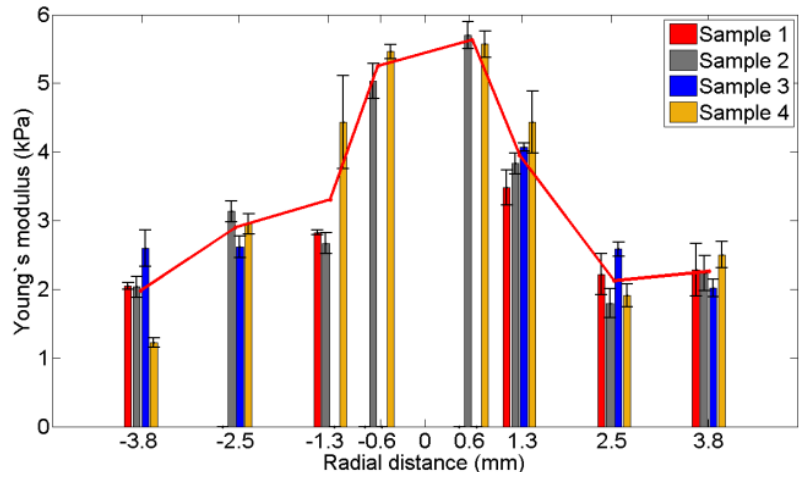

(c)

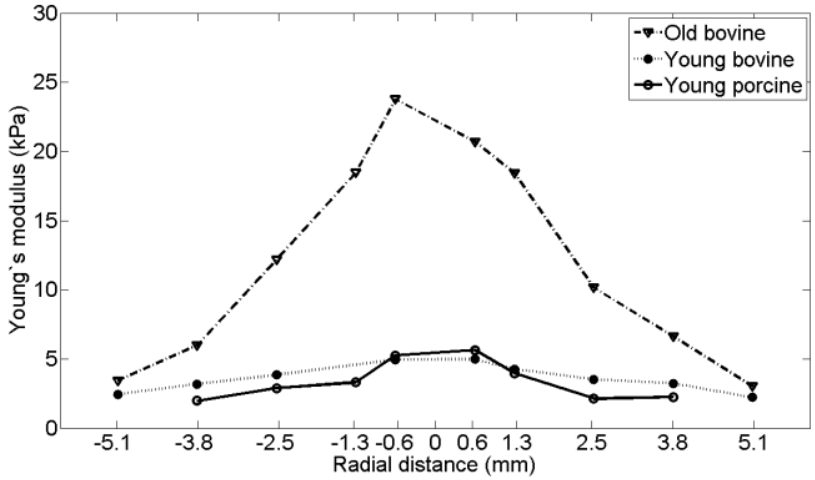

(d)

Figure 5.3: Young's modulus measurements of three groups: (a) old bovine (25-30 months old), (b) young bovine (6 months old), and (c) young porcine (6 months old). Radial distance is S-axis in Fig. 5.1(a). and 0 mm in the radial distance corresponds to the center of the lens. Four samples were used for each group. Solid lines in (a), (b), and (c) are mean values over samples for each measurement point. (d) Comparison of Young's modulus dependences with respect to radial distance for three groups. Measurement points in (d) are reproduced from plots (a), (b), and (c). Examples of detailed dynamics of the laser-induced microbubbles in old bovine lenses (dotted and solid arrows in (a)) are shown at Fig. 5.2(a). Three measurement trials were performed at each measurement point in each sample and error bars are plus/minus one standard deviation.

Shear viscosity was also evaluated with our microbubble approach. Mean and standard deviations of shear viscosity are shown for each lens sample (Fig. 5.4(a)) and all lens samples (Fig 5.4(b)). Generally, old bovine lenses had the highest shear viscosity (1.32±0.12 Pa·s) and young porcine lenses had the lowest values (0.87±0.08 Pa·s). Young bovine lenses had medium shear viscosity values (1.0±0.12 Pa·s). Shear viscosity values of lenses of three groups are independent with each other by the student's t-test results after comparing p-values of three combinations: old and young bovines, young porcine and bovine, and old bovine and young porcine ($p<0.01$ for all cases, Fig. 5.4(b)). Microbubble approach can differentiate shear viscosity values of lenses from different groups.

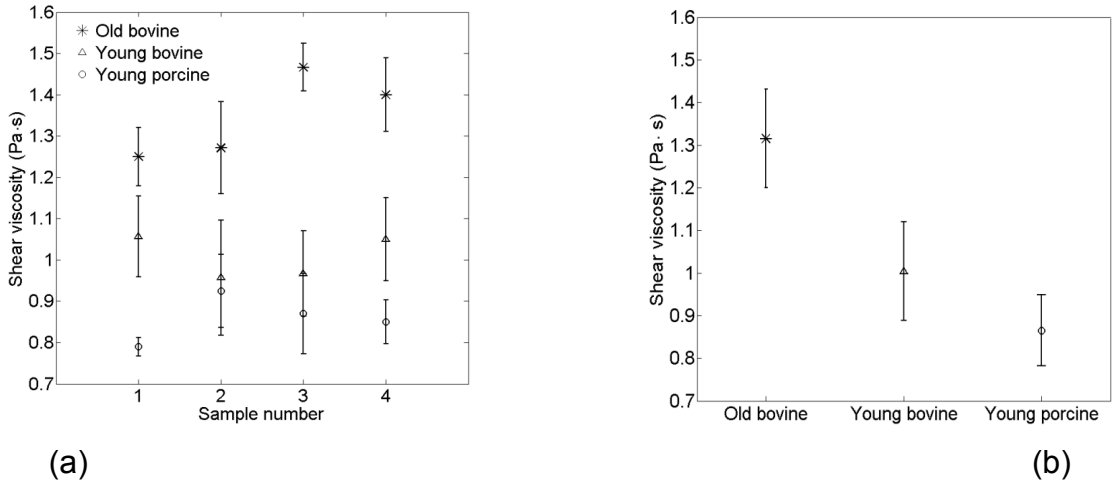

Figure 5.4: (a) Shear viscosity measurements of four lens samples from three groups. Horizontal axis represents the sample (lens) number and vertical axis is shear viscosity. (b) Averaged shear viscosity values of all lens samples from each group. Error bars are plus/minus one standard deviation. Obtained shear viscosities of lenses from three groups are compared by student's t-test and the differences of shear viscosity between three groups are statistically significant ($p<0.01$).

5.4 DISCUSSION

In this Chapter, the mechanical properties of *ex vivo* animal crystalline lenses were estimated using a laser-induced microbubble interrogated by impulsive acoustic radiation force. The approach was validated by comparing reconstructed Young's modulus of *ex vivo* bovine lenses with direct indentation measurement in our previous studies [142]. The mechanical properties of animal crystalline lenses were estimated for different ages of the same species and different species of the same ages to investigate age-related changes and location-dependent variations in the mechanical properties of lenses.

The laser-induced microbubble approach has two advantages when measuring the viscoelastic properties of crystalline lenses. First, this approach can assess the local mechanical properties within lenses. Microbubbles remotely generated by laser-induced optical breakdown are small and location specific. Usually, the diameter of laser-induced microbubbles is in the order of one hundred micrometers, which enables us to measure the viscoelastic properties of a small area in the crystalline lenses. Moreover, microbubbles can be created at any location within a crystalline lens thus allowing investigation of the gradient of the mechanical properties within a lens. Secondly, I do not need to dissect the lens for measurements. Once the inner structure is disturbed by the sectioning of lenses for the experiments, the natural mechanical properties could be subject to change. Moreover, freezing and thawing for easy sectioning of lenses also could change the natural characteristics of a crystalline lens [117, 129]. Thus, the microbubble approach is a good candidate to be extended to *in vivo* studies because it can assess local mechanical properties of crystalline lenses without affecting the natural structures of a crystalline lens.

I observed location-dependent variations of Young's modulus within a lens from all three groups. The Young's modulus of old bovine lenses continuously increases approximately 10 fold from their outer cortex to their nucleus. Lenses from young bovine and porcine do not have dramatic changes in Young's modulus compared to the case of old bovine lenses; however, they also demonstrate spatial variation of Young's modulus, as reported by other groups [27, 39]. Qualitative measurements of viscoelastic properties of young (6 months old) and old (2-5 years old) porcine lenses were performed [27]. Even though they did not provide absolute values of Young's modulus, they found the tendency of the changes of mechanical properties of porcine lenses. The central part was stiffer than the cortex and the stiffness of young porcine lenses was less than that of old porcine lenses. Quantitative measurements of Young's modulus of Young (6 months old) porcine lenses showed the similar tendency with the highest Young's modulus at the center and the lowest values at the periphery [39]. In human studies, it turned out that age and location dependences of the mechanical properties of lenses were more drastic than those in animal crystalline lenses [40, 41]. Therefore, the results from animal studies cannot be directly translated to humans.

The preliminary results of shear viscosity measurements of lenses from three groups show that the microbubble approach can be used as a technique to identify the shear viscosity of a crystalline lens. The microbubble approach can differentiate shear viscosity values of different groups (Fig. 5.4(b)). Shear viscosity, as measured with the microbubble approach, changes from species to species but does not change much within one lens or one species. In the future, further studies will be performed to verify the precision and the accuracy of the microbubble approach as a measurement technique for shear viscosity.

Location-dependent variations in a lens can provide important information to develop the mechanism of accommodation. Our microbubble approach has the potential to be extended to *in vivo* experiments by combining laser-based surgical procedures in the lens such as femtosecond lentotomy [3, 143]. *In vivo* measurements of the mechanical properties of human crystalline lenses will significantly help to develop our understanding of the mechanism of accommodation and the development of presbyopia.

5.5 CONCLUSIONS

The laser-induced microbubble approach enables accurate measurements of the mechanical properties of *ex vivo* animal crystalline lenses. Age-related changes in Young's modulus were observed between old and young animal crystalline lenses. The Young's modulus at the central region of lenses from the old bovine is much higher than that from young bovine and porcine. Generally, the absolute values of Young's modulus of lenses from old bovine are larger than those from young animals. Location dependence of Young's modulus in lenses from all three groups was also found even in young animal lenses. From the Young's modulus measurements of the three groups, the central region is stiffer than the peripheral region.

Chapter 6: *Local variations of the mechanical properties of porcine vitreous humor*

ABSTRACT

Local variations of the mechanical properties of the vitreous humors of young (6 months old, n=4) and old (2-3 years old, n=4) porcine are presented. The mechanical properties of vitreous humors of the two groups were measured in an anterior-to-posterior direction. A microbubble-based acoustic radiation force approach was used to assess the local mechanical properties of vitreous humors. An impulsive acoustic radiation force was applied to a laser-induced microbubble, generated by focusing a nanosecond pulsed laser beam at various locations in vitreous, and using a custom-made high pulse repetition frequency ultrasound system enabled us to measure the dynamics of the microbubble every 10 μs. Based on measured dynamics of the microbubble, the Young's moduli of vitreous were reconstructed. No significant age-related changes in the mechanical properties of the vitreous were observed between the two groups. Young's modulus near lens (anterior) was 45.9±5.4 Pa and 37.0±4.3 Pa for young and old porcine vitreous, respectively. These values were at least 2 times and 6 times larger than Young's moduli at posterior and central regions, respectively.

6.1 INTRODUCTION

The vitreous humor is a clear gelatinous network that provides the pathway to light to make an image on the retina and the basic structures to maintain the shape of the eye globe. Water occupies almost 99% of the total weight of the vitreous and the rest of the vitreous is salt, protein (mainly collagen type II [42, 144]), glycosaminoglycans (hyaluronic acid, chondroitin sulfate, and heparin sulfate [29]), and other chemical compositions. The combination of collagen fibrils and hyaluronan is responsible for the mechanical properties of the vitreous [4, 145].

As age advances, vitreous liquefaction begins [75, 146, 147] and one possible explanation of the liquefaction is the aggregation between collagen fibrils, resulting in the collapse of the network inside the vitreous [148]. However, vitreous liquefaction with age is not fully understood because of a lack of reliable measurements of the mechanical properties of the vitreous in its natural state, which has made it difficult to understand the relationship of the chemical composition and microstructure to the mechanical properties.

Further age-related changes due to vitreous liquefaction are posterior vitreous detachment (PVD)[149, 150] and retinal detachment, which is directly related to blindness, may be caused by PVD [151-153]. For severe cases of retinal detachment, surgical intervention is needed, called vitrectomy [30, 154-156]. Vitreous substitutes, which fill the empty space of the vitreous during vitrectomy, should resemble the mechanical properties of the vitreous to maintain the proper intraocular pressure inside the eye globe and physiological actions such accommodation.

Moreover, vitreous liquefaction causes another problem regarding the pharmacological treatment of vitreoretinal diseases. To maximize the therapeutic advantages and minimize the side effects to the tissues of intravitreally injected drugs, drug concentrations and distributions should be predicted before injection [157]. The efficacy of drug delivery through the vitreous decreases due to the reduction of gradients in the drug concentration in the liquefied area, which has lower mechanical properties [158]; therefore, precise measurements of the mechanical properties of the vitreous humor help to understand drug transport in vitreous with liquefied regions.

Numerous experimental trials to measure the mechanical properties of the vitreous humor have been done: nuclear magnetic resonance imaging for the liquefaction of the vitreous [159]; dynamic mechanical measurements with compression [46]; the relaxation of the scattering pattern in the human eye [47]; bulk measurements using

cleated tools [49]; and cavitation rheology technique [50]. Researchers qualitatively measured phenomena related to physiological changes in the eyes [46, 47, 159]. By using 25 mm diameter cleated tools, the mechanical properties of bulk vitreous was measured quantitatively [49]. In this method, local mechanical properties cannot be obtained. Lately, *in vivo* measurements of the mechanical properties of vitreous humor were taken using the relationship between applied pressure and the size of cavitation bubbles at the needle tip [50]. *In vivo* measurements of the mechanical properties of the vitreous humor had higher values than those from literature results. Monotonic decrease in the mechanical properties of vitreous humor after removal from the eye due to the collapse of the internal network was also reported in previous studies [49, 50]. In our measurements, the vitreous was maintained in the eye to keep the *in vivo* state as much as possible while three regions of the vitreous were remained membrane intact for experimental necessities.

Microbubble-based acoustic radiation force was introduced as a technique to remotely measure the localized viscoelastic properties of soft tissues, by combining microbubbles created by laser-induced optical breakdown and acoustic radiation force [27, 96, 141, 160]. The measurement technique had already been applied to the eye lenses [142]. Now, with simple modifications of the measurement system, this approach can be used to measure the mechanical properties of vitreous humors.

In our previous work, I validated our theoretical model[104] of the dynamics of rounded objects such as solid spheres[102, 122] and laser-induced microbubbles[100] under acoustic radiation force in a viscoelastic medium. The high pulse repetition frequency ultrasound system was developed and tested in ex-vivo studies on bovine crystalline lenses [142]. Moreover, the measurements of Young's modulus of *ex vivo* animal crystalline lenses for various species and ages were performed[142].

In this Chapter, I measured the viscoelastic properties of the vitreous humors from 6-month old and 2 to 3-year old porcine in an anterior-to-posterior direction to explore age-related changes and location-dependent variations in the viscoelastic properties of the vitreous humor. I generated a laser-induced microbubble at four different locations in a vitreous by focusing a nanosecond laser pulse using a custom-made objective lens. After an impulsive acoustic radiation force displaced the laser-induced microbubble, the displacement of the microbubble was measured by a custom-built high pulse repetition frequency ultrasound system. Reconstruction of Young's modulus of the vitreous was performed by comparing microbubble displacements obtained by experimental measurements and theoretical calculations. I compared the mechanical properties of the vitreous humors at four different locations from the anterior to posterior of the vitreous to investigate location-dependent variations.

6.2 Materials and Methods

6.2.1 Vitreous humor preparation

Eight porcine eyes, four from 2 – 3 years old and four from 6 months old pigs, were obtained from the Sierra for Medical Science, Inc. (Whittier, CA) and they were shipped over night in the thermo-insulated box with ice packs. All the experiments were done within 10 hours after they arrived at our facility.

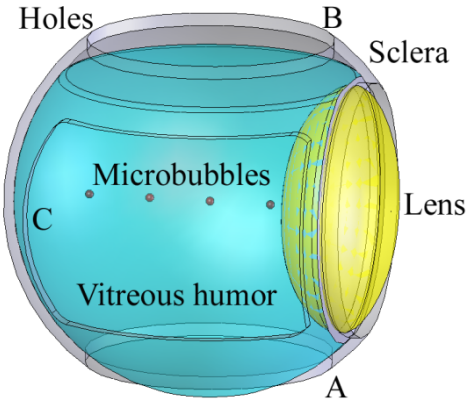

(a)

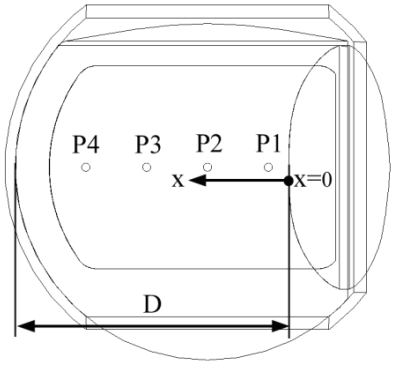

(b)

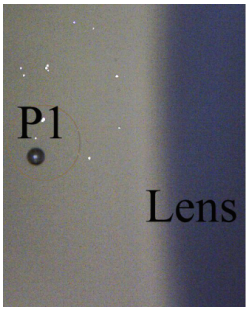

(c)

Figure 6.1: Laser-induced microbubble locations in the porcine vitreous humor. (a) 3D view of the vitreous humor with three holes (A, B, and C) in sclera. (b) Front view of vitreous humor. Laser-induced microbubbles were generated along the x-axis and positions from 1 through 4 were shown. (c) Zoomed view of the first position (P1, anterior part) and a microbubble observed by a microscope during the experiments.

Prior to the experiments, to maintain the shape and the orientation of the vitreous, I made a base that mimicked the shape of the eye with 6 wt % gelatin. The vitreous sat on the gelatin base during the microbubble experiments. For the laser-induced microbubble experiments, A, B, and C zones (Fig. 6.1(a)) were removed from the sclera for the following respective purposes: light delivery to create a laser-induced microbubble (A), ultrasound wave propagation (B), and the microbubble size observation using an optical microscope (C).

6.2.2 Microbubble generation in the vitreous humor

Laser-induced microbubbles were generated along the x-axis and positions from 1 through 4 were shown (Fig. 6.1). The first location of the laser-induced microbubble (P1 in Fig. 6.1(b) and 6.1(c)) was 500 μm from the center of the posterior of lens for all vitreous humors. The distances between two adjacent laser-induced microbubbles were 2.3 mm and 3.3 mm for young and old porcine vitreous, respectively. Thus, total distances from the first microbubble (P1) to the last microbubble (P4) were 7 mm and 10 mm for young and old porcine vitreous, respectively. Distances (D) from the surface of the lens to the apex of the vitreous were 11 and 16 mm for young and old porcine vitreous humors, respectively. Thus, the ratios of the microbubble locations (P1 – P4) to total distance (D) were kept uniform (about 0.7) for the comparison of mechanical properties of vitreous humors from young and old porcine.

6.2.3 Experimental system and signal processing

I generated laser-induced microbubbles inside the vitreous humor at desired locations by using a pulsed Nd:YAG laser (λ=532nm, Polaris II, Fremont, CA) with 5 ns pulse duration and 8 mJ energy and a custom-built objective lens that had desired numerical aperture (1.13) and working distance (8.0 mm). By focusing the laser beam

with the objective lens, I could control the shape and size of a laser-induced microbubble [109]. The size of the microbubble was monitored by an optical microscope (Dino-Lite AM411T, Wirtz, VA) operating at 230x magnification.

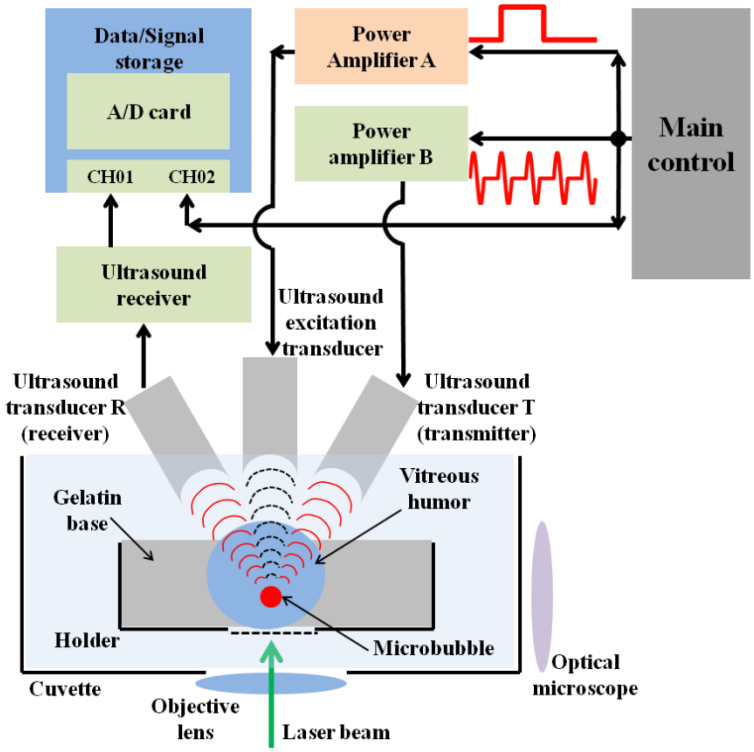

Figure 6.2: A schematic view of the experimental setup. A vitreous humor was positioned on a gelatin base that mimicked the shape of the eye globe to prevent the vitreous from collapsing in the holder and a microbubble was produced by a focused laser beam inside a vitreous. A 3.7 MHz ultrasound excitation transducer was used to generate acoustic radiation force applied to a microbubble (dashed arc). The motion of a microbubble was tracked by two 25 MHz ultrasound transducers (T and R) – the separation of transmit (T) and receive (R) transducers allowed for high pulse repetition frequency (solid arc). In this chapter, I used 100 kHz PRF for the entire experiments. In addition to ultrasound measurements, the size of the microbubble was monitored by an optical microscope.

A vitreous humor was positioned on a gelatin base in a holder. The holder was put in phosphate buffered saline (Sigma-Aldrich, Inc., St Louis, MO) to minimize the viscoelastic property changes of vitreous. The holder was attached to 3D translation stages and moved to generate laser-induced microbubbles at different locations (P1-P4 in Fig. 6.1) in the vitreous. An ultrasound excitation transducer (center frequency=3.7 MHz, F/#=2, and bandwidth=17%, Valpey Fisher, Hopkinton, MA) and ultrasound transducers T and R (center frequencies=25 MHz, F/#=4, and bandwidth=51 and 53 %, Olympus-NDT, Waltham, MA) were located at the top of the cuvette to displace and to track the microbubbles in vitreous, respectively. The foci of the three transducers were aligned at the location of the microbubble. By separating ultrasound transducers T (transmit) and R (receive), I could use desired pulse repetition frequency and set it as 100 kHz [142].

As shown in Fig. 6.2, the main control generated a train of sine pulses for pulse-echo probing using ultrasound transducers T and R and a top hat pulse for the excitation of microbubble using ultrasound excitation transducer. Both pulses for probing and excitation were amplified by radiofrequency (RF) power amplifiers A (gain=55 dB, E&I model A150, E&I, Rochester, NY) and B (gain=50dB, ENI model 2100L, ENI, Rochester, NY), respectively. The train of sine pulses from main control and the backscattered ultrasound echoes, acquired by ultrasound transducer R and amplified by the ultrasound receiver (DPR 300 Pulser / Reciever, JSR Ultrasonics, Pittsford, NY), were saved at two channels of the analog-to-digital data acquisition card (A/D card, CompuScope 12400, GaGe Inc., Montreal, Canada). Therefore, RF raw data were comprised of the train of sine pulses and backscattered ultrasound echoes. The generation of acoustic radiation pulse started with the delay of 60 μs after the first sine pulse was launched and the duration of the acoustic radiation pulse was 2.4 μs. Arrival time of the first echo defined the initial location of the microbubble and changes in the arrival times

of the following echoes determined the microbubble displacement using a cross-correlation speckle tracking method [121]. The kernel size and search window for cross-correlation tracking were 94 μm and 188 μm, respectively.

Reconstruction of Young's moduli of vitreous humors using microbubble approach was performed by finding the best fit between displacement profiles measured by the microbubble experiments and calculated by theory [100]. Once the experimentally measured time of maximum displacement of microbubble (t_{max}, Fig. 6.3) was matched to the theoretically calculated t_{max}, the value of the scaling factor of acoustic radiation force was chosen to match experimentally observed displacements with theoretically calculated displacements. Three measurements were performed to each microbubble at different positions in each sample. The shear viscosity was found by comparing decaying profiles of microbubble displacements from theory and experiments.

6.3 RESULTS

Experimentally measured and averaged displacements from three measurements at two different positions (P1 and P2 in Fig. 6.1(b)) in the young porcine vitreous humor are shown in Fig. 6.3(a). Theoretical calculations of microbubble displacements corresponding to the experimental measurements are shown in Fig. 6.3(b). Averaged Young's moduli are 12.5 Pa (thick lines) and 45.9 Pa (thin lines) and the radii of the microbubbles are 21±2 μm (thick lines) and 71±3 μm (thin lines). Times of maximum displacement (t_{max}) are indicated at Fig. 6.3. After matching t_{max} between experiments and theory, the decaying profiles were compared to find shear viscosity. For two cases in Figs 6.3(a) and 6.3(b), the shear viscosities are found as 0.025 Pa·s (thick lines) and 0.055 Pa·s (thin lines). Measured displacements of microbubbles in Fig. 6.3 are noisier than those in Chapters 4 or 5 (Figs. 4.4, 4.8, 5.2). It is not yet clear but the difference in Young's

modulus of the surrounding medium may affect noise because the vitreous humors have much lower Young's modulus than the crystalline lenses have (three orders difference in magnitude).

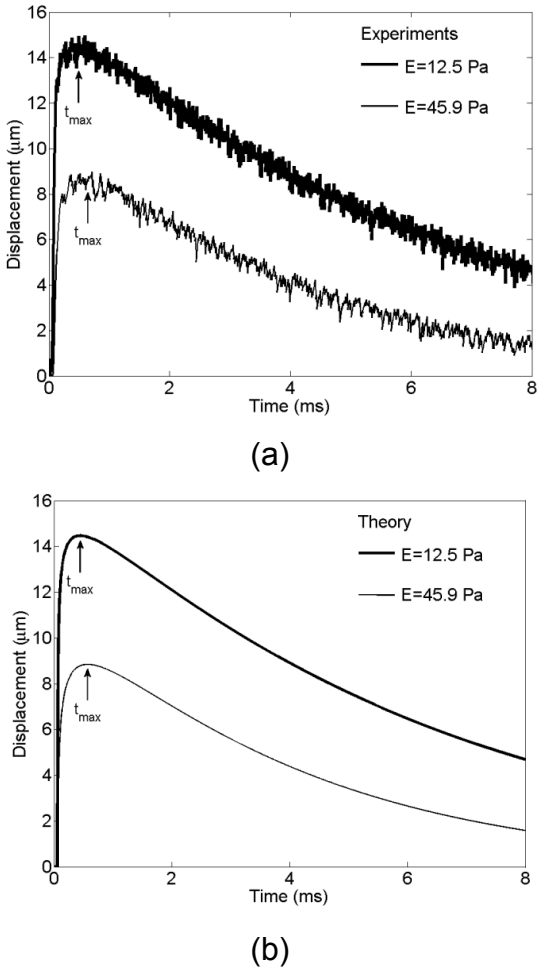

Figure 6.3: (a) Experimentally measured and averaged displacements from three trials on microbubbles at two different positions in the vitreous and (b) theoretically calculated displacements of microbubbles in response to 2.4 μs of the acoustic pulse (starting at 60 μs). Averaged Young's moduli (E) are 12.5 Pa (thick lines) and 45.9 Pa (thin lines) and the shear viscosities, used for theoretical calculations, are 0.025 Pa·s (thick line in (b)) and 0.055 Pa·s (thin line in (b)). The radii of the microbubbles are 21 ± 2 μm (thick lines) and 71 ± 3 μm (thin lines). Time of maximum displacement of microbubbles is indicated as t_{max}. Thick and thin lines in (a) and (b) correspond to dashed and solid arrows at Fig. 6.4 (a).

The dynamics of a microbubble depends on its radius (R), so direct comparison between the two cases in Fig 6.3(a) is impossible. However, because the maximum displacement of the microbubble (U_{max}) and the time of maximum displacement (t_{max}) are proportional to R [100], I can observe the general behavior of the microbubbles under acoustic radiation force in different regions. As would be expected, U_{max} in stiff region (thin line in Fig 6.3(a)) is smaller than that in soft region (thick line in Fig. 6.3(a)). However, contrary to expectation, t_{max} for stiff region (thin line) is larger than that for soft region (thick line). The reason is that the microbubble radius at stiff region (thin line) is over three times larger than that at soft region (thick line). In other words, if the same size of microbubble is considered, t_{max} at stiff region would be smaller than that at soft region as expected.

Young's modulus (E) reconstruction using laser-induced microbubbles interrogated by acoustic radiation force (duration of acoustic radiation pulse= 2.4 μs) in an anterior-to-posterior direction in the vitreous humors from young and old porcine are presented in Fig. 6.4. Measured values of Young's moduli are ranged from 2.0±0.1 to 45.9±5.4 Pa for young porcine vitreous and 5.2±0.2 to 37.0±4.3 Pa for old porcine vitreous depending on the locations within the vitreous. Anterior part (P1 in Fig. 6.1(b)) is the stiffest region and the central area has the lowest Young's modulus value as shown in Fig. 6.4. The main point is that local variation of the mechanical properties exists in an anterior-to-posterior direction in the vitreous humor. But no significant age dependence is observed for this study between the two different age groups (6 months vs. 2-3 years old).

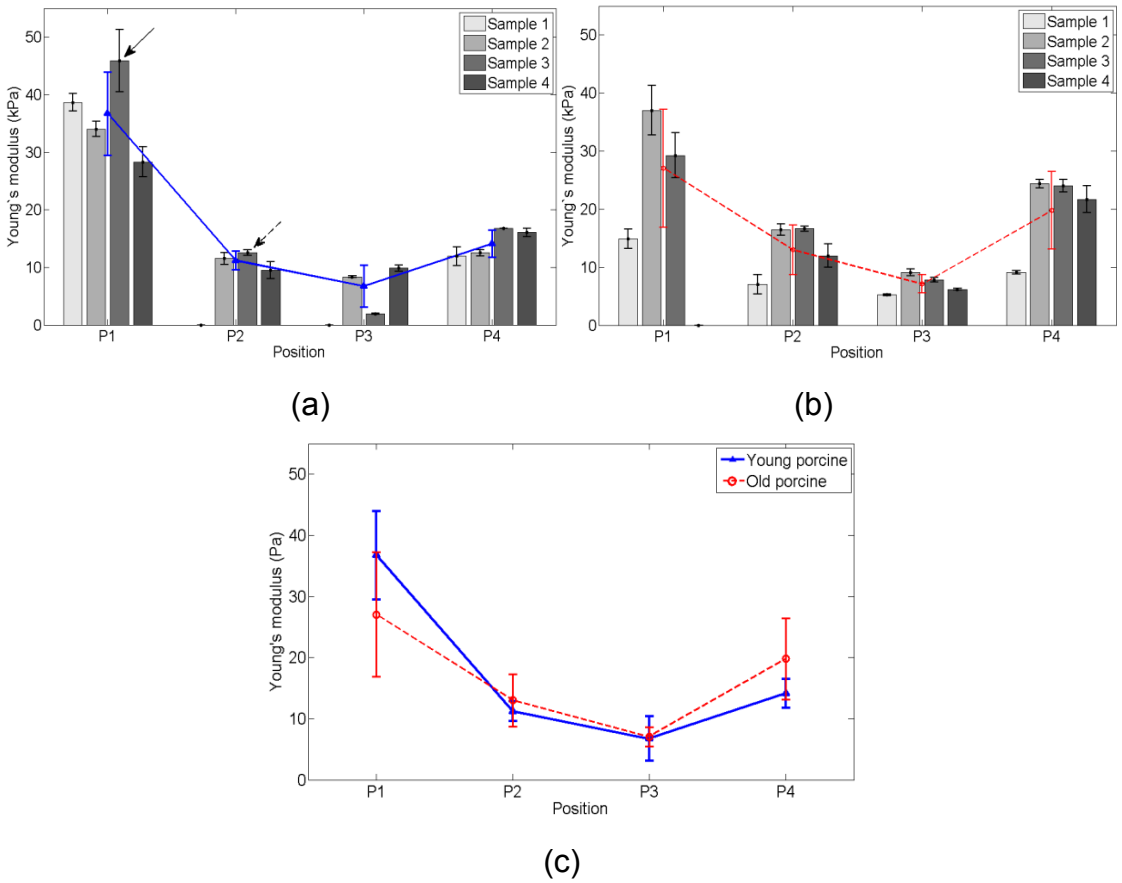

Figure 6.4: Measurements of Young's moduli of virtreous humors from (a) young porcine (6 months old) and (b) old porcine (2-3 years old). (c) Comparison of Young's modulus of vitreous between young and old porcine. Solid and dashed lines in (a), (b), and (c) are averaged Young's modulus at each position. Positions are indicated at Fig. 6.1(b). Four samples were used and three measurements were taken on one microbubble at each position. Detailed dynamics of the laser-induced microbubbles at the dashed and solid arrows are in Fig. 6.3. Error bars are plus/minus one standard deviation.

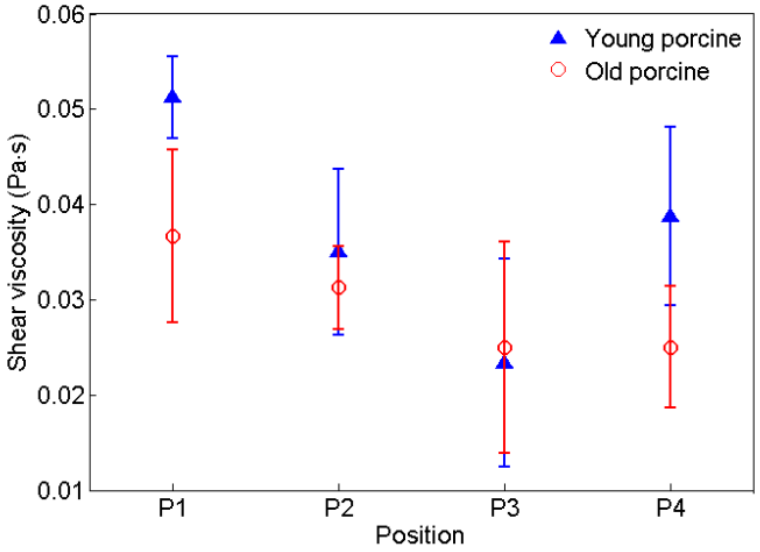

Figure 6.5: Measurements of shear viscosity. Triangles and circles indicate the shear viscosity of young porcine and old porcine, respectively. At each position, the average value and the error are from the shear viscosity values of four samples. Error bars are plus/minus one standard deviation.

The corresponding shear viscosities of vitreous humors from young (n=4) and old (n=4) porcine are ranging from 0.023±0.01 to 0.051±0.004 Pa·s and from 0.025±0.01 to 0.037±0.01 Pa·s, respectively. The shear viscosity values of the anterior and the posterior regions (P1 and P4) from Young porcine are larger than those from old porcine, but at the central regions (P2 and P3), values of the two groups overlap. The tendency of shear viscosity with respect to positions is similar to that of Young's modulus (Fig. 6.4) for both young and old vitreous.

6.4 Discussion

I measured Young's modulus of vitreous humors of young (6 months old) and old (2-3 years old) porcine using laser-induced microbubbles interrogated by acoustic radiation force. I chose pig vitreous humors as a surrogate of human vitreous after considering the several characteristics of vitreous such as volume, collagen content,

hyaluronic acid content, and protein content [161]. By using a microbubble-based acoustic radiation force approach, I could characterize the local variations of the mechanical properties of vitreous. In addition, I also compared the changes in the mechanical properties of vitreous with age, but almost no changes in Young's modulus regarding age were observed. One possible explanation of no dependence on age is that most lower mammals have relatively small changes with age in the vitreous body [161]. Thus, a human vitreous study should be done as a future study.

The shear viscosity of the vitreous also can be evaluated based on the measured dynamics of the microbubble. The shear viscosity (Fig. 6.5) has a similar local variation to Young's modulus (Fig. 6.4). The anterior part of the vitreous has higher shear viscosity than the posterior and central parts while the lowest values exist at the central regions. These preliminary results show that it is possible to use our microbubble approach to measure the shear viscosity of soft tissues. As a part of future work, I need to validate our microbubble approach to test precision and accuracy as a measurement technique for shear viscosity.

To secure the measurement positions (P1-P4 in Fig. 6.1(b)), I kept the vitreous inside the sclera, with other parts such as the lens. Difficulties in vitreous humor experiments are that no landmarks that guide the orientation of the vitreous exist and distortion of the shape of the vitreous occurs if the vitreous are taken out of the eyes. I could track the anterior, central, and posterior parts of the vitreous by observing the locations of other components, such as the lens, that could be distinguished by bare eyes (Fig. 6.1(c)). Moreover, to prevent the distortion of the vitreous during the experiments, I also made a gelatin base. The gelatin base had the same shape as the eye globe so that the prepared vitreous humor could be maintained without distortion.

Changes in the mechanical properties of vitreous with time could affect the results of measurements. Other groups [49, 50] reported that the mechanical properties of vitreous decreased monotonically after the removal of vitreous from the sclera and the changes were even accelerated if the vitreous membrane was disrupted. First of all, to avoid the time effects of the mechanical property decrease, most parts of vitreous were kept inside the sclera (Fig. 6.1). As already stated, three holes (A, B, and C in Fig. 6.1(b)) were needed for the experiment and the vitreous membranes could not be not disrupted (membrane intact). Secondly, the experiments were completed as quickly as possible. Within 5 minutes, the vitreous humor with three holes was prepared and within 20 minutes, 12 measurements, three measurements at four positions (P1-P4), were completed. Moreover, to compensate the time effects at different positions, measurements were repeatedly performed at different times. In other words, the first measurement started from the anterior part and ended at the posterior part and the second trial was done in the reverse order. The last measurement had the same order as the first one. Averaging three trials could even out the position dependent bias that might occur if the measurements were performed only in one direction.

The mechanical properties of vitreous humors of porcine, bovine and humans were reported as ranging from 0.15 to 660 Pa [46, 47, 49, 50]. Some results in the literature were extremely low compared to our results [46, 47]. The storage moduli of porcine and bovine vitreous measured with cleated tools [49] and with cavitation rheology technique [50] were comparable to our results. In our experiments, local variations within the vitreous were clearly seen for both young and old porcine vitreous humors. This result corresponds to the variations in the concentrations of collagen fibrils, reported in the literature [46]. Moreover, recently, the load-bearing struts (collagen fibrils) and tensile force (hyaluronan) hypothesis has been suggested to explain the origin

of the mechanical integrity of the vitreous [49]. By combining these observations, one possible reason for the local variations in the vitreous humors comes from the concentration differences in chemical compositions such as collagen fibrils and hyaluronic acid.

6.5 CONCLUSIONS

The mechanical properties of vitreous humors of young and old porcine were measured and local variations in Young's modulus of both groups were observed. But age dependence in Young's modulus of vitreous humors between the two groups was not clearly observed. Young's moduli at the anterior region of vitreous were higher than those at central and posterior regions while the central region had the lowest Young's modulus. The local variations of the mechanical properties in vitreous correspond to the distribution of collagen fibrils, which provide viscoelastic properties to vitreous with hyaluronan.

Chapter 7: *Conclusions and future directions*

7.1 CONTRIBUTION OF THIS WORK

The main goal of this dissertation is to develop an approach to measure the mechanical properties of soft tissues using a laser-induced microbubble interrogated by acoustic radiation force. A concomitant goal of the research was the development of a high pulse repetition frequency (PRF) ultrasound system. This system has the ability to sample the dynamics of a laser-induced microbubble under externally applied forces every 1 μs. The main contributions of the overall approach are:

1. Quantitative measurements of the mechanical properties of soft tissue by combining experimental measurement and the theoretical model.
2. The measurements of local mechanical properties of tissues.
3. Minimum invasiveness, which does not disturb the natural state of tissues.

While the first contribution of my work is a methodology of how to effectively estimate the viscoelastic properties of soft tissue, the second contribution is in terms of biological phenomena. I found age-related changes and location-dependent variations of animal crystalline lenses, which accompany the physiological changes and developmental growth of crystalline lenses [162-164]. Local variations in the porcine vitreous humor were also observed. This variations could be explained by the concentration variations of collagen fibrils and hyaluronic acid, which are responsible for the mechanical integrity of the vitreous [46, 47, 145, 165].

7.2 CONCLUSIONS

The mechanical properties of *ex vivo* animal intraocular tissues such as the crystalline lens and the vitreous humor were successfully measured using a laser-induced microbubble interrogated by acoustic radiation force. The custom-built objective lens, which had a numerical aperture of 1.13 and a working distance of 8.0 mm, effectively focused a nanosecond laser pulse to create a laser-induced microbubble at desired locations in a tissue sample. Using the microbubble as a probing tool allowed us to measure the local mechanical properties of the sample. A high pulse repetition frequency (PRF) ultrasound system accurately tracked the dynamics of the microbubble with a precision of up to 1 μs. A theoretical model that predicted the dynamics of a laser-induced microbubble displaced by externally applied forces successfully reconstructed the mechanical properties of animal ocular tissues. The combination of experimental measurements and theoretical calculations enabled us to estimate the viscoelastic properties remotely and with minimum invasiveness.

Age-related changes in Young's modulus were observed between old and young animal crystalline lenses. The absolute values of Young's modulus of lenses from old bovine are larger than those from young animals throughout the whole measurement range. The Young's modulus especially at the central region of lenses from the old bovine is much higher (5 times) than that from young bovine and porcine. Generally, location dependence of Young's modulus in lenses from all three groups was also found even in young animal lenses. From the Young's modulus measurements of lenses from old and young bovine and young porcine, the central region is stiffer than the peripheral region (2-5 times).

However, age dependence in Young's modulus of vitreous humors between the young and old porcine was not clearly observed. Young's moduli at the anterior region of

vitreous were higher than those at central and posterior regions while the central region had the lowest Young's modulus for both groups. The local variations of the mechanical properties in vitreous correspond to the distribution of collagen fibrils, which provide viscoelastic properties to vitreous with hyaluronan.

7.3 FUTURE DIRECTIONS

7.3.1 Toward *in vivo* experiments

A femtosecond laser would provide more stable and safe generation of a laser-induced microbubble. Due to its low optical breakdown threshold, damages to the collateral tissues in the eye would be greatly diminished [61, 109, 166]. In addition to employing a femtosecond laser, an objective lens with a sufficiently large numerical aperture (NA) would avoid a change of the focal spot size by nonlinear beam propagation [54, 167]. For a nanosecond laser pulse, a relatively low NA can generate a stable focal spot. However, once the pulse duration is decreased to femtosecond range, an NA of at least 0.9 is required to produce a stable focal spot size because of self-focusing [5]. It is actually impossible to achieve locally-confined energy deposition into the bulk media such as the crystalline lens and the vitreous humor with a femtosecond laser pulse using a low NA. A high NA would ensure both a smaller diffraction-limited focal diameter and a filamentation-free focal area [168-170]. Moreover, the correction of spherical aberration by employing glass elements (lens doublets or triplets) would insure that the peripheral rays and axial rays are focused into a common spot [171].

An integrated system for *in vivo* measurements of the mechanical properties of ocular tissues should be designed and developed. *In vivo* experiments are necessary, because the postmortem eye may not provide the exact viscoelastic properties of ocular tissues. However, integrating optical parts and ultrasound parts would be challenging.

First of all, the *in vivo* setting only allows us to use one side of the sample while in this dissertation I can access the sample in all directions. An integrated annular objective lens and ultrasound transducers can provide the solution to this problem. In the central part, an objective lens would be positioned and three annular transducer elements would surround the objective lens for acoustic radiation force generation and ultrasound pulse-echo probing. Because the transducer elements would have holes in the middle, the wave propagation characteristics would change. Wave propagation should be calculated and optimized using wave propagation theory such as the angular spectrum method. Secondly, coupling between the *in vivo* target and transducers should be secured. A cuvette with an impedance matching diaphragm would couple an *in vivo* eye and ultrasound transducers by filling the cuvette with water or ultrasound gel.

Optical measurement techniques may be adapted for better resolution. For example, phase-sensitive optical coherence tomography (OCT) can detect 30 nm surface modulations [122]. Because the size of a femtosecond laser-induced microbubble would be smaller than that of a nanosecond laser induced microbubble, both the time of maximum displacement and the maximum displacement of a microbubble will decrease. Thus, I would need a probing system to detect the dynamics of a microbubble with high temporal and spatial precisions. An optical measurement technique such as OCT would be a good candidate to perform this mission.

7.3.2 Mechanical property estimation using radial oscillations of a microbubble

Another method to measure the mechanical properties of soft tissues would be to use the breathing (radial oscillation) motion of a microbubble. Unlike the work performed in this dissertation, the changes of the radius of a microbubble would depend on the viscoelastic properties of the surrounding medium. This theoretical work has been

done by our group [172, 173]. The basic equation of the microbubble oscillation [172, 173] is

$$R\ddot{R}+\frac{3}{2}\dot{R}^2=\frac{1}{\rho}\left[P_g\left(\frac{R_1}{R}\right)^{3\gamma}-P_\infty-P_e(R)-\frac{2\sigma}{R}-4\eta\frac{\dot{R}}{R}\right], \qquad (7.1)$$

where R is the radius of a microbubble and $\dot{R}$ and $\ddot{R}$ are time derivatives of R. $P_e(R)\left(=\frac{1}{4\pi\rho R^2}\frac{\partial U_e}{\partial R}\right)$ is the effective pressure resulting from shear stress and U_e is the internal energy of the elastic medium. ρ, σ, γ, and η are the density of the surrounding medium, the surface tension, specific heat ratio, and shear viscosity, respectively. P_g, P_∞, and R_1 are the pressure in a microbubble, the pressure at infinity, and equilibrium microbubble radius, respectively. The second-last and the last terms in equation 7.1 indicate the effects of surface tension and viscosity, respectively.

Experimentally measured microbubble oscillation is shown in Fig. 7.1. When a laser-induced microbubble was created by an optical breakdown of a focused laser pulse, the microbubble had several (or just one) numbers of growth and collapse depending on the mechanical properties of the surrounding medium. The measurements were performed by the high PRF ultrasound system (PRF=1MHz) that was discussed in Chapter 4. The changes of the radius of a laser-induced microbubble in different bovine crystalline lenses were observed. The times of the first collapse and rebound of a microbubble depend on Young's modulus (*E)* and shear viscosity (η) of surrounding medium. The current system, unfortunately, captures the oscillation of the microbubble after the microbubble starts oscillating. As a future project, I would like to develop a system to track the oscillations of the microbuble before the oscillations start. The negative displacements in Fig. 7.1 are due to the delay between the starting point of the measurements and real oscillations.

Reconstruction of the mechanical properties of soft tissues would be achieved by the combination of the theoretical model and the experimental measurements of the oscillations of a laser-induced microbubble.

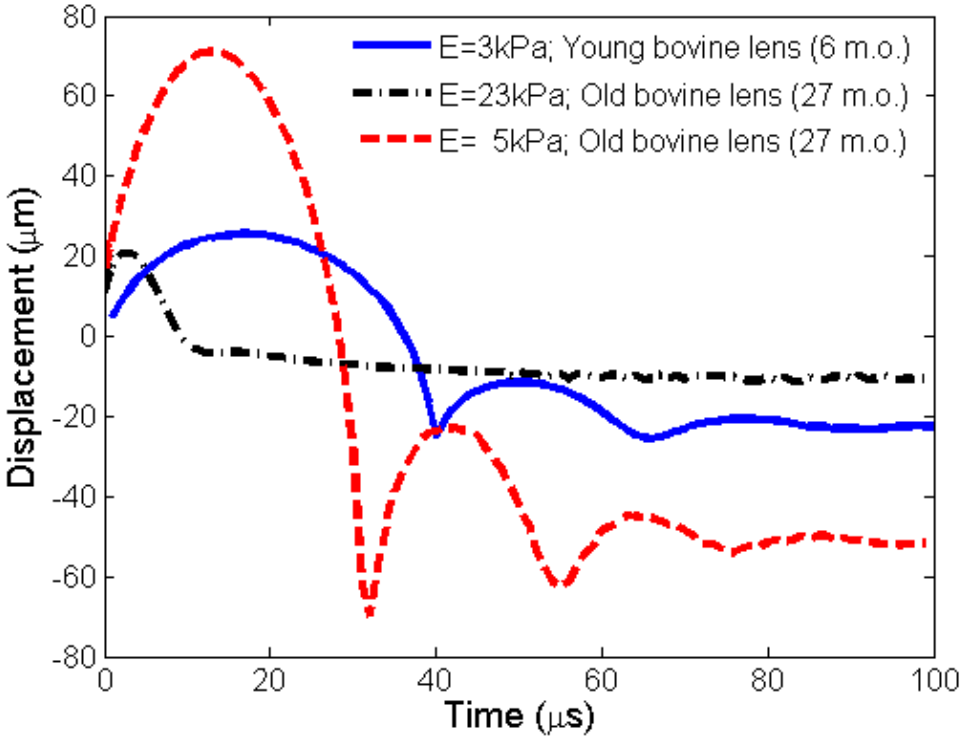

Figure 7.1: The oscillations of a laser-induced microbubble radius. Solid line indicates the bubble oscillation in a young bovine crystalline lens (Young's modulus (E) = 3kPa). Dash-dotted and dashed lines present the bubble oscillations in an old bovine crystalline lens in different locations (E=23 kPa and E= 5 kPa).

7.3.3 Reconstruction of the mechanical properties and its interpretation

Reconstruction of the mechanical properties was performed using a theoretical model of a laser-induced microbubble. Measured displacement of the microbubble was compared to the theoretical calculations. The main concern is how to minimize the gap between the theoretical model and measured displacements of the microbubble for better

reconstruction. Assumptions about the medium in the theory do not represent the exact structures of the crystalline lens and the vitreous humor. Given the natural structural anisotropy and inhomogeneous of the ocular tissues, these factors should be taken into account for future model development.

Finally, the macro-level of studies, the reconstruction of the mechanical properties, would be combined with the microstructure and molecular point of view. To date, these two areas in biomedical engineering have built own territories rather than mingled together. The clinical meaning of reconstructed mechanical properties should be interpreted as biochemical aspects and vice-versa. Thus, clinical diagnosis and therapeutic planning for disease treatment would effectively be achieved when these two areas will work in concert.

Bibliography

[1] G. Gerten, T. Ripken, P. Breitenfeld, R. R. Krueger, O. Kermani, H. Lubatschowski, and U. Oberheide, "[In vitro and in vivo investigations on the treatment of presbyopia using femtosecond lasers]," *Ophthalmologe,* vol. 104, pp. 40-6, Jan 2007.

[2] H. Lubatschowski, S. Schumacher, M. Fromm, A. Wegener, H. Hoffmann, U. Oberheide, and G. Gerten, "Femtosecond lentotomy: generating gliding planes inside the crystalline lens to regain accommodation ability," *J Biophotonics,* vol. 3, pp. 265-8, Jun 2011.

[3] T. Ripken, U. Oberheide, M. Fromm, S. Schumacher, G. Gerten, and H. Lubatschowski, "fs-Laser induced elasticity changes to improve presbyopic lens accommodation," *Graefes Arch Clin Exp Ophthalmol,* vol. 246, pp. 897-906, Jun 2008.

[4] F. W. Newell, *Ophthalmology: principles and concepts*, 7 ed. St. Louis, MO: Mosby-Year Book, Inc., 1991.

[5] R. C. Augusteyn, "On the growth and internal structure of the human lens," *Exp Eye Res,* vol. 90, pp. 643-54, Jun 2010.

[6] S. Bassnett, Y. Shi, and G. F. Vrensen, "Biological glass: structural determinants of eye lens transparency," *Philos Trans R Soc Lond B Biol Sci,* vol. 366, pp. 1250-64, Apr 27 2011.

[7] S. Duke-Elder and K. C. Sybar, *System of Ophthalmology* vol. II. St. Louis: The CV Mosby Company, 1961.

[8] N. Brown, "The change in shape and internal form of the lens of the eye on accommodation," *Exp Eye Res,* vol. 15, pp. 441-59, Apr 1973.

[9] R. S. Wilson, "Does the lens diameter increase or decrease during accommodation? Human accommodation studies: a new technique using infrared retro-illumination video photography and pixel unit measurements," *Trans Am Ophthalmol Soc,* vol. 95, pp. 261-7; discussion 267-70, 1997.

[10] H. v. Helmholtz, *Treatise on physiological optics, Volume I*, translated from 3rd German edition by JPC Southall ed. Rochester: Opt. Soc. Am., 1924.

[11] M. H. E. Tscherning, *Physilogic optics*: Philadelphia: Key Stone, 1924.

[12] S. A. Strenk, L. M. Strenk, and J. F. Koretz, "The mechanism of presbyopia," *Prog Retin Eye Res,* vol. 24, pp. 379-93, May 2005.

[13] R. Weale, "Presbyopia toward the end of the 20th century," *Surv Ophthalmol,* vol. 34, pp. 15-30, Jul-Aug 1989.

[14] B. Pierscionek, "What we know and understand about presbyopia," *Clin. Exp. Optom.,* vol. 76, 1993.

[15] B. Gilmartin, "The aetiology of presbyopia: a summary of the role of lenticular and extralenticular structures," *Ophthalmic Physiol Opt,* vol. 15, pp. 431-7, Sep 1995.

[16] M. A. Croft, A. Glasser, and P. L. Kaufman, "Accommodation and presbyopia," *Int Ophthalmol Clin,* vol. 41, pp. 33-46, Spring 2001.

[17] D. A. Atchison, "Accommodation and presbyopia," *Ophthalmic Physiol Opt,* vol. 15, pp. 255-72, Jul 1995.

[18] H. Lubatschowski, "Overview of commercially available femtosecond lasers in refractive surgery," *J Refract Surg,* vol. 24, pp. S102-7, Jan 2008.

[19] A. Duane, "Studies in Monocular and Binocular Accommodation, with Their Clinical Application," *Trans Am Ophthalmol Soc,* vol. 20, pp. 132-57, 1922.

[20] A. Duane, "Subnormal Accommodation," *Trans Am Ophthalmol Soc,* vol. 23, pp. 159-83, 1925.

[21] W. N. Charman, "The eye in focus: accommodation and presbyopia," *Clin Exp Optom,* vol. 91, pp. 207-25, May 2008.

[22] V. L. Taylor, K. J. al-Ghoul, C. W. Lane, V. A. Davis, J. R. Kuszak, and M. J. Costello, "Morphology of the normal human lens," *Invest Ophthalmol Vis Sci,* vol. 37, pp. 1396-410, Jun 1996.

[23] K. O. Gilliland, S. Metlapally, and M. J. Costello, "Morphological analysis of extensive fiber cell compaction in the adult nucleus of aged human transparent lenses," *IOVS 2009,* vol. 50, pp. ARVO E-Abstract 4388, 2009.

[24] K. J. Al-Ghoul, R. K. Nordgren, A. J. Juszak, C. D. Freel, M. J. Costello, and J. R. Kuszak, "Structural evidence of human nuclear fiber compaction as a function of ageing and cataractogenesis " *Exp. Eye Res.,* vol. 72, pp. 199-214, 2001.

[25] B. K. Pierscionek and D. Y. Chan, "Refractive index gradient of human lenses," *Optom Vis Sci,* vol. 66, pp. 822-9, Dec 1989.

[26] S. A. Goss, F. A. Frizzel, and F. Dunn, "Dependence of the ultrasonic properties of biological tissues on constituent proteins," *J. Acoust. Soc. Am.,* vol. 67, pp. 1041-1044, 1980.

[27] T. N. Erpelding, K. W. Hollman, and M. O'Donnell, "Mapping age-related elasticity changes in porcine lenses using bubble-based acoustic radiation force," *Exp Eye Res,* vol. 84, pp. 332-41, Feb 2007.

[28] H. Tabandeh, M. Wilkins, G. Thompson, D. Nassiri, and A. Karim, "Hardness and ultrasonic characteristics of the human crystalline lens," *J Cataract Refract Surg,* vol. 26, pp. 838-41, Jun 2000.

[29] R. J. Truscott and R. C. Augusteyn, "Changes in human lens proteins during nuclear cataract formation," *Exp Eye Res,* vol. 24, pp. 159-70, Feb 1977.

[30] P. A. Wilmarth, S. Tanner, S. Dasari, S. R. Nagalla, M. A. Riviere, V. Bafna, P. A. Pevzner, and L. L. David, "Age-related changes in human crystallins determined from comparative analysis of post-translational modifications in young and aged lens: does deamidation contribute to crystallin insolubility?," *J Proteome Res,* vol. 5, pp. 2554-66, Oct 2006.

[31] R. F. Fisher, "The elastic constants of the human lens," *J Physiol,* vol. 212, pp. 147-80, Jan 1971.

[32] R. F. Fisher, "Presbyopia and the changes with age in the human crystalline lens," *J Physiol,* vol. 228, pp. 765-79, Feb 1973.

[33] H. Pau and J. Kranz, "The increasing sclerosis of the human lens with age and its relevance to accommodation and presbyopia," *Graefes Arch Clin Exp Ophthalmol,* vol. 229, pp. 294-6, 1991.

[34] G. W. van Alphen and W. P. Graebel, "Elasticity of tissues involved in accommodation," *Vision Res,* vol. 31, pp. 1417-38, 1991.

[35] P. Heyworth, G. M. Thompson, H. Tabandeh, and S. McGuigan, "The relationship between clinical classification of cataract and lens hardness," *Eye (Lond),* vol. 7 (Pt 6), pp. 726-30, 1993.

[36] E. I. Assia, I. Medan, and M. Rosner, "Correlation between clinical, physical and histopathological characteristics of the cataractous lens," *Graefes Arch Clin Exp Ophthalmol,* vol. 235, pp. 745-8, Dec 1997.

[37] P. K. Sharma, H. J. Busscher, T. Terwee, S. A. Koopmans, and T. G. van Kooten, "A comparative study on the viscoelastic properties of human and animal lenses," *Exp Eye Res,* vol. 93, pp. 681-8, Nov 2011.

[38] H. J. Burd, G. S. Wilde, and S. J. Judge, "An improved spinning lens test to determine the stiffness of the human lens," *Exp Eye Res,* vol. 92, pp. 28-39, Jan 2011.

[39] M. Reilly and N. Ravi, "Microindentation of the young porcine ocular lens," *J Biomech Eng,* vol. 131, p. 044502, Apr 2009.

[40] K. R. Heys, S. L. Cram, and R. J. Truscott, "Massive increase in the stiffness of the human lens nucleus with age: the basis for presbyopia?," *Mol Vis,* vol. 10, pp. 956-63, Dec 16 2004.

[41] H. A. Weeber, G. Eckert, W. Pechhold, and R. G. van der Heijde, "Stiffness gradient in the crystalline lens," *Graefes Arch Clin Exp Ophthalmol,* vol. 245, pp. 1357-66, Sep 2007.

[42] P. Bishop, "Structural macromolecules and supramolecular organisation of the vitreous gel," *Prog. Retina Eye Res.,* vol. 19, pp. 322-344, 2000.

[43] I. Fatti, "Hydraulic flow conductivity of the vitreous gel," *Invest. Ophthalmol. Otolaryngol.,* vol. 76, pp. 480-497, 1977.

[44] A. J. Coulombre, "The role of intraocular pressure in the development of the chicken eye.," *J. Exp. Zool. ,* vol. 133, pp. 211-223, 1956.

[45] W. S. Foulds, "Is your vitreous really necessary? The role of the vitreous in the eye with particular reference to retinal attachment, detachment and the mode of action of vitreous substitutes," *Eye (Lond),* vol. 1 (Pt 6), pp. 641-64, 1987.

[46] F. A. Bettelheim and T. J. Wang, "Dynamic viscoelastic properties of bovine viterous," *Exp Eye Res,* vol. 23, pp. 435-41, Oct 1976.

[47] R. L. Zimmerman, "In vivo measurements of the viscoelasticity of the human vitreous humor," *Biophys J,* vol. 29, pp. 539-44, Mar 1980.

[48] B. Lee, M. Litt, and G. Buchsbaum, "Rheology of the vitreous body: Part 2. Viscoelasticity of bovine and porcine vitreous," *Biorheology,* vol. 31, pp. 327-38, Jul-Aug 1994.

[49] C. S. Nickerson, J. Park, J. A. Kornfield, and H. Karageozian, "Rheological properties of the vitreous and the role of hyaluronic acid," *J Biomech,* vol. 41, pp. 1840-6, 2008.

[50] J. A. Zimberlin, J. J. McManus, and A. J. Crosby, "Cavitation rheology of the vitreou: mechanical properties of biological tissue," *Soft Matt,* vol. 6, pp. 3632-3635, 2010.

[51] A. Vogel and W. Lauterborn, "Acoustic transient generation by laser-produced cavitation bubbles near solid boundaries," *J. Acoust. Soc. Am.,* vol. 84, pp. 719-731, 1988.

[52] B. Zysset, J. G. Fujimoto, and T. F. Deutsch, "Time-resolved measurements of picosecond optical breakdown," *Appl. Phys. B.,* vol. 48, pp. 139-147, 1989.

[53] P. A. Barnes and K. E. Rieckhoff, "Laser induced underwater sparks," *Appl. Phys. Lett.,* vol. 13, pp. 282-284, 1968.

[54] A. Vogel, W. Hentschel, J. Holzfuss, and W. Lauterborn, "Cavitation bubble dynamics and acoustic transient generation in ocular surgery with pulsed neodymium: YAG lasers," *Ophthalmology,* vol. 93, pp. 1259-69, Oct 1986.

[55] J. W. Rayleigh, "On the pressure developed in a liquid during the collapse of a spherical cavity," *Phil. Mag.,* vol. 34, p. 94, 1917.

[56] J. F. Ready, *Effects of high-power laser radiaion*. Orlando, FL: Academic, 1971.

[57] A. Vogel, K. Nahen, D. Theisen, and J. Noack, "Plasma formation in water by picosecond and nanosecond pulses- part I: optical breakdown at threshold and superthreshold irradiance," *IEEE J. Sel. Top. Quant. Electron,* vol. 2, pp. 847-860, 1996.

[58] N. Bloembergen, "Laser-induced breakdown in solids," *IEEE J. Quantum Electron.,* vol. 10, pp. 375-386, 1974.

[59] P. K. Kennedy, "A first-order model for computation of laser-induced breakdown thresholds in ocular and aqueous medi: Part I-theory," *IEEE J. Quantum Electron.,* vol. 31, pp. 2241-2249, 1995.

[60] J. Noack and A. Vogel, "Laser-induced plasma formation in water at nanosecond to femtosecond time scales: calculation of thresholds, absoprtion coefficients, and energe density," *IEEE J. Quantum Electron.,* vol. 35, pp. 1156-1166, 1999.

[61] A. Vogel, J. Noack, K. Nahen, D. Theisen, S. Busch, U. Parliiz, D. X. Hammer, G. D. Noojin, B.A.Rockwell, and R. Birngruber, "Energy balance of optical breakdown in water at nanosecond to femtosecond time scales," *Appl. Phys. B.,* vol. 68, pp. 271-280, 1999.

[62] O. Kermani, F. Will, O. Massow, U. Oberheide, and H. Lubatschowski, "Control of femtosecond thin-flap LASIK using OCT in human donor eyes," *J Refract Surg,* vol. 26, pp. 57-60, Jan 2010.

[63] H. Lubatschowski, S. Schumacher, M. Fromm, A. Wegener, H. Hoffmann, U. Oberheide, and G. Gerten, "Femtosecond lentotomy: generating gliding planes inside the crystalline lens to regain accommodation ability," *J Biophotonics,* vol. 3, pp. 265-8, Jun 2010.

[64] X. Liu and G. Mourou. (August 1997) Ultrashort laser pulses tackle precision machining. *Laser Focus World*. 118.

[65] D. Stern, R. W. Schoenlein, C. A. Puliafito, E. T. Dobi, R. Birngruber, and J. G. Fujimoto, "Corneal ablation by nanosecond, picosecond, and femtosecond lasers at 532 and 625 nm," *Arch Ophthalmol,* vol. 107, pp. 587-92, Apr 1989.

[66] R. M. Kurtz, X. Liu, V. M. Elner, J. A. Squier, D. Du, and G. A. Mourou, "Photodisruption in the human cornea as a function of laser pulse width," *J Refract Surg,* vol. 13, pp. 653-8, Nov-Dec 1997.

[67] T. Juhasz, F. H. Loesel, C. Horvath, R. M. Kurtz, and G. Mourou, *Femtosecond laser for ultra-accurate surgery: application to corneal surgery* vol. 9. Berlin: Springer, 1998.

[68] A. Sugar, "Ultrafast (femtosecond) laser refractive surgery," *Curr Opin Ophthalmol,* vol. 13, pp. 246-9, Aug 2002.

[69] R. Myers and R. Krueger, "Novel approaches to correction of presbyopia with laser modification of the crystalline lens " *J. Refract. Surg.,* vol. 14, pp. 136-139, 1998.

[70] R. R. Krueger, X. K. Sun, J. Stroh, and R. Myers, "Experimental increase in accommodative potential after neodymium: yttrium-aluminum-garnet laser photodisruption of paired cadaver lenses," *Ophthalmology,* vol. 108, pp. 2122-9, Nov 2001.

[71] H. Lubatschowski, G. Maatz, A. Heisterkamp, U. Hetzel, W. Drommer, H. Welling, and W. Ertmer, "Application of ultrashort laser pulses for intrastromal refractive surgery," *Graefes Arch Clin Exp Ophthalmol,* vol. 238, pp. 33-9, Jan 2000.

[72] A. Heisterkamp, T. Mamom, O. Kermani, W. Drommer, H. Welling, W. Ertmer, and H. Lubatschowski, "Intrastromal refractive surgery with ultrashort laser

pulses: in vivo study on the rabbit eye," *Graefes Arch Clin Exp Ophthalmol,* vol. 241, pp. 511-7, Jun 2003.

[73] J. Ophir, I. Cespedes, H. Ponnekanti, Y. Yazdi, and X. Li, "Elastography: a quantitative method for imaging the elasticity of biological tissues," *Ultrason Imaging,* vol. 13, pp. 111-34, Apr 1991.

[74] H. L. Oestreicher, "Field and impedance of an oscillating sphere ina viscoelastic medium with an application to biophysics," *J Acoust Soc Am,* vol. 23, pp. 707-714, 1951.

[75] S. Chen, M. Fatemi, and J. F. Greenleaf, "Remote measurement of material properties from radiation force induced vibration of an embedded sphere," *J Acoust Soc Am,* vol. 112, pp. 884-9, Sep 2002.

[76] A. P. Sarvazyan, O. V. Rudenko, S. D. Swanson, J. B. Fowlkes, and S. Y. Emelianov, "Shear wave elsticitiy imagin: a new ultrasonic technology of medical diagnostics," *Ultrasound Med Biol,* vol. 24, pp. 1419-1435, 1998.

[77] K. R. Nightingale, M. L. Palmeri, R. W. Nightingale, and G. E. Trahey, "On the feasibility of remote palpation using acoustic radiation force," *J Acoust Soc Am,* vol. 110, pp. 625-34, Jul 2001.

[78] B. J. Fahey, K. R. Nightingale, S. A. McAleavey, M. L. Palmeri, P. D. Wolf, and G. E. Trahey, "Acoustic radiation force impulse imaging of myocardial radiofrequency ablation: initial in vivo results," *IEEE Trans. Ultrason., Ferroelect., Freq. Contr., ,* vol. 52, pp. 631-642, 2005.

[79] B. J. Fahey, K. R. Nightingale, R. C. Nelson, M. L. Palmeri, and G. E. Trahey, "Acoustic radiation force impulse imaging of the abdomen: demonstration of feasibility and utility," *Ultrasound Med Biol,* vol. 31, pp. 1185-98, Sep 2005.

[80] B. J. Fahey, R. C. Nelson, S. J. Hsu, D. P. Bradway, D. M. Dumont, and G. E. Trahey, "In vivo guidance and assessment of liver radio-frequency ablation with acoustic radiation force elastography," *Ultrasound Med Biol,* vol. 34, pp. 1590-603, Oct 2008.

[81] J. Bercoff, M. Tanter, and M. Fink, "Supersonic shear imaging: a new technique for soft tissue elasticity mapping," *IEEE Trans Ultrason Ferroelectr Freq Control,* vol. 51, pp. 396-409, Apr 2004.

[82] M. Tanter, D. Touboul, J. L. Gennisson, J. Bercoff, and M. Fink, "High-resolution quantitative imaging of cornea elasticity using supersonic shear imaging," *IEEE Trans Med Imaging,* vol. 28, pp. 1881-93, Dec 2009.

[83] T. Deffieux, G. Montaldo, M. Tanter, and M. Fink, "Shear wave spectroscopy for in vivo quantification of human soft tissues visco-elasticity," *IEEE Trans Med Imaging,* vol. 28, pp. 313-22, Mar 2009.

[84] W. F. Walker, F. J. Fernandez, and L. A. Negron, "A method of imaging viscoelastic parameters with acoustic radiation force," *Phys Med Biol,* vol. 45, pp. 1437-47, Jun 2000.

[85] F. Viola and W. F. Walker, "Radiation force imaging of viscoelastic properties with reduced artifacts," *IEEE Trans Ultrason Ferroelectr Freq Control,* vol. 50, pp. 736-42, Jun 2003.

[86] F. Viola, M. D. Kramer, M. B. Lawrence, J. P. Oberhauser, and W. F. Walker, "Sonorheometry: a noncontact method for the dynamic assessment of thrombosis," *Ann Biomed Eng,* vol. 32, pp. 696-705, May 2004.

[87] A. Alizad, M. Walch, J. F. Greenleaf, and M. Fatemi, "Vibrational characteristics of bone fracture and fracture repair: application to excised rat femur," *J Biomech Eng,* vol. 128, pp. 300-8, Jun 2006.

[88] C. Pislaru, B. Kantor, R. R. Kinnick, J. L. Anderson, M. C. Aubry, M. W. Urban, M. Fatemi, and J. F. Greenleaf, "In vivo vibroacoustography of large peripheral arteries," *Invest Radiol,* vol. 43, pp. 243-52, Apr 2008.

[89] L. Rayligh, *The theory of sound* vol. 1. London: Macmillan 1877.

[90] L. Brillouin, "Sur les tensions de radiation," *Ann. Phys.,* vol. 4, pp. 528-586, 1925.

[91] L. V. King, "On the acoustic radiation pressure on spheres," *Proc. R. Soc. Lond. A,* vol. 147, pp. 212-240, 1934.

[92] P. J. Westervelt, "Acoustic radiation pressure," *J. Acoust. Soc. Am.,* vol. 29, pp. 26-29, 1957.

[93] A. Prosperetti, "Bubble phenomena in sound fields. II," *Ultrasonics,* vol. 22, pp. 115-124, 1984.

[94] T. G. Leighton, *The acoustic bubble*. San Diego: Academic, 1994.

[95] L. D. Landau and E. M. Lifshitz, *Fluid mechanics*, 2 ed. Burlington, MA: Butterworth-Heinemann, 1987.

[96] T. N. Erpelding, K. W. Hollman, and M. O'Donnell, "Bubble-based acoustic radiation force elasticity imaging," *IEEE Trans Ultrason Ferroelectr Freq Control,* vol. 52, pp. 971-9, Jun 2005.

[97] T. N. Erpelding, K. W. Hollman, and M. O'Donnell, "Bubble-based acoustic radiation force using chirp insonation to reduce standing wave effects," *Ultrasound Med Biol,* vol. 33, pp. 263-9, Feb 2007.

[98] K. W. Hollman, M. O'Donnell, and T. N. Erpelding, "Mapping elasticity in human lenses using bubble-based acoustic radiation force," *Exp Eye Res,* vol. 85, pp. 890-3, Dec 2007.

[99] T. N. Erpelding, K. W. Hollman, and M. O'Donnell, "Spatially mapping the elastic properties of the lens using bubble-based acoustic radiation force," in *IEEE Ultrasonics Symposium* 2005, pp. 613-616.

[100] S. Yoon, S. R. Aglyamov, A. B. Karpiouk, S. Kim, and S. Y. Emelianov, "Estimation of mechanical properties of a viscoelastic medium using a laser-induced microbubble interrogated by an acoustic radiation force," *J Acoust Soc Am,* vol. 130, pp. 2241-8, Oct 2011.

[101] S. R. Aglyamov, A. B. Karpiouk, Y. A. Ilinskii, E. A. Zabolotskaya, and S. Y. Emelianov, "Motion of a solid sphere in a viscoelastic medium in response to applied acoustic radiation force: Theoretical analysis and experimental verification," *J Acoust Soc Am,* vol. 122, pp. 1927-36, Oct 2007.

[102] A. B. Karpiouk, S. R. Aglyamov, Y. A. Ilinskii, E. A. Zabolotskaya, and S. Y. Emelianov, "Assessment of shear modulus of tissue using ultrasound radiation force acting on a spherical acoustic inhomogeneity," *IEEE Trans Ultrason Ferroelectr Freq Control,* vol. 56, pp. 2380-7, Nov 2009.

[103] Y. A. Ilinskii, G. D. Meegan, E. A. Zabolotskaya, and S. Y. Emelianov, "Gas bubble and solid sphere motion in elastic media in response to acoustic radiation force," *J Acoust Soc Am,* vol. 117, pp. 2338-46, Apr 2005.

[104] Y. A. Ilinskii and E. A. Zabolotskaya, "Cooperative radiation and scattering of acoustic waves by gas bubbles in liquid," *J. Acoust. Soc. Am.,* vol. 92, pp. 2837-2841, 1992.

[105] T. Hasegawa and K. Yosioka, "Acoustic-radiation force on a solid elastic sphere," *J. Acoust. Soc. Am.,* vol. 46, pp. 1139-1143, 1969.

[106] A. P. Sarvazyan, "Low-frequency acoustic characteristics of biological tissues," *Mech. Compos. Mater.,* vol. 11, pp. 594-597, 1975.

[107] D. D. Von Hoff, P. J. Goodman, C. A. Presant, R. L. Ruxer, J. S. MacDonald, J. J. Costanzi, R. L. Stephens, and S. J. Vogel, "A phase II trial of continuous infusion

vinblastine in patients with gastric carcinoma. A Southwest Oncology Group study," *Eur J Cancer,* vol. 26, pp. 405-7, Mar 1990.

[108] A. Vogel, "Nonlinear absorption: intraocular microsurgery and laser lithotripsy," *Phys Med Biol,* vol. 42, pp. 895-912, May 1997.

[109] A. Vogel, J. Noack, G. Huttman, and G. Paltauf, "Mechanisms of femtosecond laser nanosurgery of cells and tissues," *Appl. Phys. B.,* vol. 81, pp. 1015-1047, 2005.

[110] R. F. Steinert and C. A. Puliafito, *The Nd:YAG laser in ophthalmology*. Philadelphia, PA: Saunders, 1985.

[111] A. Olmes, S. Lohmann, H. Lubatschowski, and W. Ertmer, "An improved method of measuring laser induced pressure transients," *Appl. Phys. B-Lasers,* vol. 64, pp. 667-682, 1997.

[112] A. Vogel, M. R. C. Capon, M. N. Asiyo-Vogel, and R. Birngruber, "Intraocular Photodisruption With Picosecond and Nanosecond Laser Pulses: Tissue Effects in Cornea, Lens, and Retina," *Invest. Ophthalmol. Vis. Sci.,* vol. 35, pp. 3032-3044, 1994.

[113] S. V. Patel, L. H. Maguire, J. W. McLaren, D. O. Hodge, and W. M. Bourne, "Femtosecond laser versus mechanical microkeratome for LASIK," *Ophthalmology,* vol. 114, p. 1487~1490, 2007.

[114] R. Montes-Mico, A. Rodriguez-Galietero, and J. L. Alio, "Femtosecond laser versus mechanical keratome LASIK for myopia," *Ophthalmology,* vol. 114, p. 62~68, 2007.

[115] W. F. Walker, "Internal deformation of a uniform elastic solid by acoustic radiation force," *J. Acoust. Soc. Am.,* vol. 105, p. 2508~2518, 1999.

[116] Y. Kikkawa and T. Sato, "Elastic properties of the lens," *Exp Eye Res,* vol. 2, pp. 210-5, Apr 1963.

[117] H. A. Weeber, G. Eckert, F. Soergel, C. H. Meyer, W. Pechhold, and R. G. van der Heijde, "Dynamic mechanical properties of human lenses," *Exp Eye Res,* vol. 80, pp. 425-34, Mar 2005.

[118] F. Soergel, C. Meyer, G. Eckert, B. Abele, and W. Pechhold, "Spectral analysis of viscoelasticity of the human lens," *J Refract Surg,* vol. 15, pp. 714-6, Nov-Dec 1999.

[119] M. Itoi, N. Ito, and H. Kaneko, "Visco-elastic properties of the lens," *Exp Eye Res,* vol. 4, pp. 168-73, Sep 1965.

[120] H. A. Weeber and R. G. van der Heijde, "Internal deformation of the human crystalline lens during accommodation," *Acta Ophthalmol,* vol. 86, pp. 642-7, Sep 2008.

[121] M. A. Lubinski, S. Y. Emelianov, and M. O'Donnell, "Speckle tracking methods for ultrasonic elasticity imaging using short-time correlation," *IEEE Trans Ultrason Ferroelectr Freq Control,* vol. 46, pp. 82-96, 1999.

[122] R. K. Manapuram, S. A. Baranov, V.G.R. Manne, N. Sudheendran, M. Mashiatulla, S. Aglyamov, S. Emelianov, and K. V. Larin, "Assessment of wave propagation on surfaces of crystalline lens with phase sensitive optical coherence tomography," *Laser Phys. Lett.,* vol. 8, pp. 164-168, 2011.

[123] R. A. Schachar, T. D. Black, R. L. Kash, D. P. Cudmore, and D. J. Schanzlin, "The mechanism of accommodation and presbyopia in the primate," *Ann Ophthalmol,* vol. 27, pp. 59-67, 1995.

[124] T. J. Hall, M. Bilgen, M. F. Insana, and T. A. Krouskop, "Phantom materials for elastography," *IEEE Trans. Ultrason., Ferroelect., Freq. Contr.,,* vol. 44, pp. 1355-1365, 1997.

[125] R. A. Schachar, "Cause and treatment of presbyopia with a method for increasing the amplitude of accommodation," *Ann Ophthalmol,* vol. 24, pp. 445-7, 452, Dec 1992.

[126] R. A. Schachar, T. D. Black, R. L. Kash, D. P. Cudmore, and D. J. Schanzlin, "The mechanism of accommodation and presbyopia in the primate," *Ann Ophthalmol,* vol. 27, pp. 59-67, 1995.

[127] R. A. Schachar, "Qualitative effect of zonular tension on freshly extracted intact human crystalline lenses: implications for the mechanism of accommodation," *Invest Ophthalmol Vis Sci,* vol. 45, pp. 2691-5, Aug 2004.

[128] H. J. Burd, S. J. Judge, and M. J. Flavell, "Mechanics of accommodation of the human eye," *Vision Res,* vol. 39, pp. 1591-5, May 1999.

[129] R. A. Schachar, R. W. Chan, and M. Fu, "Viscoelastic properties of fresh human lenses under 40 years of age: implications for the aetiology of presbyopia," *Br J Ophthalmol,* vol. 95, pp. 1010-3, Jul 2011.

[130] F. Yang, "Indentation of an incompressible elastic film," *Mech Matter,* vol. 30, pp. 275-286, 1998.

[131] B. Patnaik, "A photographic study of accommodative mechanisms: changes in the lens nucleus during accommodation," *Invest Ophthalmol,* vol. 6, pp. 601-11, Dec 1967.

[132] W. Drexler, A. Baumgartner, O. Findl, C. Hitzenberger, and A. Fercher, "Biometric investigation of changes in the anterior eye segment during accommodation," *Vision Res,* vol. 37, pp. 2789-2800, 1997.

[133] W. R. Coates, "Amplitudes of accommodation in South Africa," *Br J Physiol Opt,* vol. 12, pp. 76-81; passim, Apr 1955.

[134] M. J. Turner, "Observations on the normal subjective amplitude of accommodation," *Br J Physiol Opt,* vol. 15, pp. 70-100, Apr 1958.

[135] S. R. Cobb, "An Investigation into Accommodation by Ayrshire Study Circle," *Br J Physiol Opt,* vol. 21, pp. 31-5, Jan-Mar 1964.

[136] A. P. Beers and G. L. Van der Heijde, "Presbyopia and velocity of sound in the lens," *Optom Vis Sci,* vol. 71, pp. 250-3, Apr 1994.

[137] S. T. Bailey, M. D. Twa, J. C. Gump, M. Venkiteshwar, M. A. Bullimore, and R. Sooryakumar, "Light-scattering study of the normal human eye lens: elastic properties and age dependence," *IEEE Trans Biomed Eng,* vol. 57, pp. 2910-7, Dec 2010.

[138] B. K. Pierscionek and R. A. Weale, "Presbyopia - a maverick of human aging," *Arch Gerontol Geriatr,* vol. 20, pp. 229-40, May-Jun 1995.

[139] R. C. Augusteyn, "Growth of the human eye lens," *Mol Vis,* vol. 13, pp. 252-7, 2007.

[140] S. Milas, J. Y. Ye, T. Norris, K. Hollman, S. Emelianov, and M. O'Donnell, "Acoustic characterization of microbubble dynamics in laser-induced optical breakdown," *IEEE Trans. Ultrason. Ferroelec. Freq. Control,* vol. 50, pp. 517-522, 2003.

[141] S. Milas, J. Y. Ye, T. Norris, L. Balogh, J. Baker, K. Hollman, S. Emelianov, and M. O'Donnell, "Acoustic detection of microbubble formation induced by enhanced optical breakdown of silver/dendrimer nanocomposite," *App. Phys. Lett.,* vol. 82, pp. 994-996, 2003.

[142] S. Yoon, S. Aglyamov, A. Karpiouk, and S. Emelianov, "High pulse repetition frequency ultrasound system for ex vivo measurement of mechanical properties of crystalline lenses with laser-induced microbubble interrogated by acoustic radiation force," *Phys. Med. Biol,* vol. Submitted, 2012.

[143] H. Lubatschowski, S. Schumacher, M. Fromm, A. Wegener, H. Hoffmann, U. Oberheide, and G. Gerten, "Femtosecond lentotomy: generating gliding planes inside the crystalline lens to regain accommodation ability," *j. Biophotonics,* vol. 3, pp. 265-268, 2011.

[144] K. J. Bos, D. F. Holmes, K. E. Kadler, D. McLeod, N. P. Morris, and P. N. Bishop, "Axial structure of the heterotypic collagen fibrils of vitreous humour and cartilage," *J Mol Biol,* vol. 306, pp. 1011-22, Mar 9 2001.

[145] D. A. Swann and I. J. Constable, "Vitreous structure. I. Distribution of hyaluronate and protein," *Invest Ophthalmol,* vol. 11, pp. 159-63, Mar 1972.

[146] J. L. Denlinger, G. Eisner, and E. A. Balazs, "Age-related changes in the vitreus and lens of rhesus monkeys (Macaca mulatta)," *Exp Eye Res,* vol. 31, pp. 67-79, Jul 1980.

[147] L. I. Los, "The rabbit as an animal model for post-natal vitreous matrix differentiation and degeneration," *Eye (Lond),* vol. 22, pp. 1223-32, Oct 2008.

[148] J. Sebag, "Age-related changes in human vitreous structure," *Graefes Arch Clin Exp Ophthalmol,* vol. 225, pp. 89-93, 1987.

[149] N. E. Byer, "Natural history of posterior vitreous detachment with early management as the premier line of defense against retinal detachment," *Ophthalmology,* vol. 101, pp. 1503-13; discussion 1513-4, Sep 1994.

[150] L. I. Los, R. J. van der Worp, M. J. van Luyn, and J. M. Hooymans, "Age-related liquefaction of the human vitreous body: LM and TEM evaluation of the role of proteoglycans and collagen," *Invest Ophthalmol Vis Sci,* vol. 44, pp. 2828-33, Jul 2003.

[151] J. Sebag, "Anatomy and pathology of the vitreo-retinal interface," *Eye (Lond),* vol. 6 (Pt 6), pp. 541-52, 1992.

[152] S. Schulze, S. Hoerle, S. Mennel, and P. Kroll, "Vitreomacular traction and exudative age-related macular degeneration," *Acta Ophthalmol,* vol. 86, pp. 470-81, Aug 2008.

[153] F. Mojana, L. Cheng, D. U. Bartsch, G. A. Silva, I. Kozak, N. Nigam, and W. R. Freeman, "The role of abnormal vitreomacular adhesion in age-related macular degeneration: spectral optical coherence tomography and surgical results," *Am J Ophthalmol,* vol. 146, pp. 218-227, Aug 2008.

[154] R. Machemer, "The development of pars plana vitrectomy: a personal account," *Graefes Arch Clin Exp Ophthalmol,* vol. 233, pp. 453-68, Aug 1995.

[155] V. Lakhanpal, S. S. Schocket, M. J. Elman, and M. R. Dogra, "Intraoperative massive suprachoroidal hemorrhage during pars plana vitrectomy," *Ophthalmology,* vol. 97, pp. 1114-9, Sep 1990.

[156] F. M. Recchia, A. J. Ruby, and C. A. Carvalho Recchia, "Pars plana vitrectomy with removal of the internal limiting membrane in the treatment of persistent diabetic macular edema," *Am J Ophthalmol,* vol. 139, pp. 447-54, Mar 2005.

[157] J. Kathawate and S. Acharya, "Computational modeling of intravitreal drug delivery in the vitreous chamber with different vitreous substitutes," *Int. J. Heat Mass Transfer,* vol. 51, pp. 5598-5609, 2008.

[158] D. Maurice, "Review: practical issues in intravitreal drug delivery," *J Ocul Pharmacol Ther,* vol. 17, pp. 393-401, Aug 2001.

[159] J. Aguayo, B. Glaser, A. Mildvan, H. M. Cheng, R. G. Gonzalez, and T. Brady, "Study of vitreous liquifaction by NMR spectroscopy and imaging," *Invest Ophthalmol Vis Sci,* vol. 26, pp. 692-7, May 1985.

[160] S. Milas, J. Y. Ye, T. Norris, K. Hollman, S. Emelianov, and M. O'Donnell, "Acoustic characterization of microbubble dynamics in laser-induced optical breakdown," *IEEE Trans. Ultrason. Ferroelec. Freq. Control,* vol. 50, pp. 517-522, 2003.

[161] T. T. Kleinberg, R. T. Tzekov, L. Stein, N. Ravi, and S. Kaushal, "Vitreous substitutes: a comprehensive review," *Surv Ophthalmol,* vol. 56, pp. 300-23, Jul-Aug 2011.

[162] R. C. Augusteyn, "Growth of the lens: in vitro observations," *Clin Exp Optom,* vol. 91, pp. 226-39, May 2008.

[163] R. C. Augusteyn, C. E. Jones, and J. M. Pope, "Age-related development of a refractive index plateau in the human lens: evidence for a distinct nucleus," *Clin Exp Optom,* vol. 91, pp. 296-301, May 2008.

[164] J. Keenan, D. F. Orr, and B. K. Pierscionek, "Patterns of crystallin distribution in porcine eye lenses," *Mol Vis,* vol. 14, pp. 1245-53, 2008.

[165] E. A. Balazs and L. Sunblad, "Studies on the structure of the vitreous body. V. Soluble protein content," *J Biol Chem,* vol. 235, pp. 1973-8, Jul 1960.

[166] A. Vogel, N. Linz, S. Freidank, and G. Paltauf, "Femtosecond-laser-induced nanocavitation in water: implications for optical breakdown threshold and cell surgery," *Phys Rev Lett,* vol. 100, p. 038102, Jan 25 2008.

[167] C. B. Schaffer, A. Brodeur, J. F. Garcia, and E. Mazur, "Micromachining bulk glass by use of femtosecond laser pulses with nanojoule energy," *Opt Lett,* vol. 26, pp. 93-5, Jan 15 2001.

[168] Y. R. Shen, *The principles of nonlinear optics*. New York: Wiley, 1984.

[169] W. Watanabe, T. Asano, K. Yamada, K. Itoh, and J. Nishii, "Wavelength division with three-dimensional couplers fabricated by filamentation of femtosecond laser pulses," *Opt Lett,* vol. 28, pp. 2491-3, Dec 15 2003.

[170] C. L. Arnold, A. Heisterkamp, W. Ertmer, and H. Lubatschowski, "Computational model for nonlinear plasma formation in high NA micromachining of transparent materials and biological cells," *Optics Express,* vol. 15, pp. 10303-10317, 2007.

[171] W. J. Smith, *Modern lens design*, 2nd ed. New York: McGraw-Hill, 2005.

[172] S. Y. Emelianov, M. F. Hamilton, Y. A. Ilinskii, and E. A. Zabolotskaya, "Nonlinear dynamics of a gas bubble in an incompressible elastic medium," *J Acoust Soc Am,* vol. 115, pp. 581-8, Feb 2004.

[173] E. A. Zabolotskaya, Y. A. Ilinskii, G. D. Meegan, and M. F. Hamilton, "Modifications of the equation for gas bubble dynamics in a soft elastic medium," *J Acoust Soc Am,* vol. 118, pp. 2173-81, Oct 2005.

Vita

Sangpil Yoon was born and raised in Seoul, Korea. He attended Yonsei University, Seoul, Korea and acquired his B.S. degree in Mechanical Engineering. Right after he completed his undergraduate courses, he went to Georgia Institute of Technology, Atlanta, GA. After he received his M.S. degree at Georgia Tech on 2004, Sangpil worked for Samsung Electronics, Suwon-city, Korea, as an Engineer, for three years. He started his Ph.D. work at Acoustics Program in the Department of Mechanical Engineering at the University of Texas at Austin, Austin, Texas on August 2008. He joined the Ultrasound imaging and therapeutics research laboratory on September 2008 and started working with Dr. Stanislav Emelianov. He passed his qualifying examination on August 2009 and defended on April 2012. For his doctoral studies at the University of Texas at Austin (August 2008 – May 2012), he developed an approach to measure soft tissue mechanical properties using laser and ultrasound. He wrote two first-author papers on journals and was a contributor to another article. Moreover, two first-author manuscripts are currently under review. He also presented his work at three international conferences. Sangpil was a recipient of Warren A. and Alice L. Meyer Endowed Scholarship in Engineering, The University of Texas at Austin (2011 – 2012). He will continue his work with Dr. Michael Kolios at Ryerson University, Toronto, Canada as a postdoctoral research fellow. He will concentrate on red blood cell aggregation detection using photoacoustic imaging and cell death detection by decorrelation time measurements using OCT and their clinical applications.

E-mail: s.yoon@utexas.edu

This dissertation was typed by Sangpil Yoon